McGill

EFFECT OF DEFORMATION CONDITIONS ON TEXTURE AND MICROSTRUCTURE OF MAGNESIUM SHEET AZ31

By

Emilie Chia Ching Hsu

A Thesis Submitted to the Faculty of Graduate Studies and Research in Partial Fulfillment of the Requirement for the Degree of Master of Engineering

Department of Mining, Metals and Materials Engineering
McGill University
Montreal, Canada

December 2006

Your file Votre référence
ISBN: 978-0-494-32596-4
Our file Notre référence
ISBN: 978-0-494-32596-4

Abstract

Magnesium alloys have a great potential in automotive industries, compared to steel and aluminium (Al), Magnesium (Mg) is much lighter and this weight reduction improves fuel efficiency and lowers green gas emission. Due to its hexagonal crystal structure, magnesium has poor ductility at room temperature. Magnesium's ductility improves significantly above about 200°C due to thermal activation of additional slip systems. This has lead to efforts to form auto-body panels with commercial AZ31 magnesium sheet at elevated temperatures. In this work, various AZ31 magnesium alloy materials were used to investigate the influence of deformation conditions on texture and microstructure. Moreover, it is to define the correlation between formability and different deformation mechanisms.

It was observed that only basal slip and twinning contributed to room temperature deformation. As deformation temperature increased, an increase in ductility in Mg contributed to dynamic recrystallization occurring readily at elevated temperatures (≥ 300 °C). Even coarse grain material experienced significant tensile elongation due grain refinement. Depending on temperature and strain rate, different deformation mechanisms were activated and lead to different failure modes (moderate necking, cavity, strong necking). More specifically, deformation at elevated temperature in the low-strain-rate regime with stress exponent n about 2-3 and activation energy close to grain-boundary diffusion of Mg (Q = 92 kJ/mol) is characteristic of GBS. Deformation at elevated temperature in the high strain rate regime showed that the stress exponent increased to a

value close to 5 and that the activation energy was consistent with the one for Mg self-diffusion (135 kJ/mol) and for diffusion of Al in Mg (143 kJ/mol). This was indicative of a dislocation creep deformation mechanism. Plus the six-fold symmetric patterns of the $\{1\bar{1}00\}$ and $\{11\bar{2}0\}$ pole figures and the splitting of basal plane distribution are another indication of slip mechanism or of dislocation creep mechanism.

The optimum deformation behavior for AZ31 sheet was found to be for the material with fine grain microstructure. The highest elongation of 265% was obtained with the material having initial grain size of 8 μm. In addition, strain-rate sensitivity, which is a good indication of material's ductility, also was the highest in material with 8 μm grain size. As a common trend, the strain-rate sensitivity increased with decreasing strain rate, increasing temperature and decreasing grain size.

In terms of drawability of AZ31 sheet, the deformation controlled by GBS resulted in a fair drawability/formability property with r-value about 1 whereas a deformation mechanism controlled by dislocation creep showed a good drawability with r-value above 1.5. Due to activation of additional slip systems (non-basal <a> and <c+a>), the thinning of the sheet was prevented, in particular at deformation conditions of 450°C with $0.1s^{-1}$ where r-value was highest. This deformation condition might suggest good forming process parameters, especially for deep drawing, for the commercial AZ31 sheet under investigation. A preliminary study of Forming Limit Diagram for AZ31 sheet was performed by the Limit Dome Height test method at 300°C. The FLD_0 of AZ31 was found to be 67%; the part depth of biaxial forming was 1.86 in; and the maximum LDH varied from 2.4 to 2.6 in.

Résumé

Les alliages de magnésium sont de plus en plus prisés par les constructeurs automobiles. Comparativement à l'acier et à l'aluminium, le magnésium est beaucoup plus léger, ce qui entraîne une réduction de poids des composantes automobiles et donc, améliore l'efficacité en carburant et réduit les émissions de gaz. En raison de la structure cristalline hexagonale de magnésium, il s'ensuit une ductilité minimum du magnésium à la température ambiante. Toutefois, cette ductilité s'améliore de manière significative au-dessus d'une température d'environ 200°C dû à l'activation thermique de systèmes de glissement additionnels. Ceci explique pourquoi les chercheurs et industriels favorisent actuellement la mise en œuvre de feuilles commerciales de magnésium AZ31 à hautes températures. Dans ce mémoire de maîtrise, divers échantillons d'alliage de magnésium AZ31 ont été utilisés pour étudier l'influence des états de déformation sur la texture et la microstructure. En effet, l'objectif ultime du projet visait la corrélation entre la formabilité et les différents mécanismes de déformation de l'alliage de magnésium AZ31.

Il a été observé que seuls le glissement basal et le maclage contribuaient à la déformation plastique du magnésium à température ambiante. À mesure que la température de déformation a été augmentée, une hausse de la ductilité du magnésium a été observée due au processus de recristallisation dynamique apparaissant aux températures plus élevées ($\geq$300°C). Même les échantillons présentant initialement une taille de grains importante ont démontré une amélioration significative de leur allongement à la rupture dû à un phénomène d'affinement de la taille des grains. Selon la température et la vitesse de

déformation, différents mécanismes de déformation ont été activées et ont mené à différents modes de défaillance (striction modérée, cavitation, striction forte). Plus spécifiquement, la déformation aux températures élevées dans le régime de basse vitesse de déformation, avec un exposant *n* d'environ 2-3 et la valeur d'énergie d'activation près de celle de diffusion intergranulaire du magnésium (Q = 92 kJ/mol), s'est vue caractéristique du glissement intergranulaire. Par ailleurs, une déformation à températures élevées cette fois-ci dans le régime de haute vitesse de déformation, avec un exposant *n* d'environ 5 et une valeur d'énergie d'activation située près de celle de l'autodiffusion de magnésium (135 kJ/mol) et celle de la diffusion de l'aluminium dans le magnésium (143 kJ/mol), s'est vue une indication d'un mécanisme de déformation de fluage de dislocation. De plus, les six-plis de motifs symétriques du $\{1\bar{1}00\}$ et $\{11\bar{2}0\}$ figures de pôle et la division de la distribution du plan de base sont une autre indication d'une déformation par glissement ou par fluage de dislocation.

Le meilleur comportement en déformation a été observé pour la feuille de magnésium AZ31 présentant une microstructure à grains fins. Un allongement maximal de 265% a été obtenu pour l'échantillon ayant une taille de grain initiale de 8μm. En outre, la sensibilité à la vitesse de déformation, qui est une bonne indication de la ductilité du matériau, s'est également avérée être la plus haute pour l'échantillon ayant une taille de grain de 8 μm. De plus, il a été observé que la sensibilité à la vitesse de déformation augmentait avec une croissance de la température et une décroissance de la vitesse de déformation et de la taille de grain.

Pour une déformation contrôlée par le glissement intergranulaire et pour un coefficient

d'anisotropie plastique (r) d'environ 1, il a été observé que la formabilité et les aptitudes à l'emboutissage de la feuille de magnésium AZ31 étaient acceptables. Toutefois, ces deux aptitudes se sont vus améliorées pour un r supérieur à 1.5 et lorsque le fluage de dislocation agissait comme mécanisme de déformation principal. Cette observation peut s'expliquer par une atténuation de l'amincissement de la feuille dû à l'activation de systèmes de glissement additionnels (<a> non-basal et <c+a>). Ceci a été particulièrement vrai pour une déformation réalisée à une température de 450°C et pour une vitesse de $0.1s^{-1}$, où le coefficient r a atteint sa valeur la plus haute. Cet état de déformation pourrait suggérer de bons paramètres de formabilité pour la feuille commerciale de magnésium AZ31, particulièrement en ce qui a trait au procédé d'emboutissage profond. Finalement, une étude préliminaire sur les courbes limites de formage pour la feuille de magnésium AZ31 a été réalisée pour un procédé d'expansion (« Limit Dome Height ») effectué à une température de 300°C. Le FLD_0 de magnésium AZ31 s'est alors avéré de 67%, la hauteur de la pièce à la force maximale était de 1.86 po et le maximum LDH (hauteur de la pièce à la rupture) variait de 2.4 à 2.6 po.

Acknowledgements

I would like to express my sincere gratitude to my supervisor, professor Jerzy Z. Szpunar, for his guidance, support, patience and encouragement. I am also very grateful to professor Steve Yue, who was the chief of the Mg project, for his input, constructive criticisms and discussions. Both professors have provided me with invaluable opportunities to investigate in physical metallurgy and participate in scientific conferences that have enhanced and strengthened my knowledge of materials science.

I am appreciative to Dr. Ravi Verma and Dr. John E. Carsley for their supervision and their scientific approach towards many of the problems encountered during my internship at Technical Center of General Motors in Warren, US. I am grateful to Paul E. Krajewski, Carl D. Fuerst and Jon T. Carter for their supports and encouragements. I am also thankful to the staffs at General Motors for their assistances and for making my stay at GM more enjoyable.

I would like to extend my appreciation to my fellow graduate students for their persistent and candid friendships. I am grateful to Dr. Hualong Li for his kind help concerning texture analysis. I am thankful to Slavek Poplawski for his technical assistance in resolving experimental difficulties. I am appreciative to Dr. Elhachmi Essadiqi and CANMET for supplying investigated materials. I am grateful to my officemates, Marwan Azzi, Jae-Young Cho and Tedric Soh, and as well as the people from the Texture lab for providing friendly working environment. In addition, I would like to thank the graduate students who also participate in this Mg project, in particular Dr. Faramarz Zarandi, Lihong Shang and Dr. Rocco Varano.

I am deeply thankful to my parents for their unceasing love, support, and patience that have brought me to this point.

Last, but not least, the financial support from General Motors and National Science & Engineering Research Council of Canada is gratefully acknowledged.

Table of Contents

List of Figures

List of Tables

Chapter 1

Introduction

The driving force behind the development of magnesium alloys was the potential for lightweight applications. Saving weight in automobile applications in order to meet the demands for more economic use of fuel and lower emissions, magnesium usage in such field has steadily increased.

Magnesium, as the lightest available construction metal, offers a wide range of opportunities for use in automobiles. Nowadays, the main applications of magnesium are as cast parts and they can be very complex but in many cases they lack the desired properties [1, 4]. Sheet-formed magnesium parts are an alternative. Moreover they meet application demands due to fine-grained microstructure with no pores and the properties for applications are much better. The potential for the application of shaped magnesium parts in a vehicle is great; the majority of the body shape consists entirely of formed parts, representing almost 26% of the vehicle weight (Figure 1-1).

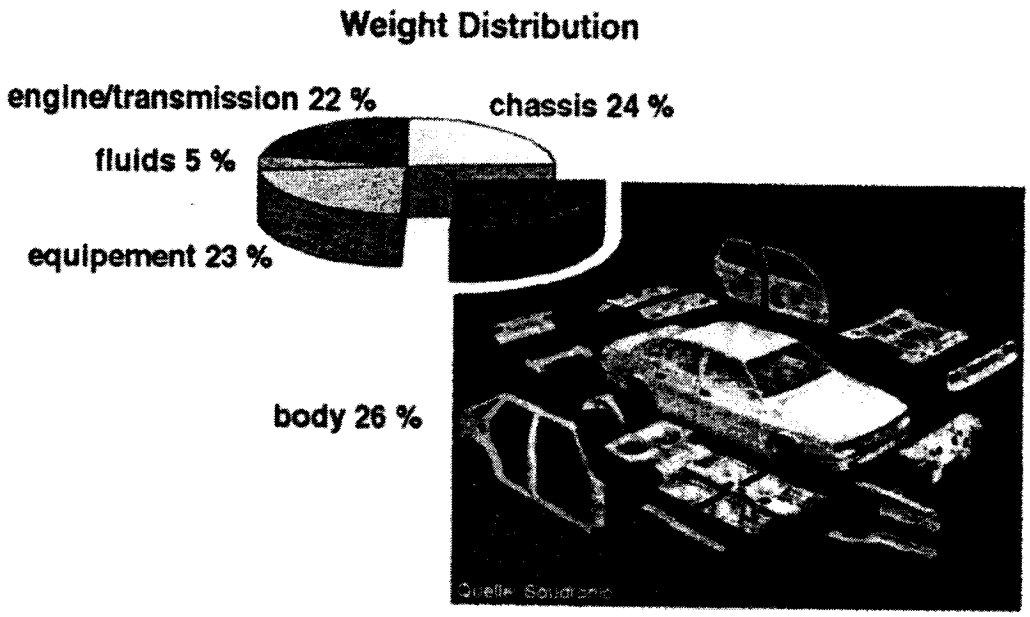

Figure 1 - 1. Use of sheets in automotive engineering [1].

The absence of sheet magnesium from mainstream production programs is related predominantly to its limited ductility at the room temperature. This is a consequence of its hexagonal close packed crystal structure that permits only a limited number of slip systems to be activated. It is known that magnesium ductility improves significantly above 200°C due to thermal activation of additional slip systems [5-8]. This has lead to efforts to form auto-body panels with commercial AZ31 magnesium sheet at elevated temperatures [9-11]. The application of the magnesium alloys in sheet forming at elevated temperatures has been discussed in several papers [9, 11-14]. Nevertheless, systematic analysis of the deformation conditions on the formability of magnesium alloys is still necessary. The research objectives of the present project are the following:

1 To understand the deformation mechanism and failure mechanisms of magnesium at different temperatures

2 To determine the effect of deformation conditions on texture and microstructure of Mg sheet

3 To improve deformation behavior of AZ31 sheet through microstructure control

4 To characterize formability of Mg sheet having different texture and microstructure

This thesis is divided into eight chapters: introduction of magnesium and its alloys characteristics, plus discussion on magnesium properties and texture measurement techniques are given in chapter 2; research materials and equipments for mechanical testing, texture measurement and metallographic examination are presented in chapter 3; investigation of deformation modes on cast AZ31 by compression is presented chapter 4; study of deformation and failure mechanisms of AZ31 sheet at elevated temperatures is given in chapter 5; optimization of AZ31 sheet's deformation behavior through microstructure control is given in chapter 6; characterization of AZ31 sheet's formability by r-value at various deformation conditions and by limit dome height (LDH) test is presented in chapter 7; and general conclusions of this research are given in chapter 8.

Chapter 2
Literature Review

2.1 Magnesium and Magnesium Alloys

2.1.1 Magnesium's Characteristics

Magnesium is the lightest of all engineering metals, having a density of only 1.74g/cm^3. It is 35% lighter than aluminum and over four times lighter than iron and steel. Its melting point is 650°C and it crystallizes into a close-packed hexagonal crystal structure. The atom positions of the magnesium unit cell are shown in Figure 2-1 along with its principal planes and direction. The lattice parameters of pure magnesium at 25°C are assessed by many investigators and are a = 0.32092 nm and c = 0.52105 nm. According the above data, the c/a value at room temperature is 1.6236, very close to the ideal value of 1.633.

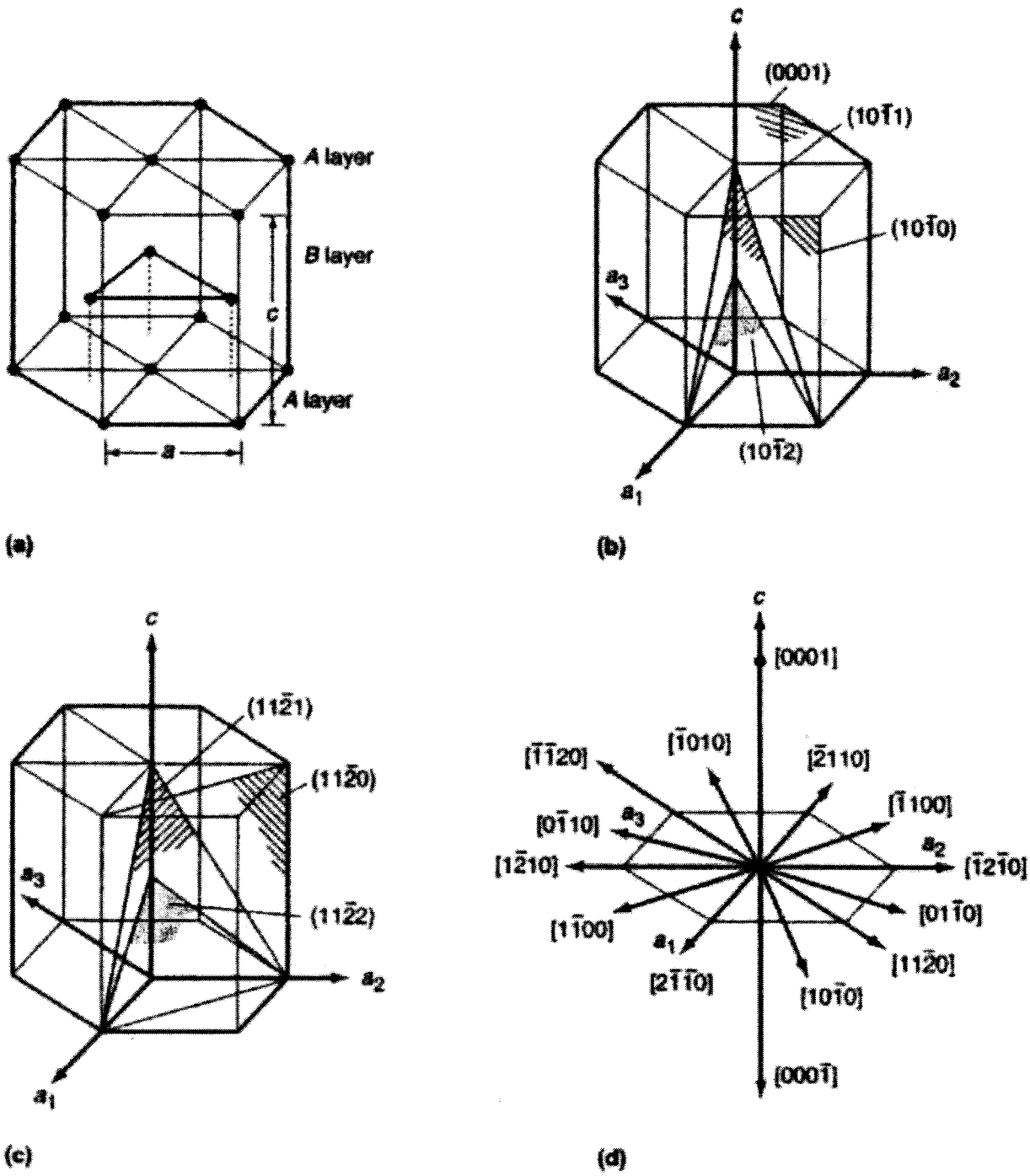

Figure 2 - 1. The magnesium unit cell crystal. (a) Atomic positions; (b) Basal plane, a face plane, and principal planes of the [1 $\bar{2}$ 10] zone; (c) Principal planes of the [1 $\bar{1}$00] zone; (d) Principal directions [3].

Below 225°C, only $\{0001\}\langle 1\bar{2}10\rangle$ basal plane slip system is possible, along with pyramidal $\{10\bar{1}2\}\langle 10\bar{1}1\rangle$ twinning system. Above 225°C, critical resolved shear stresses for prismatic and pyramidal slip systems are lowered and magnesium suddenly shows good deformation behavior, suggesting that the extensive deformation can occur above this temperature. More discussion on magnesium's slip systems will be presented in following sections.

2.1.2 Alloying Systems

To give a short overview of the different magnesium alloys, it is necessary to first show the identification of all kinds of alloys and the effect of each allying element.

Magnesium Alloys

The classification identification of magnesium alloys is standardized worldwide by the ASTM norm; each alloy is marked with letters indicating the main alloy elements, followed by the rounded figures of each (usually two) weight in percentage terms. Table 2-1 shows the key letter for every alloying element. The alloy AZ31, for example, is an alloy with a rated content of 3% aluminum (A) and 1% zinc (Z).

Table 2 - 1. Code letter for the designation system of magnesium alloys [3].

Letter Code	Alloying Element
A	Aluminum
C	Copper
E	Rare-Earth metals
H	Thorium
K	Zirconium
L	Lithium
M	Manganese
Q	Silver
S	Silicon
T	Tin
W	Yttrium
Z	Zinc

Alloying Elements

Magnesium, which is readily obtainable commercially at purity better than 99.8%, is rarely used for engineering application in the unalloyed form due to its low ultimate strength. To increase its strength-to-weight ratio, magnesium is alloyed with one or more elements. The groups of alloy system that are currently being commercially produced are based on several major alloying elements: aluminum, zinc, manganese, zirconium and rare-earth metal [3]. Addition of lithium has been an interest for wrought Mg for improving formability. Table 2-2 describes the effects of the alloying elements on properties.

Table 2 - 2. Effects of alloying elements [3].

Alloying	Effects
Aluminum	It has the most favorable effect on magnesium of any of the alloying elements. It improves strength and hardness, and it widens the freezing range and makes the alloy easier to cast. When present in amounts in excess of 6wt%, the alloy becomes heat treatable, but commercial alloys rarely exceed 10wt% aluminum.
Zinc	It is next to aluminum in effectiveness as an alloying ingredient in magnesium. Zinc is often used in combination with aluminum to produce improvement in room temperature strength. Zinc also helps to overcome the harmful corrosive effect of iron and nickel impurities that might be present in the magnesium alloy.
Manganese	It does not have much effect on tensile strength, but it does increase yield strength slightly. Its most important function is to improve the saltwater resistance of Mg-Al and Mg-Al-Zn alloys by removing iron and other heavy metal elements into relatively harmless intermetallic compounds, some of which separated out during melting. The amount of manganese that can be added is limited by its relatively low solubility in magnesium.
Zirconium	It has a powerful grain refining effect on magnesium alloys due to its lattice parameters of α-zirconium are very close too those of magnesium. The zirconium-rich solid particles produced early in the freezing of the melt may provide sites for the heterogeneous nucleation of magnesium grains during solidification.
Rare-Earth	Additions of rare-earths increase the strength of magnesium alloys at elevated temperatures. They form eutectic systems of limited solubility with magnesium. Thus precipitation hardening is possible at grain boundaries and grain interiors that limit grain boundary sliding and pin dislocation.
Lithium	It has relatively high solid solubility in magnesium, and because of its low relative density of 0.54, it has attracted interest as an alloying element in magnesium alloys to lower the density to values even lower that that of unalloyed magnesium. Moreover, only some 11 wt% of lithium is needed to form the β phase, which has a body-centered cubic (bcc) crystal structure, thereby improving formability of wrought products.

Wrought Alloys

Since the focus of this present work is on the application of magnesium sheet in automobiles, the Mg/Al series of alloys, such as AZ31 and AZ61, play the most important role among the most common commercial wrought Mg alloys. Tables 2-3 and 2-4 give an overview of the composition and properties of selected wrought alloys.

Table 2 - 3. Chemical composition of selected magnesium wrought alloys [4].

Alloy	Al	Zn	Mn	Cu	Ca	Zr
AZ31	3.0	1.0	0.3			
AZ31B	2.5-3.5	0.7-1.3	0.2-1.0	0.05	0.04 max	
AZ61A	5.8-7.2	0.4-1.5	0.15-0.5	0.05		
AZ80	8.5	0.5	0.12			
ZK40		3.5-4.5				0.45 min
ZK60A		4.8-6.2				0.45 min

Table 2 - 4. Mechanical properties of various magnesium wrought alloys [4].

Condition	Alloy	Tensile Strength [MPa]	0.2% Yield Strength [MPa]	Fracture Elongation [%]
	AZ31B-F	262	193	14
	AZ61A-F	317	228	17
	AZ80-T5	379	276	7
	ZK60A-T5	365	303	11
	AZ31B-F	248	165	16
	AZ61A-F	283	165	14
	ZK60A-T5	345	276	11
	AZ31B-H24	290	221	15
	AZ31B-O	255	152	21

2.1.3 Crystallographic slip systems and Twinning of Magnesium

Figure 2-2 shows a more systematic figure representation of the direction for easy crystallographic slip in magnesium single crystal. There are the three $[11\bar{2}0]$ or [a] close packed directions. The three dominant sets of planes that contain this slip direction are: (1) the {0001} basal plane, (2) the three $\{1\bar{1}00\}$ planes and (3) the six $\{1\bar{1}01\}$ planes. All of the easy $<11\bar{2}0>$ slip directions are perpendicular to the c-axis, as shown in Figure 2-2. The slip on the system listed above does not produce any elongation or shortening parallel to the c-axis. In order to accommodate the deformation in this direction, slip or twin system with <c+a> directions must be operative. At room or low temperature, twinning $\{10\bar{1}2\}<10\bar{1}1>$ is the dominant deformation accommodating mechanism that allows for the shape changes in c-axis.

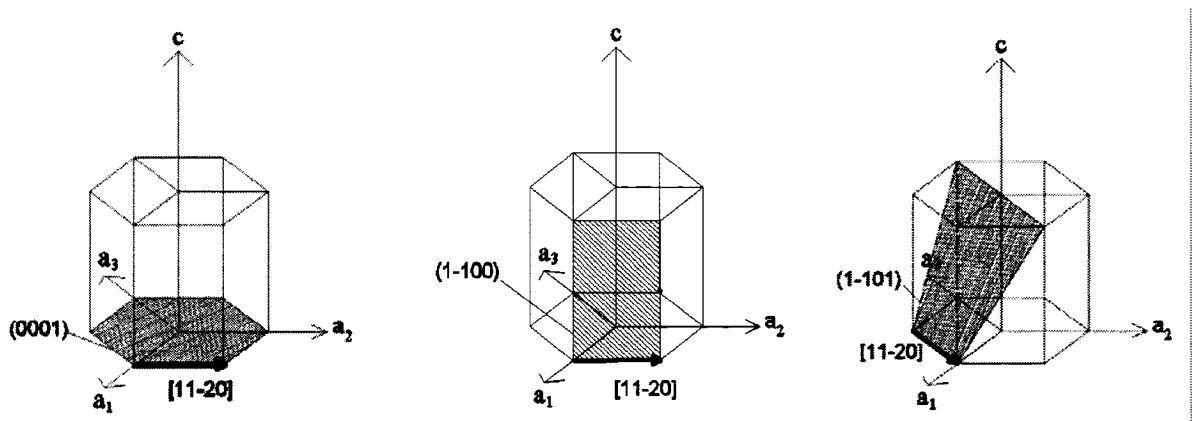

Figure 2 - 2. Slip systems of Mg. (a) basal slip $(0001)<11\bar{2}0>$; (b) $(1\bar{1}00)<11\bar{2}0>$ slip; (c) $(1\bar{1}01)<11\bar{2}0>$ slip.

Twinning

Twinning plays an important role in plastic deformation. Not only the strain is produced be the twinning process but also the orientation changes resulting from twinning may

place new slip systems in a favorable orientation with respect to the stress axis so that additional slip can take place. However, it should be understood that only a relatively small fraction of the total volume of a crystal is reoriented by twinning, and therefore magnesium and its alloys will, in general, possess less ductility than metals with a greater number of slip systems.

At room temperature, twinning readily occurs on the $\{10\bar{1}2\}<10\bar{1}1>$ system. However, twinning can be characterized into $\{10\bar{1}2\}$ tensile twins and $\{10\bar{1}1\}$ compression twins [5]. Figure 2-3 shows the two types of twins (compression and tensile) slips systems in a magnesium HCP crystal structure.

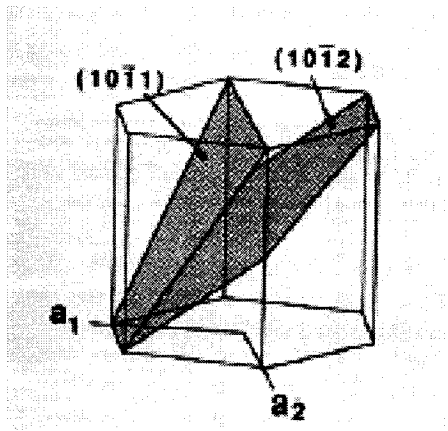

Figure 2 - 3. Compression and tensile twin in HCP crystal. [15].

Double twinning, involving $\{10\bar{1}1\}$ followed by $\{10\bar{1}2\}$ twinning, has also been reported in a cold rolled Mg alloys [15]. Double twinning is able to facilitate compression along the c-axis of the unit cell. However, it should be noted that <c+a> slip, which can accommodate compression along the c-axis has observed by some authors. Figure 2-4 is a schematic image describing the different types of twins found in deformed HCP metals,

like Mg.

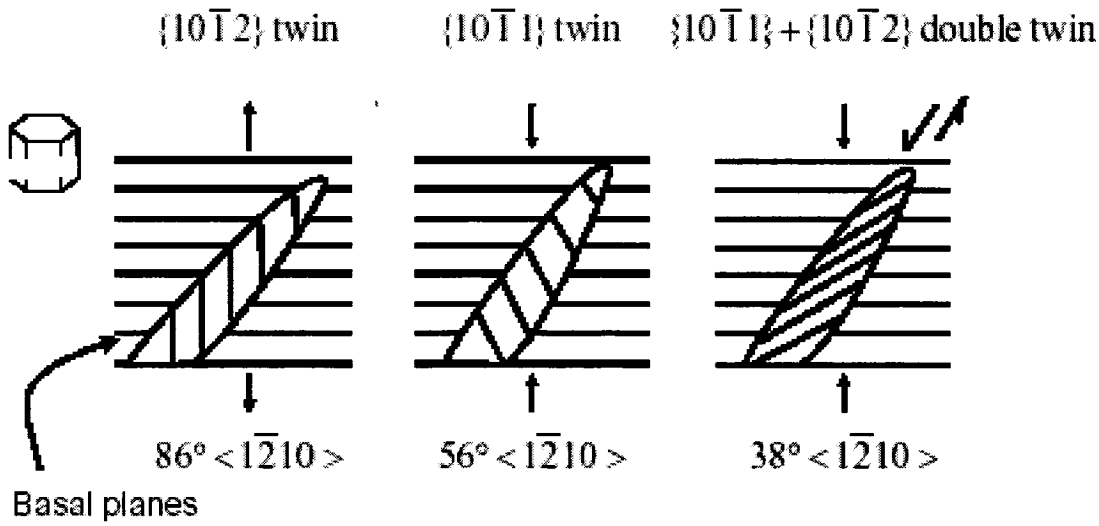

Figure 2 - 4. Types of twins occurring in deformation [16].

In Figure 2-5, a Mg-0.2Ce alloy cold rolled to 10% thickness reduction is presented to illustrate the different types of twin occurring during deformation. The boundaries corresponding to {10$\bar{1}$2} twins (i.e. 86° <11$\bar{2}$0>), {10$\bar{1}$1} twins (i.e. 56° <11$\bar{2}$0>) and {10$\bar{1}$1}+{10$\bar{1}$2} double twins (i.e. 38° <11$\bar{2}$0>) are assume to have a common plane of shear. The two twins in the lower middle of the images (marked B and C) contain within them fragments of all three types of twin boundaries.

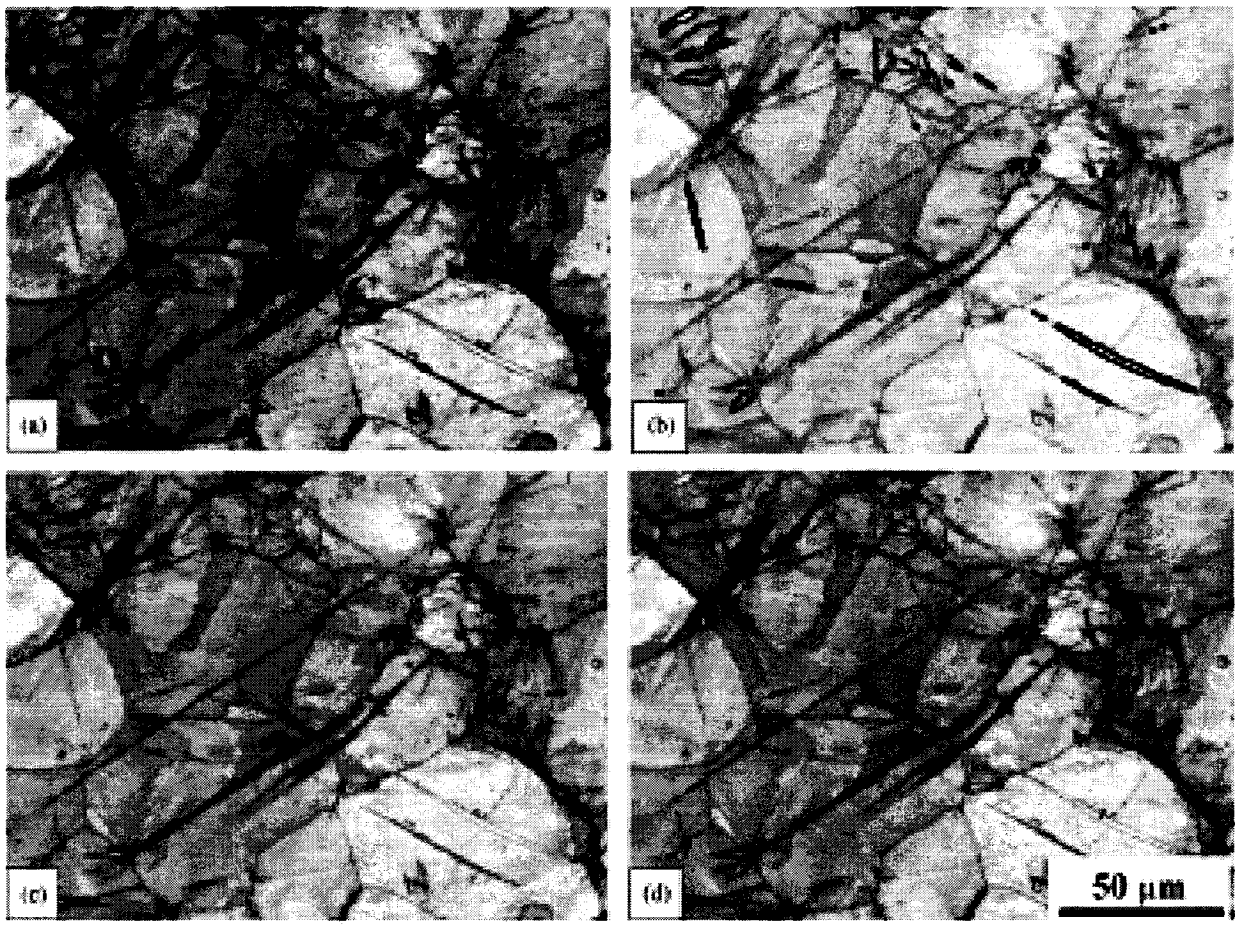

Figure 2 - 5. An example of double twinning in which $\{10\bar{1}2\}$ twins form within $(10\bar{1}1)$, for Mg-0.2Ce sample cold rolled to 10% reduction. (a) Kikuchi band contrast; (b) $\{10\bar{1}2\}$ twin boundaries (86° $<11\bar{2}0>$ ±5°); (c) $\{10\bar{1}1\}$ twin boundaries (56° $<11\bar{2}0>$ ±5°); (d) boundaries expected from $\{10\bar{1}1\}$+$\{10\bar{1}2\}$ double twinning (38° $<11\bar{2}0>$ ±5°); (e) interpretation of twins B and C. RD-ND sections with RD parallel to scale bar [17].

2.1.4 Textures of Magnesium

In material science, texture is a distribution of crystallographic orientations of a material. When theses orientations are fully random, the material is said to have no texture. If the crystallographic orientations have some preferred orientation, then the material has a weak, strong, or moderate texture. The degree of the texture is dependent on the percentage of crystals that have the preferred orientation. Most engineering materials have preferred orientations which results from different thermomechanical processing. Actually, the crucial aspects for texture development depend on the crystal structure as well as the nature and severity of the thermomechanical processes. One of the common thermomechanical processes is rolling, which is a process of working and shaping metal by passing it between rolls. For instance, a rolled metal tends to have a strong texture, while a solidified metal from a melt has a weak texture.

The importance and significance of texture to materials lies in the fact that many material properties are texture-specific. A texture material leads to anisotropy of physical and chemical properties, such as plasticity, ductility, strength and corrosion resistance. In the case of a rolled magnesium alloy, it has a strong texture and anisotropic property that affect its strength and ductility. As a consequence, the mechanical properties of this alloy vary significantly with direction.

Development of Texture

Textures created during deformation depend on the crystal structure as well as the nature and severity of the working process. In the case of magnesium alloys, having hexagonal close-packed (HCP) structure, its c/a ratio is one the factor influences the texture. HCP

rolling textures, it is categorized into three groups that are determined primarily by the c/a ratio, as shown in Figure 2-6. Metals that have c/a ratios near to the ideal close packing of sphere (1.633) have rolling textures of the type (0001) basal fiber texture. Magnesium and its alloys (c/a ~1.624) behave in this way as shown by the basal plane pole figure in Figure 2-7a. The origin of such texture may be understood in term of slip on basal plane. The slightly "egg-shaped" distribution of the (0001) basal plane has a significant influence on the anisotropy of the rolled Mg sheet, which will be discussed later. Figure 2-7b illustrates the Mg HCP crystallites arrangement in a rolled sheet.

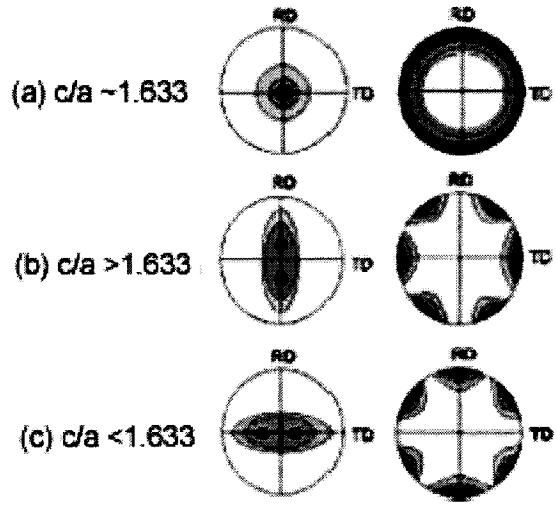

Figure 2 - 6. Simulated rolling texture in HCP metals with c/a ratio:
(a) ~1.633; (b) >1.633; (c) <1.633 [18].

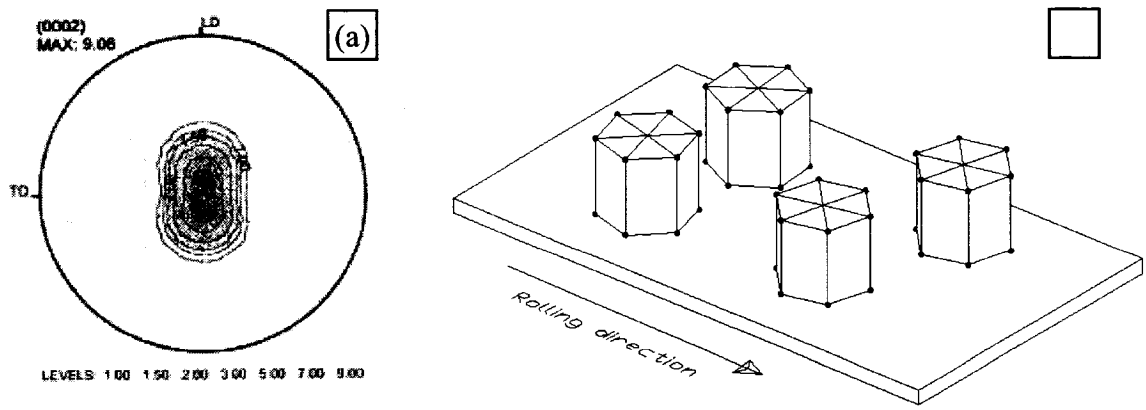

Figure 2 - 7. (a) Pole figure (0002) plane of rolled AZ31 at 250°C [19]; (b) HCP crystallites arrangement in a Mg rolled sheet.

2.1.5 Deformation Behavior of Magnesium

Flow Behavior at Various Temperatures

The principal difference between forming magnesium alloys and forming other metals is the temperature used. Temperature is a critical factor for the deformation of magnesium since magnesium shows only limited formability at ambient temperatures because of limited number of slip systems. As mentioned previously, above 225°C, additional slip systems, such as prismatic <a> slip and pyramidal $\{11\bar{2}2\}\langle 11\bar{2}\bar{3}\rangle$ (aka <c+a>) slip, become thermally activated and magnesium becomes highly deformable. This can be illustrated by the critical resolved shear stress (CRSS) of Mg single crystal at various temperatures shown in Figure 2-8.

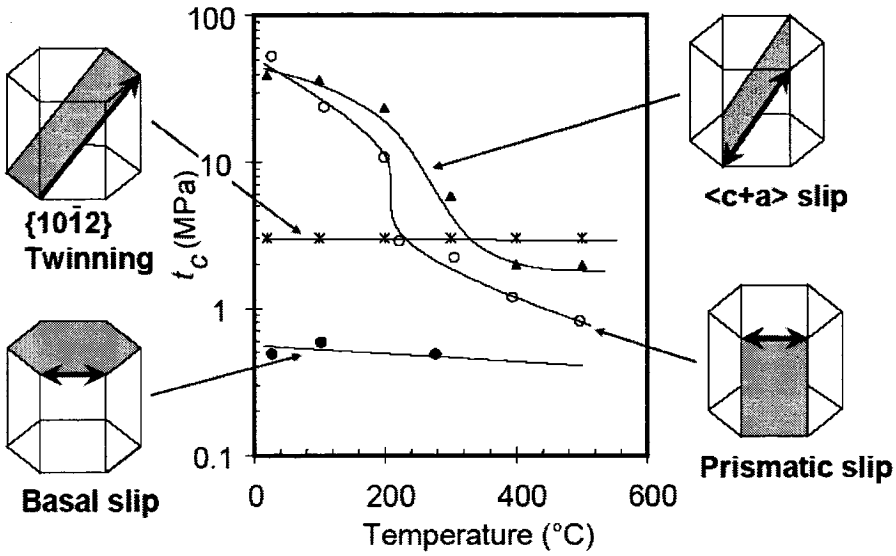

Figure 2 - 8. Critical Resolved Shear Stress (CRSS) of Mg single crystal at various temperatures [15].

Agnew [20] investigated the tensile flow curves for the alloy in RD and TD directions. (Figure 2-9). The test was performed at various temperatures ranging from room temperature to 250°C with a constant strain rate of $5\text{x}10^{-3}$ s^{-1}. As expected, the flow stress

decreased and ductility increased with increasing temperature. In addition, it was reported that there was a high dependence of the strength on the orientation of the sheet, namely RD and TD [20]. This will be discussed in later section.

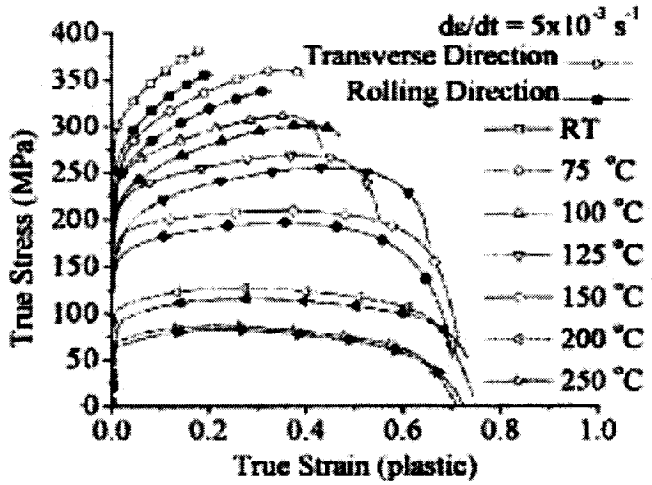

Figure 2 - 9. Flow curves of AZ31 at initial strain rate of $5x10^{-3}$ s^{-1} as a function of tensile test direction (i.e. RD & TD) and temperature [20].

Flow Behavior vs Texture

Evolution of hot-working flow stress with strain was studied under the channel die compression condition in AZ31 magnesium alloy, including the condition of "c-axis compression", "c-axis extension", as well as "c-axis constraint" in Barnett's work [21]. Three differently oriented channel die samples are illustrated in Figure 2-10.

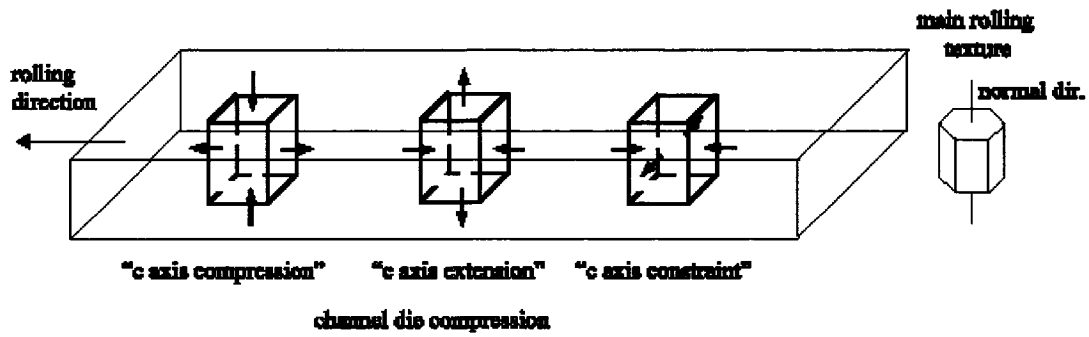

Figure 2 - 10. Orientation test samples of AZ31 with respect to the deformation and crystallographic reference frames [21].

The influence of texture on the flow stress is presented in Figure 2-11, which shows the compression flow curves obtained at the temperature of 300°C and the strain rate of $0.3s^{-1}$. The main differences of flow stress are observed at low strain and are related to different geometry of deformation of anisotropic textured specimens.

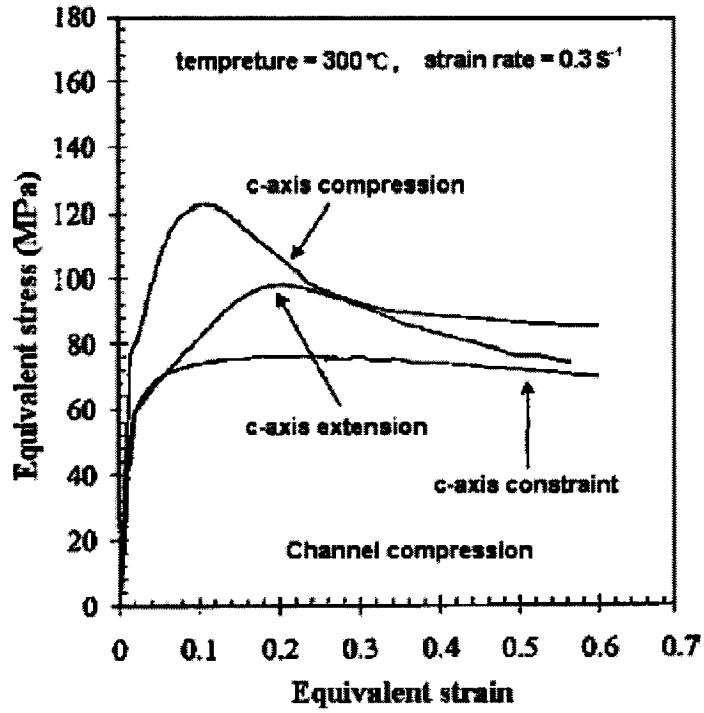

Figure 2 - 11. Flow stress–strain curves of the AZ31 Mg alloy with different crystallographic orientation tested at 300°C and 0.3 s^{-1} [21].

During deformation, slip in magnesium occurs predominantly on basal planes; however the prismatic and pyramidal slip systems become more important as the temperature raises. Twinning also readily occurs on the $\{10\bar{1}2\}<10\bar{1}1>$ system. When deformation takes place under the condition of c-axis constraint, the prismatic <a> slip systems will be favorable and this results in the low flow stress and low strain hardening rate. When deformation occurs by compression along c-axis, the prismatic <a> slip systems will become difficult and the pyramidal $\{11\bar{2}2\}<11\bar{2}\bar{3}>$ and will be activated. This will

result in high flow stress and high strain hardening. While the tensile deformation along c-axis, favors the prismatic <a> slip systems, the pyramidal $\{11\bar{2}2\}<11\bar{2}\bar{3}>$ slip and also twinning on the $\{10\bar{1}2\}<10\bar{1}1>$ system will bring the c-axis into close alignment with the plate normal [21].

Thermomechanical Processing Structure Map

A Thermomechanical Processing (TMP) structure map is proposed to plot critical conditions required for a given grain/ subgrain size following recovery, dynamic recrystallization (DRX), static recrystallization and meta-dynamic recrystallization. The key independent processing variables in TMP are strain, strain rate, temperature and in some cases, time. If the time is neglected and the temperature and strain rate are combined into one term, the Zener-Hollomon parameter is defined as :

$$Z = \dot{\varepsilon} \exp \frac{Q_{def}}{RT}$$

Equation 2-1

where $\dot{\varepsilon}$ is the strain rate, Q_{def} is the activation energy, R is the gas constant and T is temperature in Kelvin. The Zener-Holloman parameter is closely related to the flow stress. Hence it is possible to develop constitutive equations that describe flow behavior in terms of strain, strain rate, and temperature. Accordingly, conventional hot working processes parameters can be predicted which is essential for design and control. Figure 2-12 illustrates TMP structure map and defines the operating conditions of the Mg common wrought process including transition in deformation mechanism [22].

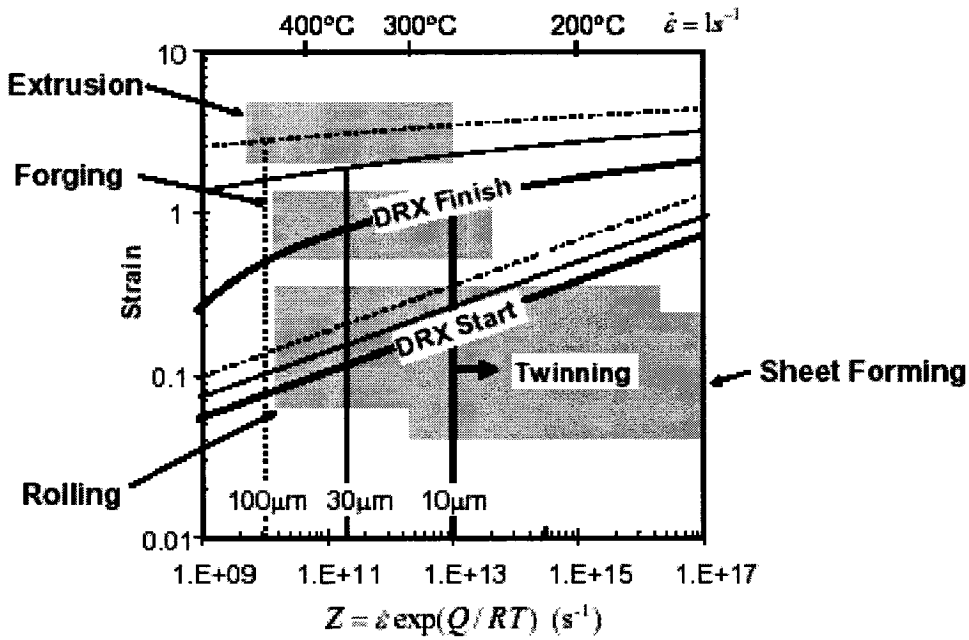

Figure 2 - 12. TMP structure map showing the conditions under which twinning and dynamic recrystallization can be expected. It is shown the approximate conditions encountered in the main wrought deformation processes [22].

2.1.6 Formability of Magnesium

Sheet metal forming processes are among the most important metal-working operations. These processes account for a sizable proportion of the manufactured goods made in industrialized countries. In order to reduce the weight of vehicles, limit fuel consumption and to address the environmental concerns, light weight materials, such as Mg alloys, are being used more and more often. Magnesium alloys have however limited formability, and therefore a thorough understanding of the deformation processes and the factors limiting the forming processes is important.

Forming Limit Diagram of AZ31 Sheet

Forming Limit Diagram (FLD) is served as a help for most stamping operations. FLD is a

map in principal strain space (e1, e2) which separated safe strain states that a material could sustain from the more severe states which would lead to failure. By definition, e1 is the major principal strain, and e2 is the minor principal strain. In other words, FLDs show a combination of major and minor in-plane principal strains beyond which failure occurs. The FLDs cover strain states from uniaxial tension through plane strain to balanced biaxial tension. Figure 2-13 shows a typical forming limit diagram of a sheet as a plot of major and minor strain. For generating a FLD, different types of tests have to be considered: stretch forming, plane strain, uniaxial tensile strain and deep drawing.

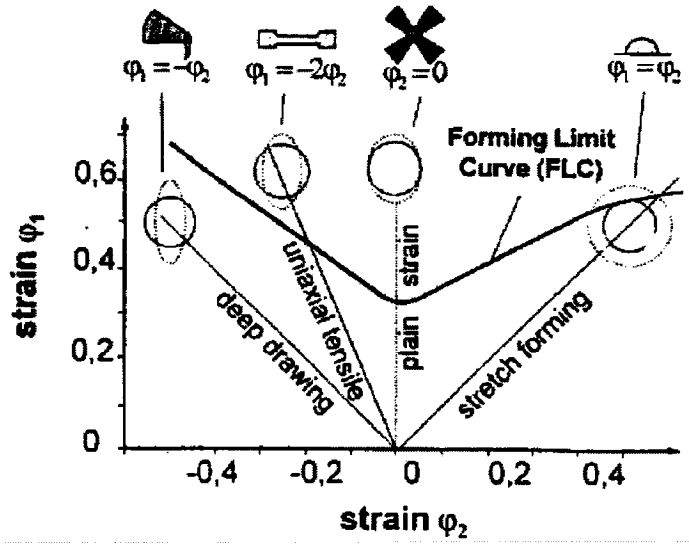

Figure 2 - 13. Forming Limit Diagram of a Sheet [23]

This FLC diagram can be determined by a single test, named Limiting dome Height test. The Limiting Dome Height (LDH) test is a modified hemispherical dome test. Instead of a fully clamped blank, strips of varying widths are clamped on the ends by a lock bead and then deformed with a hemispherical punch (most commonly four inches in diameter). Changing the width of the sample allows the strain state to be matched to the strain state of the stamping under investigation. Figure 2-14 shows how a strip fails during LDH test.

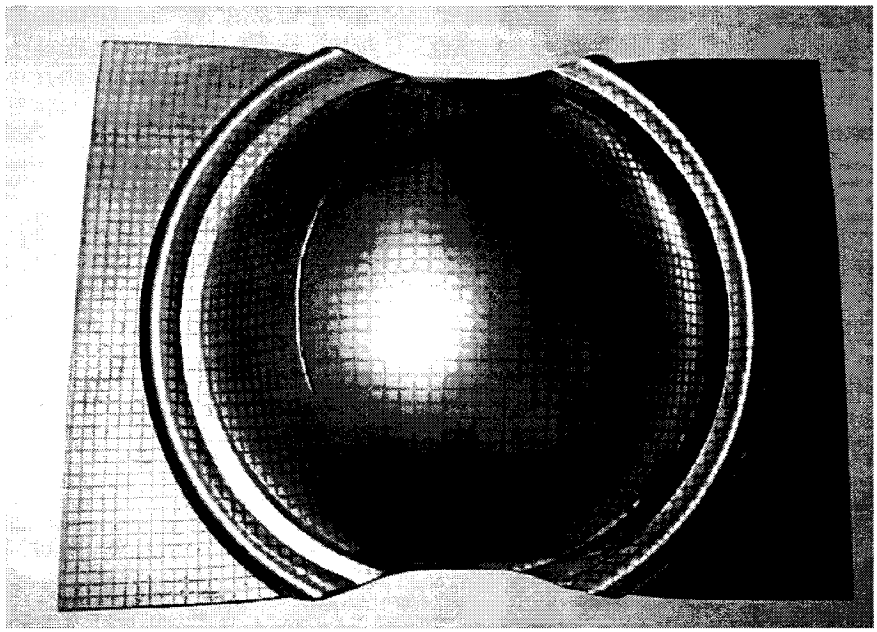

Figure 2 - 14. A LDH strip after fracture [24]

A forming limit diagram has been found from literature [25] for Mg AZ31 alloy at different temperatures and it is shown in Figure 2-15. This is to show the effect of temperature on the formability of the AZ31 alloy sheet. The limiting strains is much lower at 100 °C as compared to 300 °C, which means that the formability is better at high temperature.

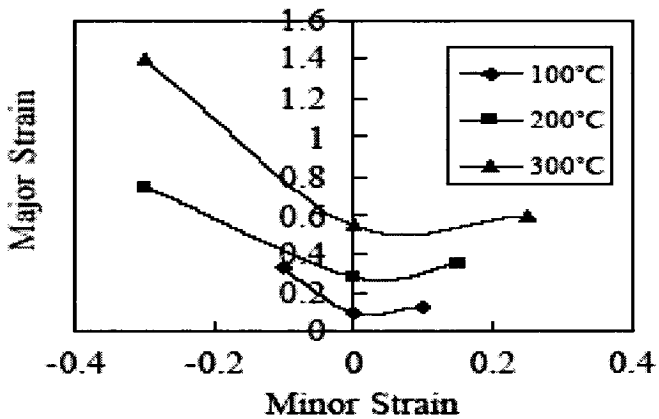

Figure 2 - 15. FLD for AZ31 alloy [25]

Anisotropic Property and r-value of Magnesium Sheet AZ31

Formability of magnesium can be determined taking into consideration the effect of directionality that exists in the worked sheet induced by the rolling process. One consequence of directionality is a change in mechanical properties with direction. For example, the yield strength and ductility may change with the orientation at which a laboratory tensile specimen is cut from a sheet. Generally, minimum and maximum values of these quantities occur at 0°, in the vicinity of 45° and at 90° with respect to the rolling direction (Figure 2-16).

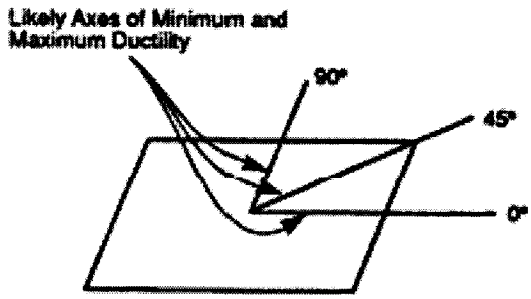

Figure 2 - 16. Directionality in properties of a rolled sheet [34].

A number of specialized laboratory mechanical tests have been developed to identify the anisotropy of directionality. Examples are measurements of plastic strain ratios in tensile tests, limiting drawing ratio measurements, cupping tests, etc. Of particular interest here is the plastic strain ratio or r-value. The r-value, which is measured using a standard tensile specimen strained to approximately 20% elongation, is defined as the ratio of the (true) strains in the width and thickness directions [26]. For AZ31, it is determined for uniform elongation of about 10% [20]. It is defined as:

$$r = \frac{e_w}{e_t} = \frac{-e_w}{(e_l + e_w)}$$

Equation 2-2

where e_w is the strain ratio in the width direction and e_t is the strain in the thickness direction and e_l is the strain ratio in the length direction specimen of a tensile loaded in the plastic regime. Conventionally, measurements are taken from the strained width and length because of the large uncertainties in determination of the thickness strains.

An average r-value, r_m, is defined as [27]:

$$r_m = \frac{(r_{0^\circ} + 2r_{45^\circ} + r_{90^\circ})}{4}$$

Equation 2-3

High values of r_m correlate with good drawability, as shown most convincingly in Figure 2-17. For a metal without any preferred orientation the individual and average r-values are all unity and the metal is isotropic. Rolled AZ31 has a strong anisotropy of r-value.. The average r-value, r_m, is a convenient measure of normal anisotropy, but the variation of r with angle with respect to the rolling direction of the sheet gives information about the extent of planar anisotropy.

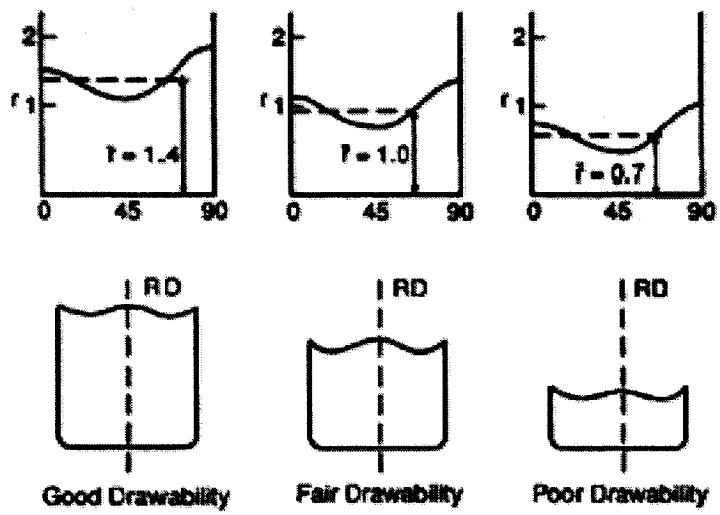

Figure 2 - 17. Relationship of plastic strain ratio to drawability [34].

This anisotropy term is often defined as [26]:

$$\Delta r = \frac{\left(r_{0^\circ} - 2r_{45^\circ} + r_{90^\circ}\right)}{2}$$

Equation 2-4

and correlate closely with the amount of earing that occurs in deep drawing. Ears tend to form along those directions in the sheet which are orthogonal to the directions of highest r-value. Thus, a positive values of Δr implies 0° and 90° earing while a negative Δr is associated with 45° earing.

In general, *r* will vary with the angle at which the tensile specimen is cut with respect to the rolling direction of the sheet. Figure 2-18 shows the r-value as a function of temperature and sample orientation at Rolling Direction (RD) and Traverse Direction (TD). The r-value of TD samples is very high (r~3) at low temperatures, while RD samples strain in a nearly isotropic fashion (r~1) [19]. The "egg-shaped" basal texture, as seen previously in Figure 2-7a, causes this strong anisotropy of the sheet. It is possible to understand that there is a better chance for activation of slip systems according to Schmid factor in the RD than in the TD [20]. However, as the temperature increases, the r-value for the TD sample drops and they become closer to those of the RD (Figure 2-18).

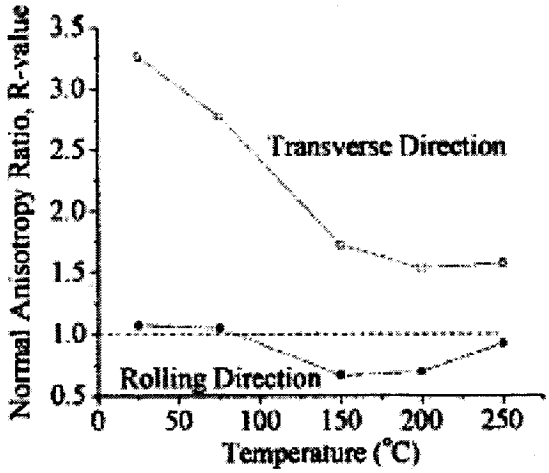

Figure 2 - 18. Plot of normal anisotropy as a function of orientation and temperature of AZ31 [20].

2.2 Texture Measurement Techniques

Texture measurement techniques will be explained in details in this section. For macrotexture techniques, the primary output is intensity diffracted from a large volume of a sample. For microtexture techniques, the primary output is a diffraction pattern from a small sampled volume. Such a pattern embodies the complete crystallographic information on the orientation of the respective sampled volume.

2.2.1 Texture Measurement by X-Ray Diffraction

Macrotexture are commonly measured by angular dispersive X-ray diffractometry. The principle of pole figure analysis by means of diffraction techniques is based on Bragg's law (Equation 2-5). As each set of lattice planes has a different lattice spacing d, the reflections from various sets of lattice planes can be distinguished by setting the detector to the corresponding angle 2θ with respect to the direction of the incident radiation.

$$\lambda = 2d\sin\theta$$

Equation 2-5

where λ is similar to the periodic atomic (lattice) spacing d inside a crystal. The scattered waves interfere to produce diffracted wave at the Bragg angle θ. To derive the crystallographic orientation of a given crystallite, the arrangement of planes with respect to an external specimen reference frame has to be determined. For the sake of simplicity, we first consider reflection at a single crystallite as schematically shown in Figure 2-19. However the same principle applied to sample with polycrystalline.

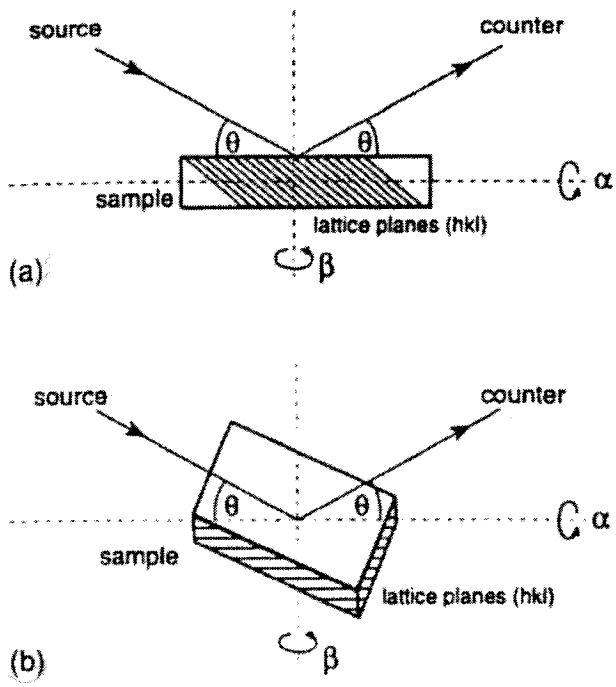

Figure 2 - 19. Sketch to illustrate the effect of sample rotation of the arrangement of the lattice planes: (a) untilled position ($\alpha = \beta = 0°$); (b) sample tilted such that the lattice planes are in Bragg condition ($\alpha > 0°$, $\beta > 0°$) [27].

The crystal is irradiated with monochromatic radiation and the detector is set at the angle 2θ with respect to the primary beam. Of course, a reflected intensity is only measured if the corresponding lattice planes are arranged such that they lie perpendicular to the

scattering vector that is the bisector of the angle between incident and reflected beams, as shown in Figure 2-19b, which means that in most cases no reflection is obtained from a single crystal (Figure 2-19a). In order to ensure reflection from other lattice planes, the sample has to be rotated and/or tilted until the lattice planes are in reflection condition. The necessary rotation and tilt angles are used to measure the arrangement of the lattice planes with respect to the external sample frame.

In order to determine an unknown crystal orientation in practical applications, the sample is systematically rotated in a texture goniometer about well-defined angles in such a way that all possible lattice planes are successively brought into the reflection condition and the reflected intensities are recorded as a function of these rotation angles.

2.2.2 Microtexture Measurement by Electron Backscattered Diffraction (EBSD)

Microtexture are commonly measured by Orientation Imaging Microscopy (OIM) to analyse the Electron Back-Scattered Pattern (EBSP) of a material. When an electron beam enters a crystalline solid, it experience inelastic scattering in all directions. This means that there must always be some electrons arriving at the Bragg angle θ_B at some set of lattice planes, and these electrons can undergo elastic scattering to give a strong, reinforced beam. These diffracted patterns are represented called the Kikuchi patterns, and consists of pairs parallel lines where each pair or 'band' has a distinct width and corresponds to a distinct crystallographic plane (Figure 2-20).

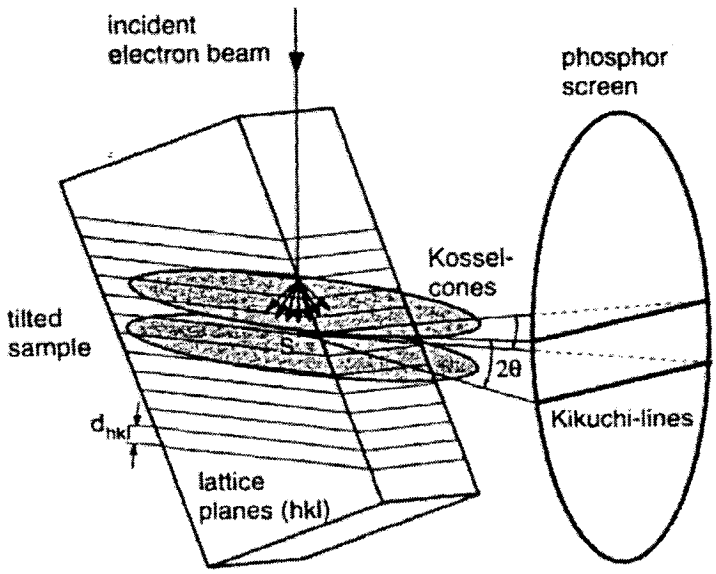

Figure 2 - 20. Schematic image of origin of Kikuchi lines from the EBSD (i.e. tilted specimen perspective) [27]

It is seen from Figure 2-21 that the two lines forming a given Kikuchi band in general have different intensities, and typically the line that is closer to the primary beam direction is darker (the 'defect' line) then the background, whereas the other one is brighter (the 'excess' line). The specimen is tilted about 60-70° to allow more electron to be diffracted and to be recorded. A digital camera captures the Kikuchi patterns projected onto the phosphor screen and computer software converts the bands in the Kikuchi pattern to Hough space for facilitating automatic band identification.

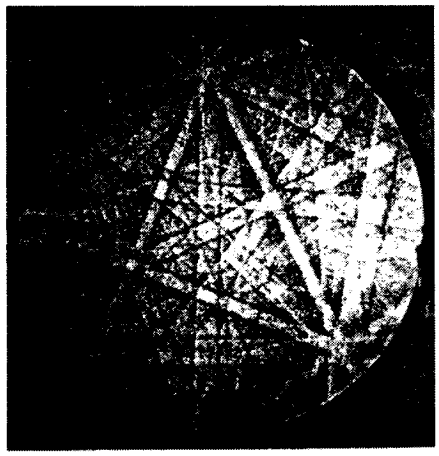

Figure 2 - 21. An example of Kikuchi patterns viewed under camera [27].

The angle and distance between the bands, the intensities and width of the bands also provide information on the symmetry, the atomic spacing and the angular relationship of crystal lattices. By scanning the electron beam across the specimen surface and recording the Kikuchi pattern at each specimen location, the software can construct a map of the spatial orientation distribution, texture components, type of interfaces between grains, orientation changes within grains, true grain size and shape distributions and deformation maps. Figure 2-22 illustrates an example of an OIM image of HCP material with its crystallites orientation marked with different colors.

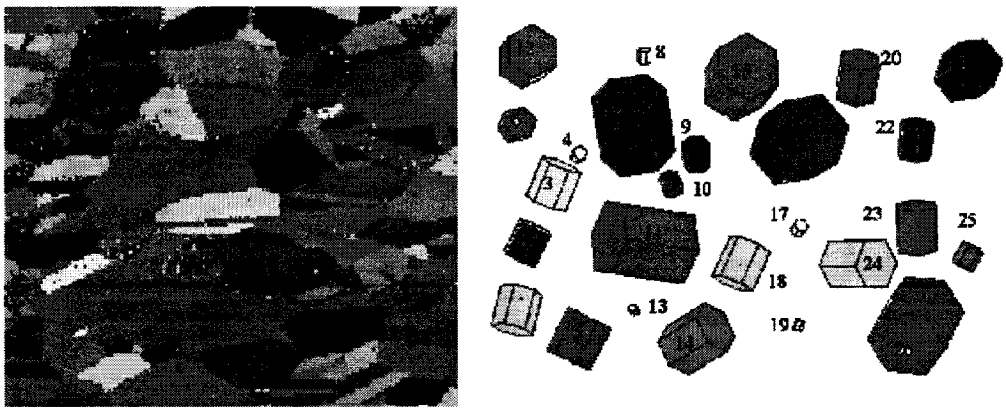

Figure 2 - 22. Illustration of OIM image of an HCP material with its relative crystallites orientation [35].

2.3 References

1. Doege, E et al., "Deformation of Magnesium", *Magnesium-Alloys and Technologies*, Wiley-VCM, 2003, pp.72-89.

2. Avedesian, M. M. & Bake h., ASM Specialty Handbook: Magnesium and Magnesium Alloys, *ASM international*, 1999, pp.7-29.

3. Kainer, K. U., "The current State of Technology and Potential for further Development of Magnesium Applications", *Magnesium-Alloys and Technologies*, Wiley-VCM, 2003, pp.1-22.

4. Al Wrigley: American Metal Market, Vol. 110, 2002.

5. Eds. Avedesian, M.M. and Baker, H.: *Magnesium and Magnesium Alloys* (ASM Specialty Handbook, 1999), pp. 98-102.

6. Chapman, J. A. and Wilson, D. V., *J. Inst. Metals,* Vol. 91, 1962.

7. Doege, E. and Droder, K., "Sheet Metal Forming of Mg Wrought Alloys - Formability and Process Technology", *J. Materials Processing Technology,* 115, 2001, pp. 14-19.

8. Enss, J., Everetz, T., Reier, T. and Juchmann, P., "Properties and Perspectives of magnesium Rolled Products," Magnesium Alloys and Their Applications, Ed. K.U. Kainer, Wiley-VCH, 26-28 September, 2000, Munich, Germany (DGM, Weinheim).

9. Krajewski, P., "Elevated Temperature Forming of Sheet Magnesium Alloys," SAE Paper No. 2001-01-3104, Warrendale, PA, SAE, 2001.

10. Siegert, K. and Jaeger, S., "Pneumatic Bulging of Magnesium AZ31 Sheet metal at Elevated Temperatures," Magnesium Technology 2004, Ed. Alan Luo, TMS, Warrendale, PA, 2004, pp. 87-90.

11. Takuda, H., Enami, T., Kubota, K., Hatta, N., "The formability of a thin sheet of Mg-8.5Li-1Zn alloy", *Journal of Material Processing Technology* ,101 ,2000, pp. 281 - 286.

12. Lee, S., Chen, Y.-H., Wang, J.-Y., "Isothermal sheet formability of magnesium alloy AZ31 and AZ61", *Journal of Material Processing Technology,* 124, 2002, pp.19 - 24.

13. Doege, E. and Droder, K., "Processing of magnesium sheet metals by deep drawing and stretch forming", *Mater. Technol.*, 7-8, 1997, pp.19 - 23.

14. Kohzu, M., Yoshida, F., Somekawa, H., "Fracture mechanism and forming limit in deep-drawing of magnesium alloy AZ31", *Mater. Trans.*,, 42, 2001, pp.1273 - 1276.

15. Nave, M. D., & Barnett, M. R., "Microstructures and textures of pure magnesium deformed in plain-strain compress", *Scripta Materialia*, v.5, 2004, pp.881-885.

16. Reed-Hill, R.E., Physical Metallurgy Principles, 2nd ed., 1973.

17. Barnett, M. R. et al., "Deformation microstructures and textures of some cold rolled Mg alloys", *Material Science and Engineering A*, v. 386, 2004, pp. 205-211.

18. Wang, Y. N., & Huang, J. C., "Texture analysis in hexagonal materials", *Material Chemistry and Physics*, v. 81, 2003, pp. 11-26.

19. Kaiser, F. et al., "Anisotropy Properties of Magnesium Sheet AZ31", *Material Science Forum*, v.419-422, 2003, pp. 315-320.

20. Agnew, S. & Duygulu, O., "A Mechanistic Understanding of the Formability of Magnesium: Examining the Role of Temperature on the Deformation Mechanisms", *Materials Science Forum*, v.419-422, 2003, pp. 177-188.

21. Barnett, M. R., "Influence of deformation conditions and texture on the high temperature flow stress of magnesium AZ31", *Journal of Light Metals*, v.1, 2001, pp. 167-177.

22. Barnett, M. R., et al., "Effect of Grain size on the Deformation and Dynamic Recrystallization of Mg-3Al-1Zn", *Material Science Forum*, v.465-470, pp.435-440.

23. Ohio State University

24. Interlacken User Manual

25. Chen, F.-K. and Huang, T.-B., "Formability of stamping magnesium-alloy AZ31 sheets", *Journal of Materials Processing Technology*, v.142, 2003, pp. 643–647.

26. Hatherly, M. & Hutchinson, W. B., "Introduction to Texture in Metals", pp.1-74.

27. Randle, V. & Engler, O., "Introduction to Texture Analysis Macrostructure, Microtexture and Orientation Mapping", *Gordon and Breach Science Publishe*rs, 2000, pp. 13-40, 61-152.

28. Course notes, MIME 367 Electronic Properties of Materials, Section: Texture, Professor Jerzy A. Szpunar

29. Chang, T.C. et al., "Grain-refining of magnesium alloy AZ31 by rolling", *Materials Processing Technology*, v.140, 2003, pp. 588-591.

30. Styczynski, A. et al., "Cold rolling textures in AZ31 wrought magnesium alloy", *Sripta Materialia*, v.50, 2004, pp. 943-947.

31. Rosenbaum, H. S., "Nonbasal Slip in h.c.p. Metals and its Relation to mechanical Twinning", *Metallurgical Society Conferences*, v.25, 1963, pp. 43-76.

32. Reed-Hill, R. E., "Role of Deformation Twinning in the Plastic Deformation of a Polycrystalline Anisotropic Metal", *Metallurgical Society Conferences*, v.25, 1963, pp. 295-320.

33. Smallman, R. E. & Bishop, R. J., Modern Physical metallurgy & materials Engineering, Butterworth Heinemann, sixth edition, 1999, pp.197-258.

34. www.ndt-ed.org

35. www.texture.de

Chapter 3

Research Materials and Experimental Equipments

3.1 Materials Used and Specimen Preparation

The AZ31 magnesium alloy was used in the present investigation. Varieties of AZ31 materials were studied (1) cast AZ31 alloy ingot from CANMET; (2) commercial AZ31 alloy sheet of 2.35 mm thick supplied by Spectrulite; (3) commercial AZ31 alloy sheets of 2.01 and 1.3 mm thick supplied by Magnesium Electron (MEL).

The specimens for metallographic examination and x-ray diffraction texture measurement were prepared by surface grinding with SiC papers to 1200 grit, and then polishing with diamond paste through grade of 3 μm and 1 μm. For microstructure analysis, the specimens were etched with a solution of 4.2 g picric acid, 10 ml acetic acid, 70 ml ethanol and 10 ml water until the change of color on the specimen surface (typical time

from 2 to 5 secs). For microstructural analysis, optical microscope (Nikon) with Clemex analysis software was used.

The sample preparation for examination with Orientation Imaging Microscopy (OIM) is difficult due to low density of Mg, and the Kikuchi diffraction patterns are not sharp enough. Therefore, a good surface finishing is crucial. Sample preparation includes electropolishing followed by grinding using in the final stage 1200 grit SiC paper. The electropolishing was carried out with an electrolyte of LiCl + $Mg(ClO4)2 \cdot 6H2O$ + Cellosolve + Methanol at -15°C.

3.2 Equipments Used in Investigation

3.2.1 Elevated Temperature Tensile Machine

Tensile testing was performed at General Motors, Materials Processing Laboratory in Research and Development Center, Warren, US. The test was performed at high temperature under constant strain rate in a screw-driven Instron 5568 machine equipped with an air circulating furnace. Figure 3-1 depicts the tensile machine used. Bluehill data acquisition software was used to analyze the results.

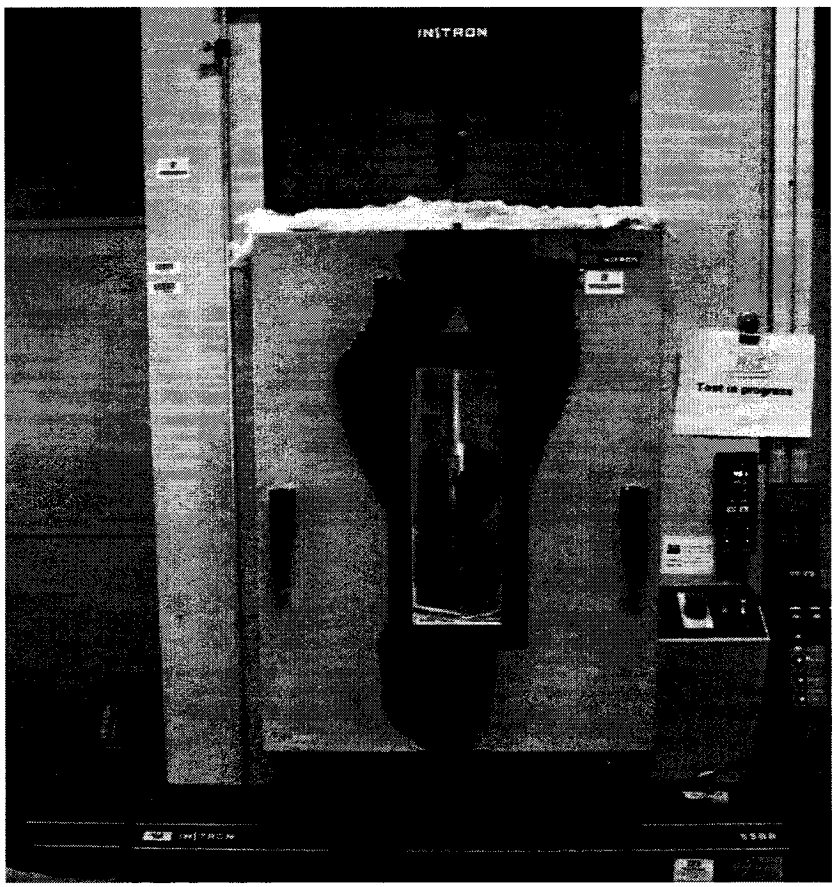

Figure 3 - 1. Instron 5568 tensile machine equipped with an air circulating furnace.

3.2.2 Compression Machine

Compression test was conducted with a closed-loop, serve-hydraulic MTS test machine of 100 kN full capacity (Figure 3-2). Load measurement was performed using a 25 kN load cell. Displacement of the hydraulic actuator was measured from the output of a linear variable differential transformer (LVDT).

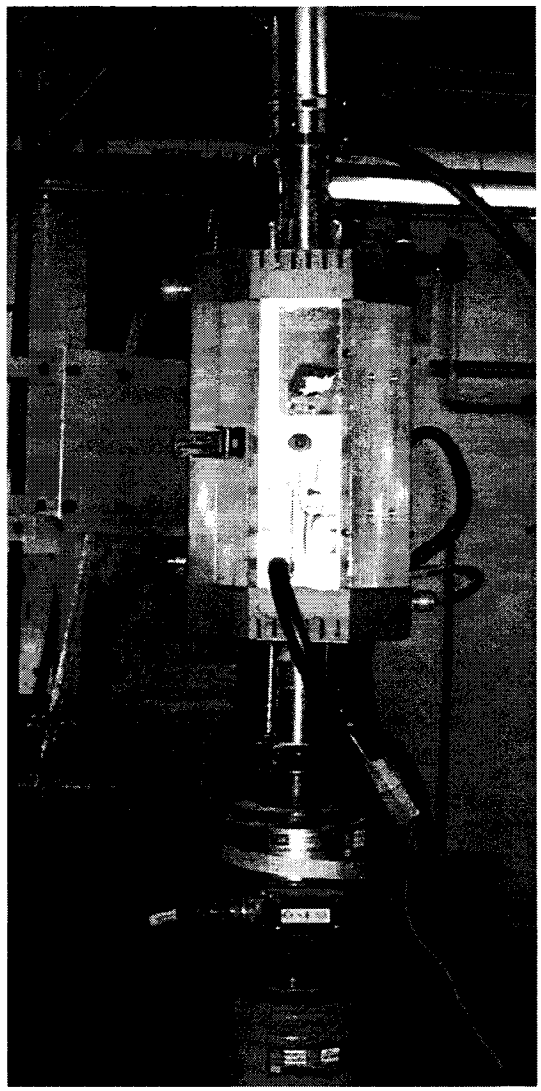

Figure 3 - 2. MTS compression machine

3.2.3 Forming Press Machine

Forming testing was performed at General Motors, Materials Processing Laboratory in Research and Development Center. For generating a forming limit diagram (FLD) for Mg alloys Limiting Dome Height (LDH) test at high temperature was performed. Figure 4 depicts Interlaken ServoPress 150 machine and its tooling. The circled part in Figure 4b shows the tooling used for LDH test. Control and data acquisition of the LDH test was

conducted using UniTest software and FLD was generated with an aid of Grid Pattern Analyzer GPA 3.0.

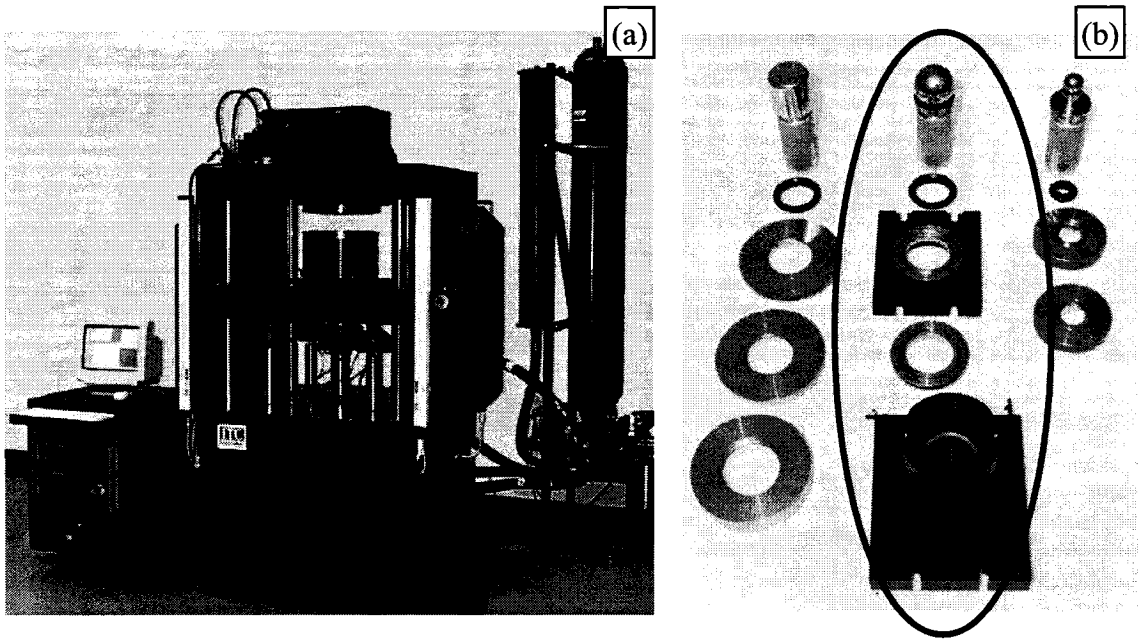

Figure 3 - 3. (a) Interlaken ServoPress 150 machine and (b) its tooling.

3.2.4 Optical Microscope

Optical metallography was performed on the etched samples using a Nikon EPIPHOT microscope equipped with a digital camera and the grain size analysis was performed by line-intercept method using Image Pro software.

3.2.5 X-Ray Diffractometer

Crystallographic texture measurement was carried out using Siemens D-500 x-ray diffractometer equipped with texture goniometer using Mo radiation (Figure 3-4). The (0002), $(1\bar{1}00)$ and $(10\bar{1}1)$ pole figures were collected on a 5° grid up to 80° sample tilt. The data were analyzed using Textool software to calculate orientation distribution

functions and poles figures.

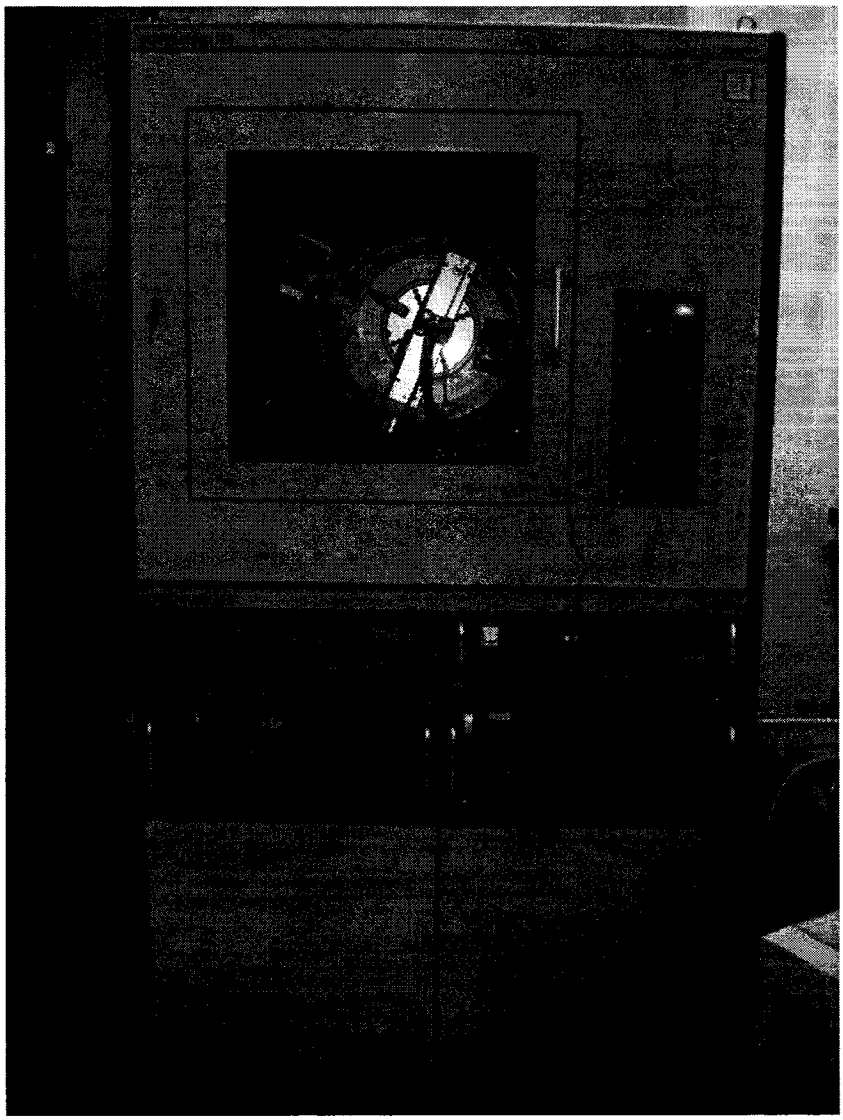

Figure 3 - 4. Siemens D-500 x-ray diffractometer

3.2.6 Orientation Imaging Microscope

Local texture was examined by orientation imaging microscopy (OIM). The system used consists of Philips XL30 S FEG Scanning Electron Microscope (SEM) equipped with EDAX (model) electron backscatter pattern (EBSP) detector (Figure 3-5). The resulted data were analyzed with TSL analysis software.

Figure 3 - 5. Philips XL30 S FEG Scanning Electron Microscope (SEM) equipped with EDAX (model) electron backscatter pattern (EBSP) detector

Chapter 4

Deformation Modes in AZ31

4.1 Introduction

Deformation modes of Mg crystals are mainly basal slip, prismatic slip, pyramidal slip and twinning. The activation of these deformation modes depends on their CRSS (critical resolved shear stress) value and the lattice orientation. In pure magnesium, at room temperature, basal slip has the lowest CRSS value among all deformation systems, while CRSS for pyramidal <c+a> slip has the highest, approximately 2 orders of magnitude larger than that of basal slip. Hence deformation at room temperature is poor for magnesium alloys. However, above 225°C, additional slip systems become thermally activated and magnesium becomes highly deformable. Graphical representation of CRSS as function of the temperature is presented in Figure 2-8.

There is no doubt that crystallographic texture plays an important role for plastic

deformation of metals with HCP structure. Several researchers have studied texture as a means to characterize the formability of HCP materials however a systematic texture analysis of magnesium is still missing. Therefore, the aim of this chapter is a more profound understanding of the role of texture and microstructure on deformation of magnesium AZ31 alloy at and above ambient temperatures. Thereby a preliminary investigation was initiated to observe and evaluate the metallographic changes following uniaxial compression of AZ31 cast material.

4.2 AZ31 CANMET Cast Ingot

The preliminary objective of this investigation is to observe and evaluate the metallographic changes following uniaxial compression of AZ31 cast material. The cast material was chosen because of its large grains that ease the metallographic examination. The AZ31 cast material, supplied by CANMET, was cast from a permanent Cu mould. Cylindrical specimens with a diameter of 7.65 mm and height of 11.6 mm were machined out of the cast ingot as shown in Figure 4-1.

Eight specimens were investigated in this study. Specimens were compressed at different temperatures from room temperature to 450°C at the initial strain rate of $0.01s^{-1}$. Prior to the compression test, the specimens were polished from one side of circular surface, as shown in Figure 4-1. After deformation the specimens were water quenched to stop any further changes in the deformation microstructure and texture. The list of the various test conditions is shown in Table 4-1.

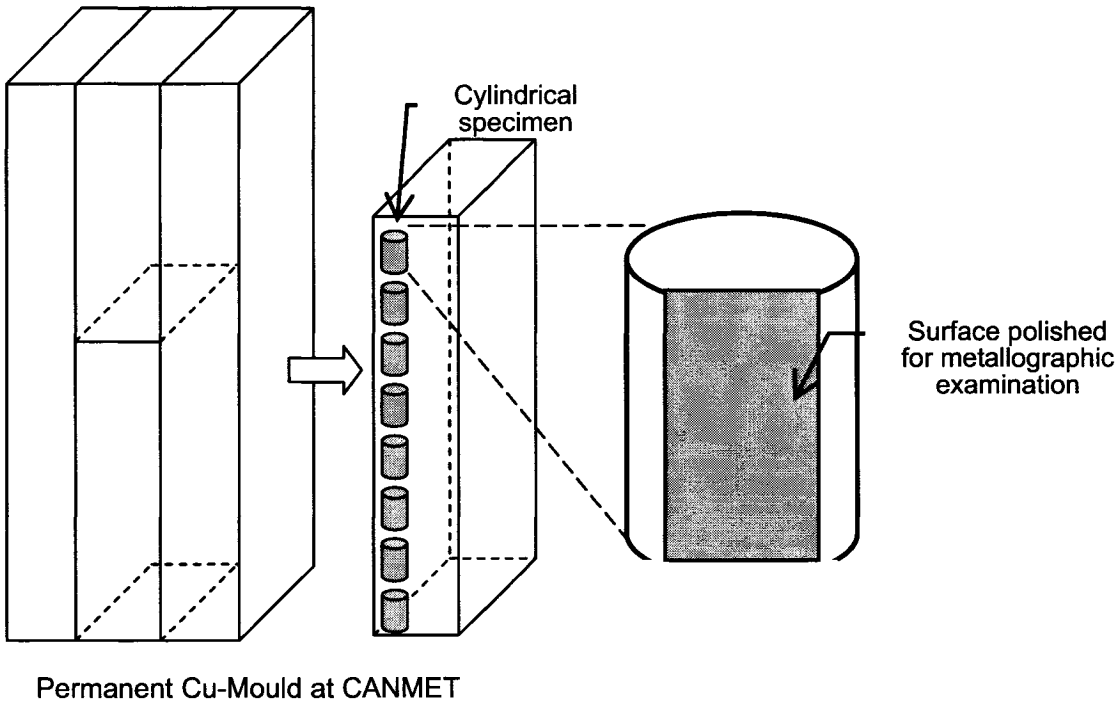

Figure 4 - 1. Cylindrical specimens from the CANMET permanent Cu-mould.

There were two set of test conditions: set 1 was conducted to compress to a strain of 0.4 without interruption and set 2 was conducted to compress the specimen to small amounts of strain (~0.1)[1] and then removed from the compression machine for metallographic examination. The 0.4 strain applied to specimens of set 1 is designed to show the texture of deformed material whereas the small amount of strain applied to specimens of set 2 is designed to review the evolution of microstructure during deformation. Because compression generates a wavy surface, specimens of set 2 were polished again prior to each compression test to maintain the flat surface for further microstructure analysis.

[1] Since the MTS compression machine is less sensitive at low strain, the amount of strain applied to the specimens deviates ±0.04 of the chosen value (0.1).

Table 4 - 1. List of compression specimens and test conditions investigated.

Specimen	*Temperature (°C)*	*Strain Rate (s^{-1})*	*Test Condition*
A1	Room Temperature	0.01	Compression to 0.4 strain
B1	250°C	0.01	
C1	350°C	0.01	
D1	450°C	0.01	
A2	Room Temperature	0.01	Compression to 0.1 strain per test for cumulative strain of 0.3 strain
B2	250°C	0.01	
C2	350°C	0.01	
D2	450°C	0.01	

4.3 Microstructure and Texture Evolution During Recrystallization of AZ31 (Specimen Set 1)

The microstructure and texture of the non-deformed and the deformed specimen are shown in Figure 4-2. The texture of the initial cast material shows that the c-axes of the grains are randomly orientated with respect to the cylinder axis.

As shown in Figure 4-2a, the grains of the cast ingot are very large, ranging from 500 μm to 900 μm, limiting the number of grains in each cylindrical specimen. These results have relatively poor statistics for the texture measurement. Hence cylinders compressed at room temperature and at 450°C were sectioned into several slices and texture of each slice was measured. Texture measurements were then combined to obtain statistically reasonable results. Figures 4-2d and 4-2f show the basal plane pole figures where a subtle orientation of the (0001) plane is revealed.

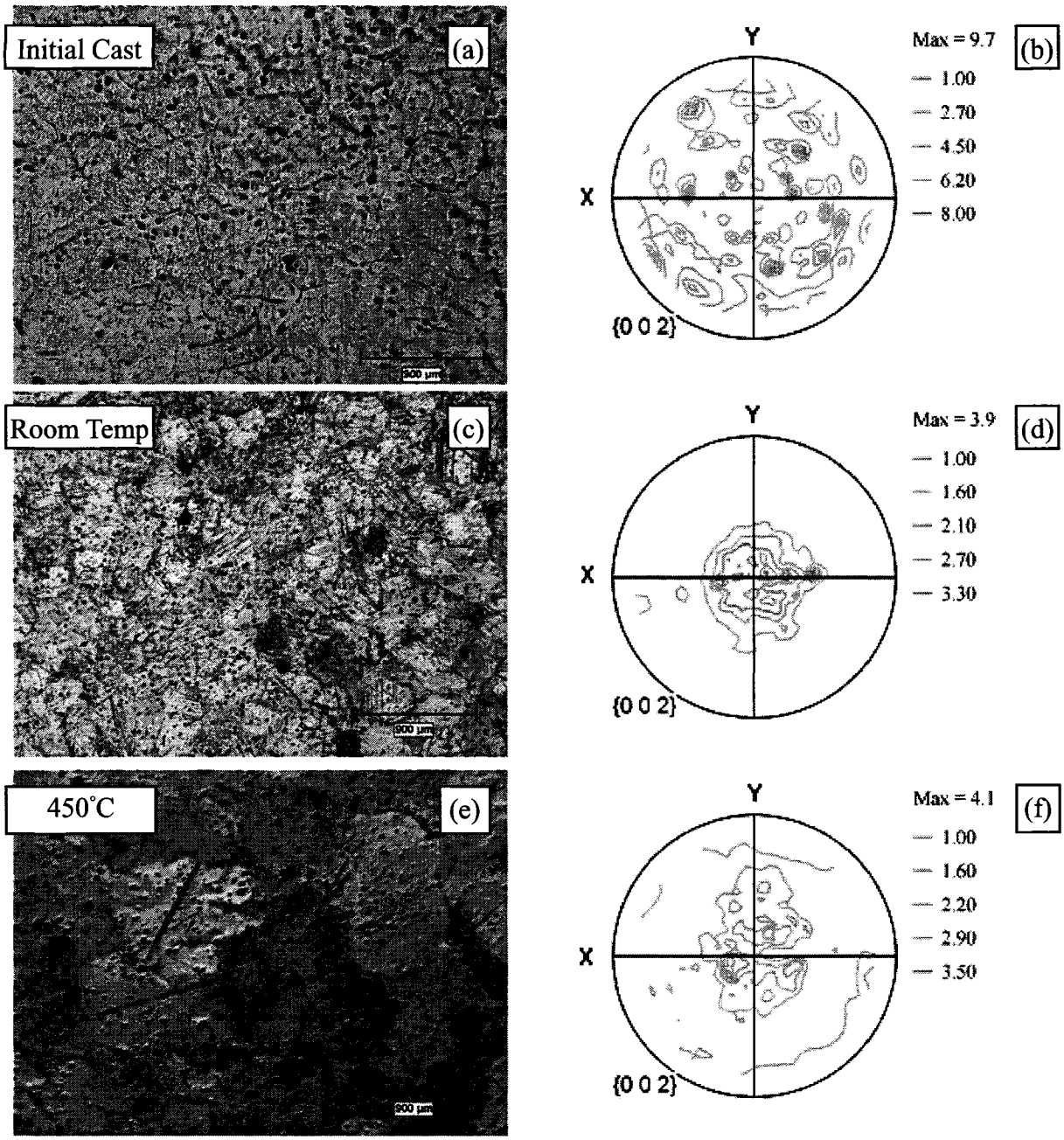

Figure 4 - 2. Microstructure and Texture compressed specimens of set 1. (a)and (b) Initial cast; (c) and (d) Cylinder compressed at room temp. with ε=0.4; (e) and (f) Cylinder compressed at 450°C with ε=0.4.

At room temperature, only basal slip and twinning[2] are responsible for the deformation

[2] There are a variety of twinning systems in Mg, but the twinning system that has been mainly observed is as the so-called "tensile" twin.

mechanisms (Figures 4-3a and 4-3b) because their CRSS are much lower than the CRSS for prismatic and pyramidal slip (Figure 2-8). These two mechanisms cause a rotation of the c-axis towards the compression axis (Figure 4-2d). In the case of basal slip there will be a gradual reorientation of the c-axes, whereas in the case of twinning there will be a sudden orientation change: the basal plane of the twin will be rotated 86.3° around a $\langle 11\bar{2}0 \rangle$ axis with respect to the basal plane in the original grains. Once the basal texture is established, both basal slip and twin system cease their contribution to deformation.

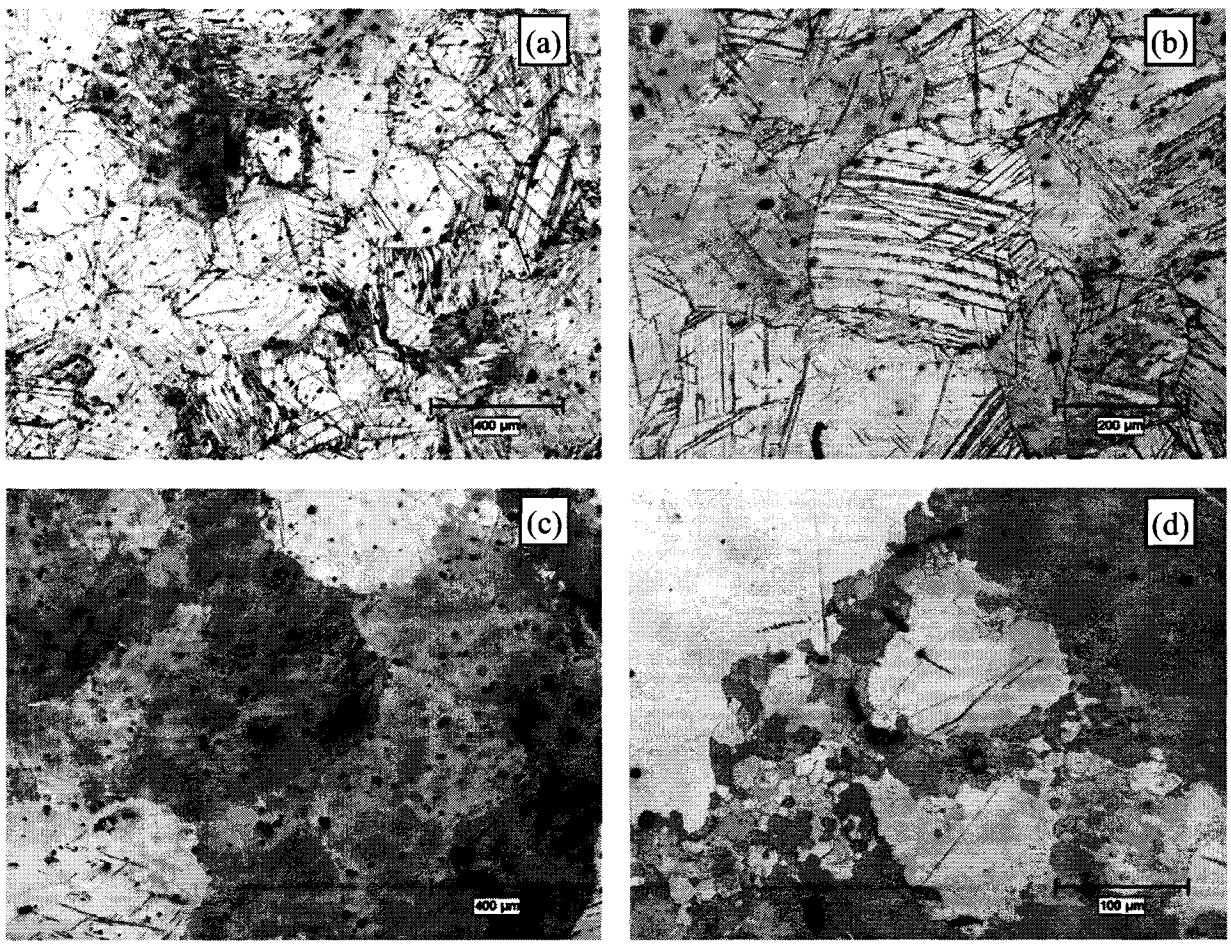

Figure 4 - 3. Detailed microstructures of the compressed cylinders of set 1. (a) and (b) twins revealed for compressed specimen at room temperature; (c) and (d) Recrystallized grains around the prior grain boundaries for specimen compressed at 450°C.

At higher temperatures, the prior grain boundaries are found to be decorated by small recrystallized grains, which often named as the necklacing phenomenon (Figure 4-3d). The recrystallization of Mg alloys is usually not accompanied by an obvious change of crystallographic texture because the recrystallization texture also reveals the basal texture of the deformed Mg [1]. Regardless of the initial orientation distribution, a basal texture (basal plane normal to the deformation axis) readily develops during compression due to the mechanism of crystallographic slip and twinning (Figure 4-2f).

4.4 Observations of Compression Surfaces After Deformation at Different Temperatures (Specimen Set 2)

4.4.1 Deformation Modes

In general, all the slip-bands in each grain were parallel with a set of parallel twins lying diagonal to the slip lines as shown in Figure 4-4b. The slip lines seemed to be "lighter" and were separated by a very small interval, whereas the twins seemed to be "darker" and separated by a large interval. This was mostly observed in the less constrained areas as indicated in white in Figure 4-4a. At the bottom center of the cylinder in the grey area, where deformation is constrained, the slip lines were more complex, i.e. one observe different slip line directions within a grain (Figure 4-4c). This phenomenon gradually became more obvious with increasing amount of strain (Figure 4-4d). The complexity of slip lines might suggest activation of additional slip systems such as prismatic and pyramidal.

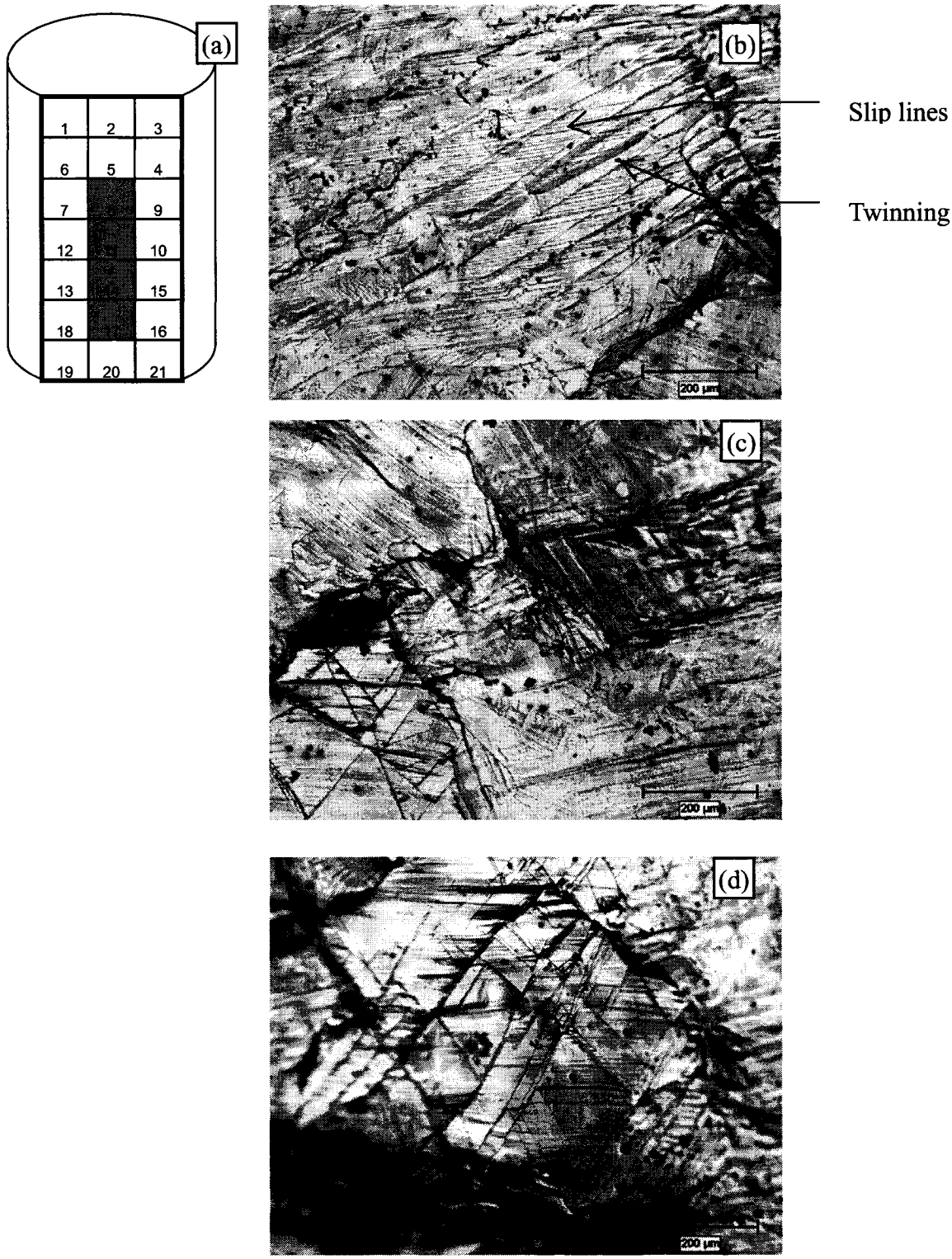

Figure 4 - 4. (a) Area identification in the cylindrical specimen. White are non constrained areas and grey are constrained areas; (b) Slip lines and Twinning. 250°C and ε=0.16 at 100x of area 6; (c) Complex slip lines. 250°C and ε= 0.16 at 100x of area 14; (d) Complex slip lines. 250°C and ε= 0.24 at 100x of area 14.

Slip occurs in specific directions on certain crystallographic planes. Generally the slip plane is the plane of greatest atomic density, and the slip direction is the closest-packed direction within the slip plane. Since magnesium has a ratio c/a = 1.624 which is close to the ideal ratio of the close packed spheres c/a (ideal) = 1.633, basal slip and mechanical twinning are easy and strongly preferred among all slip systems. Less densly packed slip planes or even larger burgers vectors are more difficult to activate; therefore slip systems, such as prismatic slip and pyramidal slip, operate only at a higher critical resolved shear stress. Hence, below 225°C, only basal plane slipping is possible, along with twinning, and above 225°C, prismatic slip and pyramidal slip are activated.

In the case of the specimen deformed at room temperature, the basal slip line and twinning were the main deformation mechanism as illustrated in Figure 4-5a. Whereas for the specimens deformed at higher temperatures (250°C, 350°C and 450°C), less twinning was observed (Figures 4-5b and 4-5c).

Cross slip was observed at 250°C after strain of 0.16 (Figure 4-6). This phenomenon implies that the stresses at this deformation condition become high enough for dislocations to bypass the obstructions by cross slip, which is a motion of dislocations on a plane inclined to that on which they were moving previously. This might also explain the lower rate of work hardening at high temperature compared to that at room temperature.

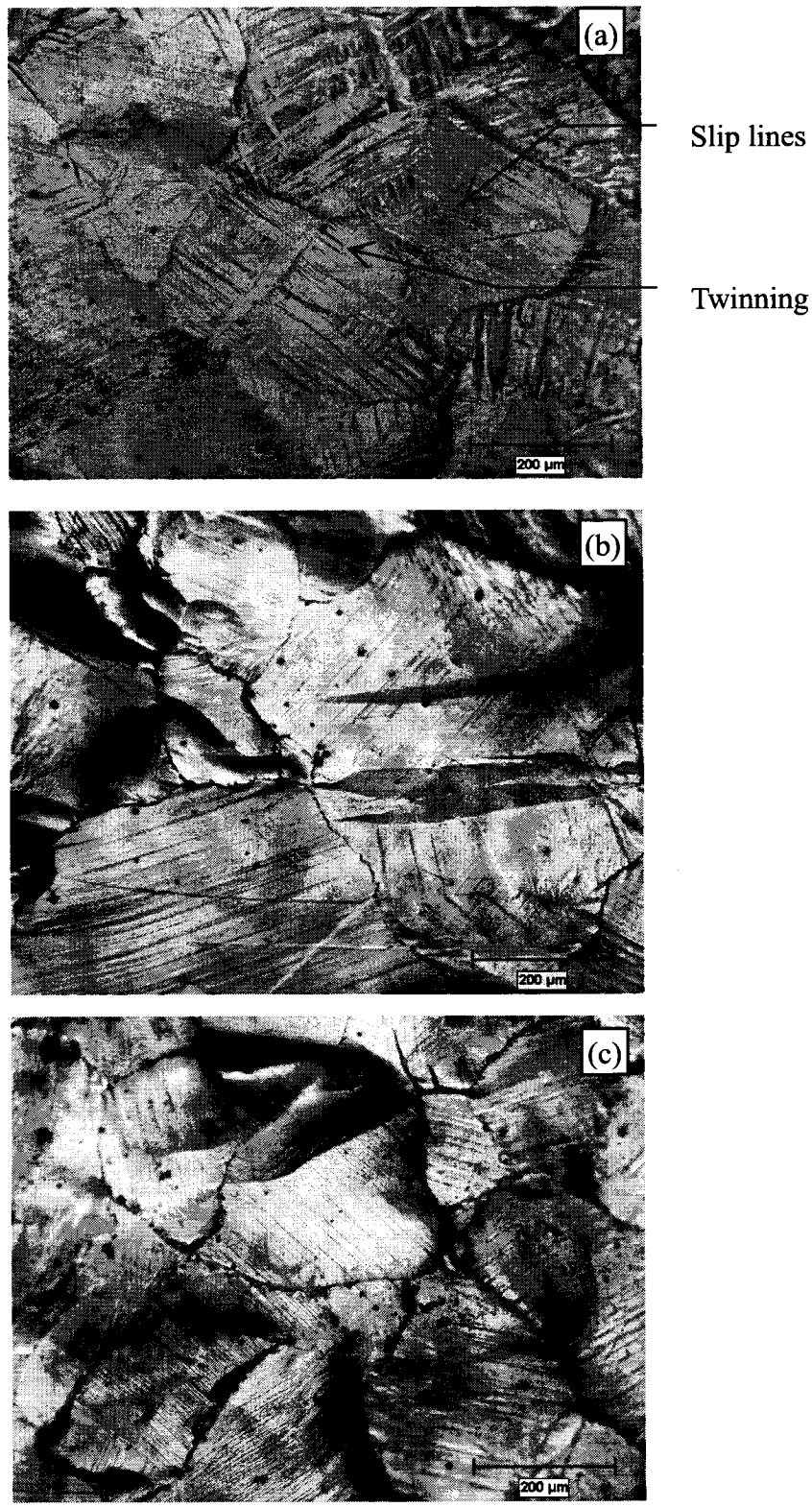

Figure 4 - 5. (a) Slip line and twins. Room temp. and ε= 0.12 at 100x of area 11; (b) Slip line and few twins. 350°C and ε= 0.08 at 100x of area 9; (c) Mainly slip lines. 450°C and ε= 0.09 at 100x of area 14.

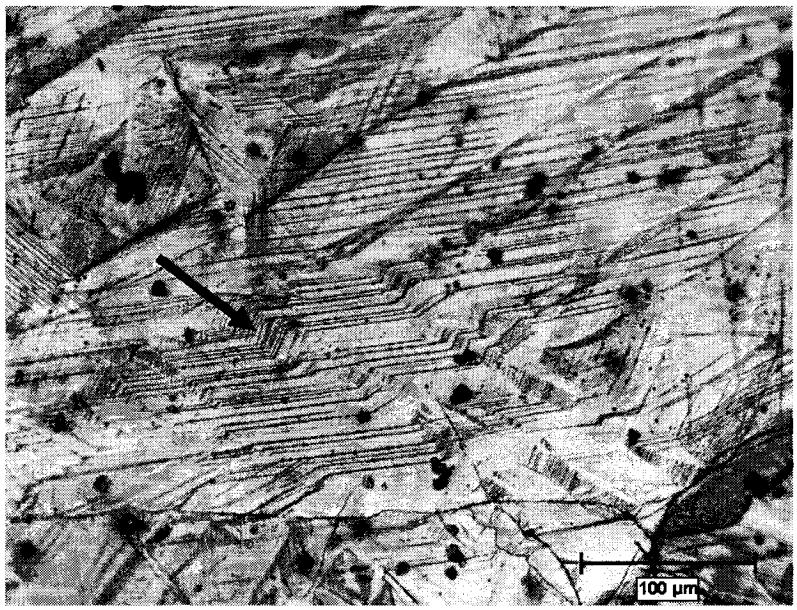

Figure 4 - 6. Cross slip. 250°C and ε=0.16 at 200x of area 6.

When high strains were applied, the subgrains were observed at higher temperatures (Figure 4-7a). The formation of these subgrains is known to be the phenomenon of polygonization. The process of these subgrains coalescence is important since the development of these enlarged sub-grains adjacent to high-angle boundaries, which are mobile, provides the crucial steps in the nucleation of recrystallization [2]. This is the first time in this entire program that this type of recrystallization has been observed. The usual mechanism is necklacing, which was also observed in these tests (Figure 4-7b).

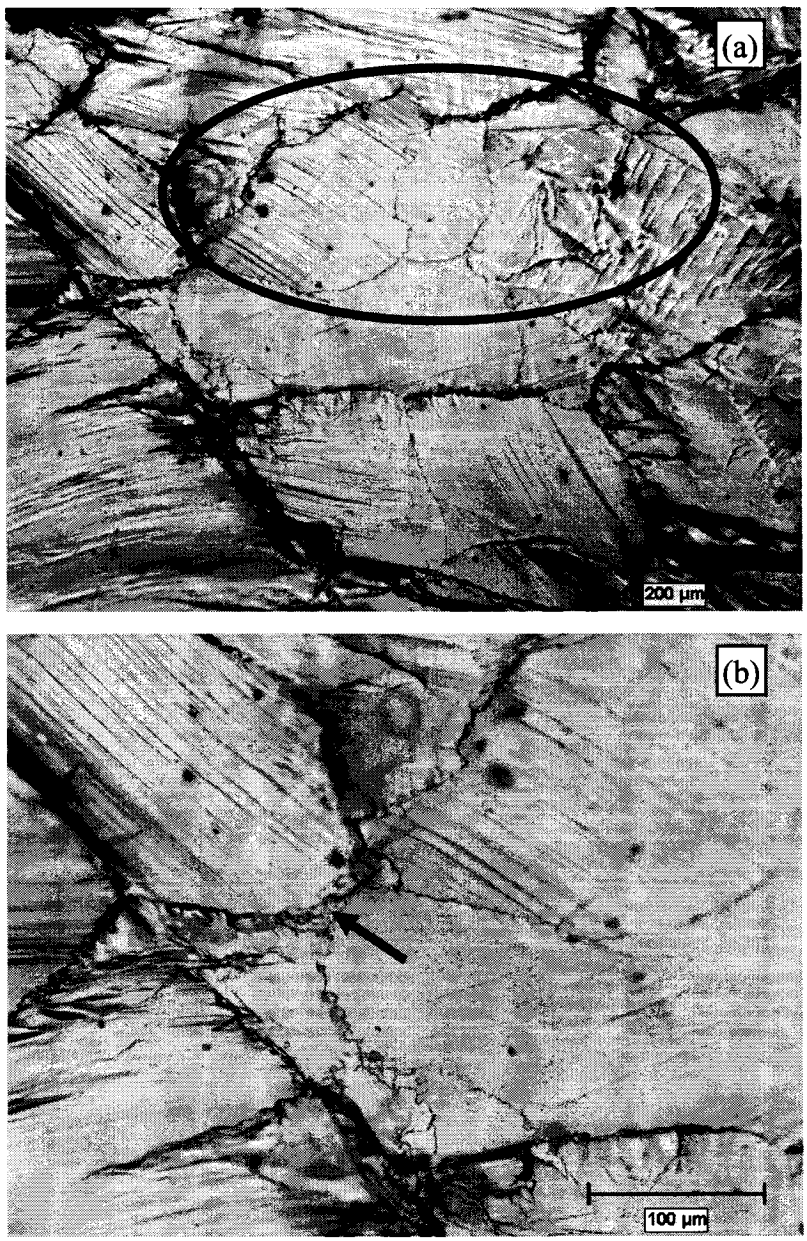

Figure 4 - 7. (a) Polygonization. 350°C and ε= 0.28 at 100x of area 9; (b) Necklacing. 350°C and ε= 0.28 at 200x of area 9.

4.4.2 Twinning

In the present study, it was possible to clearly reveal twin formation at slip planes crossing. This is illustrated in Figure 4.8a for the specimen deformed at room temperature (Figure 4-8a). The schematic drawing, Figure 4-8b, illustrates the relative orientations of

the slip lines and the twinning planes.

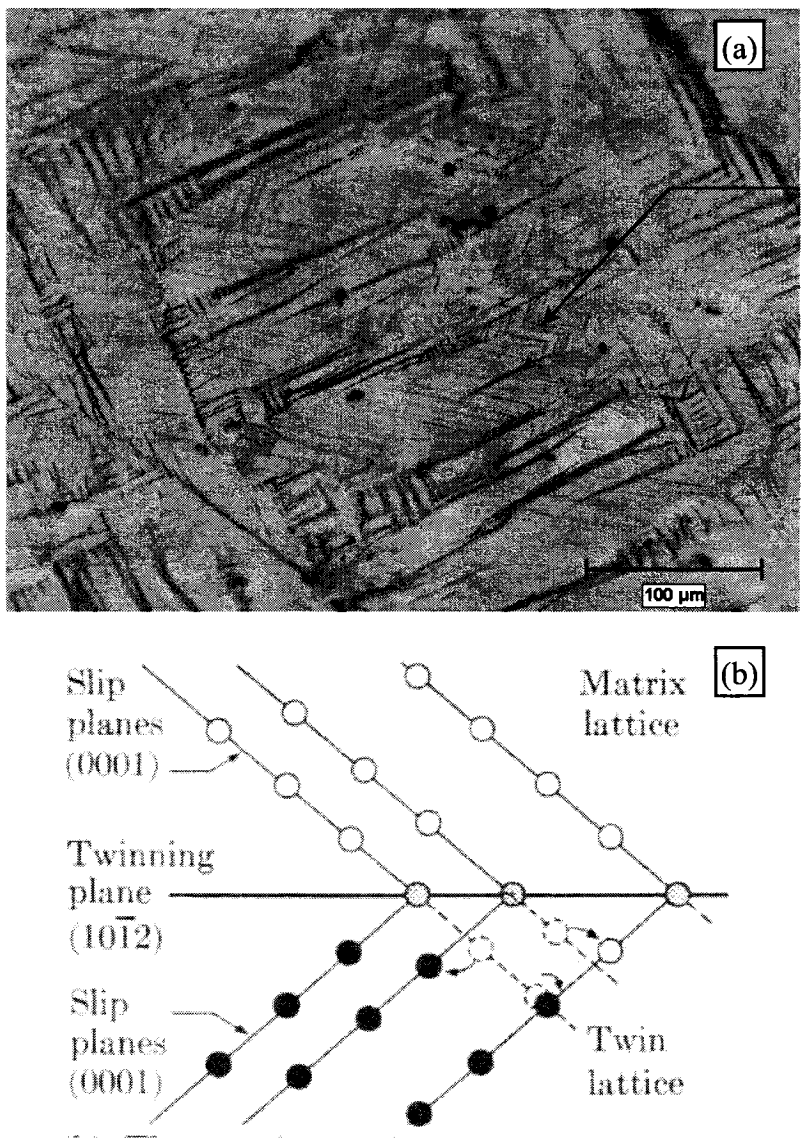

Figure 4 - 8. Twinning. (a) Room temp. and ε= 0.12 at 200x of area 4; (b) Atomic positions near twinning plane in (a) [3].

Since slip cannot continue as the only deformation mode at room temperature, twinning becomes significant at very low strain ($\varepsilon < 0.2$). The most obvious feature of the microstructure of deformed Mg at room temperature is the rapid development of profuse

arrays of large, broad, lenticular deformation twins. The twins originate usually as long, thin lamellae at low strain levels, but broaden rapidly at higher strain. Twin broadening in Mg is related to the smaller value of the twinning shear. Despite their profusion in the microstructure the contribution of twinning to the overall deformation at medium to high strain levels is usually small. The reason for this lies in the limited magnitude of the twinning shear. Table 4-2 gives details of the twinning systems in HCP.

Table 4 - 2. Twinning system in HCP metals [4].

Metal	c/a	Twinning shear	Twinning element	
			Plane	Direction
Cd	1.89	0.17		
Zn	1.88	0.14	$\{10\bar{1}2\}$	$\langle 10\bar{1}1\rangle$
Co	1.62	0.13		
Mg	1.62	0.13	$\{10\bar{1}2\}$	$\langle 10\bar{1}1\rangle$
Zr, Ti	1.59	0.167	$\{10\bar{1}2\}$	$\langle 10\bar{1}1\rangle$

The strain produced by the twinning shear depends on the twinning system and the value of c/a. For metals with c/a < ideal, such as Mg, deformation twinning is found in all grains at a very early stage, where they looks broad and lenticular. Because of the small twinning shear, further deformation requires the formation of smaller twins between and within those first formed. When this is not longer possible, fresh twins do not form at moderate strain. At high strain levels, shear bands begin to form (Figure 4-9).

As mentioned previously, there are several mechanical twinning systems in Mg, namely $\{10\bar{1}2\}$ tensile twins, $\{10\bar{1}1\}$ compression twins as well as double twinning, involving $\{10\bar{1}1\}$ followed by $\{10\bar{1}2\}$ twinning (Figure 2-4). However, only $\{10\bar{1}2\}$ tensile twin

seemed to be observed in this work. This might be due to its lower twinning shear compared to other twinning systems.

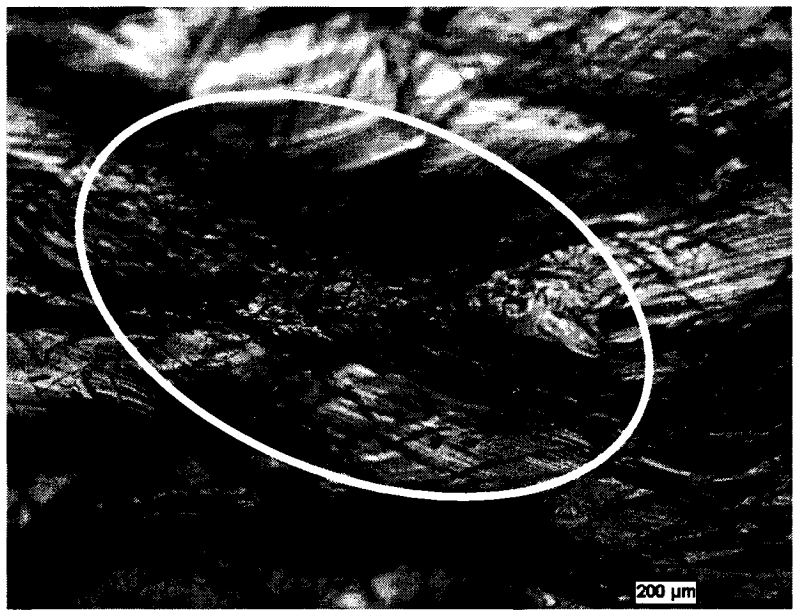

Figure 4 - 9. Shear bands. Room temp and ε=0.18 at 100x area of 17.

4.4.3 Grain Boundary Shearing

At room temperature, the existence of grain boundary shearing was observed. At strains as low as 0.12, shear displacement was observed across the grain boundary between grains A and B as shown in Figure 4-10a. Continued straining caused an increase in the amount of grain boundary shearing in this region as well as the introduction of grain boundary shears in other regions of the specimen. In most cases where grain boundary shearing was evident, fracture took place (Figure 4-10b).

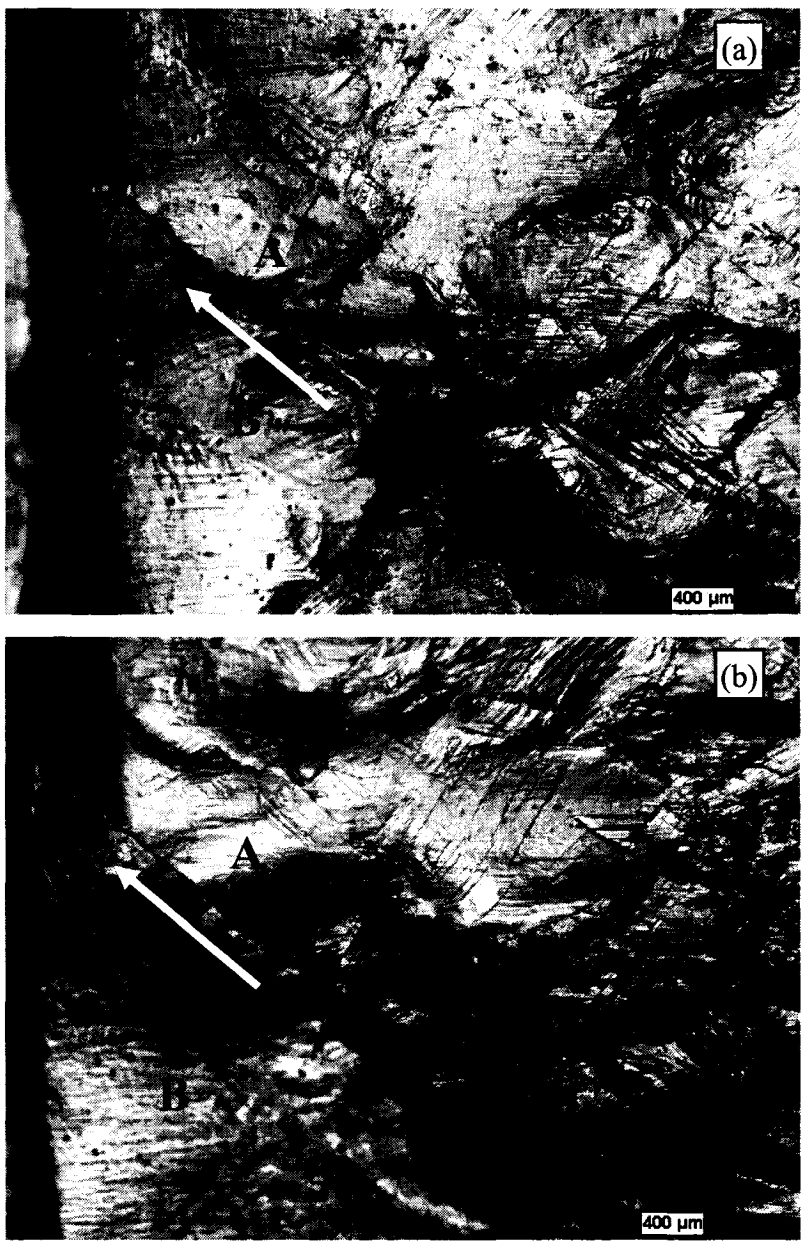

Figure 4 - 10. (a) Grain boundary shearing. Room temp. and ε=0.12 at 50x area of 13; (b) Fracture. Room temp. and ε=0.18 at 50x area of 18.

4.5 Summary

At room temperature, only basal slip and twinning contribute to deformation; however they cease to operate when basal texture is established. The twins are seen from the surface metallographic examination; they are believed to be $\{10\bar{1}2\}$ tensile twins characterized by the broad morphology because of smaller value of twinning shear. These twins are formed at low strain level and continue until straining shear bands begin to form. When grain boundary shearing is becoming evident, the cracks are formed.

In high temperature and high strain deformation condition, polygonization (i.e. sub grain formation) and necklacing are observed. The recrystallization texture is found to be the basal texture (basal plane perpendicular to the axis of compression). When deformation is constrained and / or amount of strain is increased, the slip lines are more complex. The complexity of slip lines might imply activation of additional slip systems (prismatic and pyramidal).

4.6 References

1. Hsu, E., Formability of Magnesium Alloys, McGill / GM Internal report, 4th quarterly, 2005.
2. Doherty, R.D. and Szpunar, J.A., "Kinetics of Sub-grain Coalescence – A Reconsideration of the Theory", *Acta metall.* , Vol. 32, No. 10., 1984, pp. 1789-1798.
3. Hren, G., Elements of Physical Metallurgy, Addison-Wesley, 3rd ed., 1974, pp. 120-140.
4. Dieter, G.E., Metallurgy and Metallurgical Engineering Series, McGram-Hill Book Company, 1961, pp. 81-117.

Chapter 5

Study of Deformation and Failure Mechanisms of AZ31 Sheet at Elevated Temperatures

5.1 Introduction

This chapter will be focused on investigation of temperature and strain rate effect on deformation mechanism and fracture mechanism in commercial AZ31 sheet.

5.2 Tensile Deformation of Commercial AZ31 Sheet

A commercial AZ31 magnesium sheet alloy, supplied by Spectrulite Consortium[3], was selected for this part of study. The sheet was 2.35 mm in thickness. Figure 5-1 shows the micrographs of the as-hot rolled AZ31 sheet in the as-received condition, which shows a heavily deformed microstructure consisting of twins and deformation bands. Figure 5-2a[4] shows the microstructure of the material after heat-treatment of 450°C for 6min, the average grain size is about 20 μm. Figure 5-2b is the respective texture of heat treated specimen, where strong basal texture is revealed. The composition of the AZ31 sheet is shown in Table 5-1.

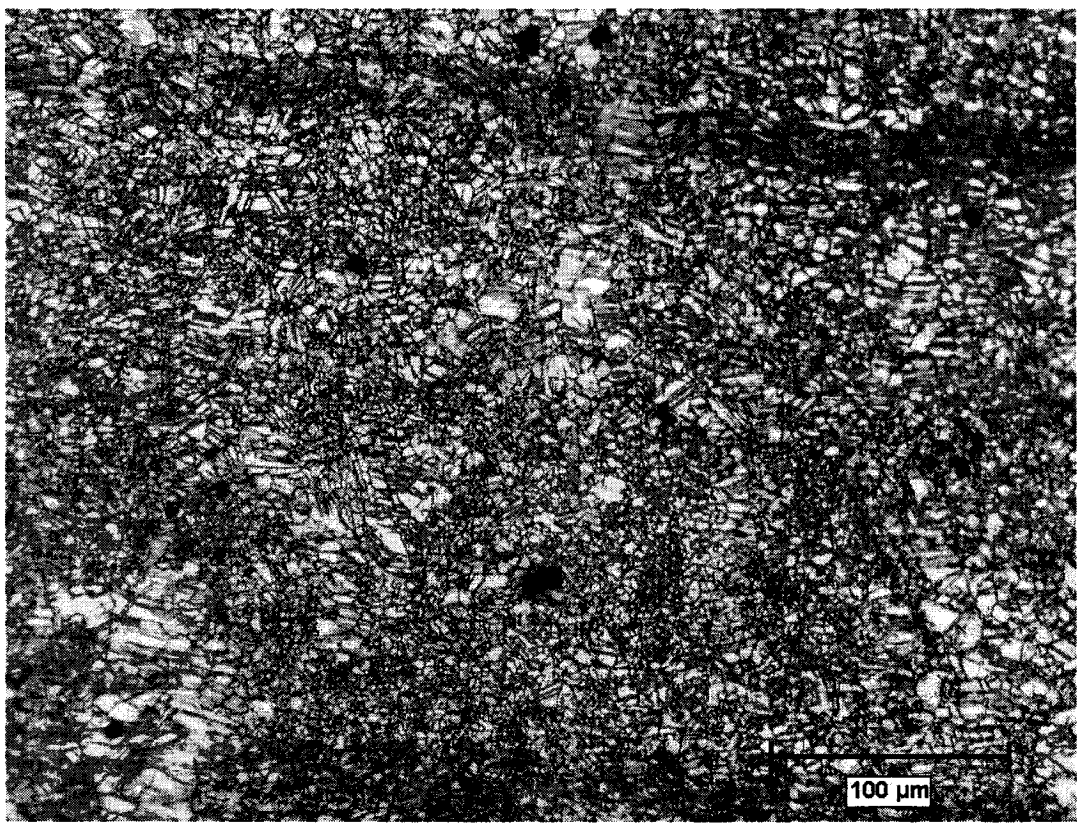

Figure 5 - 1. Micrographs of the as-hot rolled AZ31 sheet in the as-received condition.

[3] Former company of Magnesium Electron (MEL). Similar material used in later chapters, but came from different batch.

[4] Figure 1b is shown for reference purpose. The tested specimens were not all treated at this temperature.

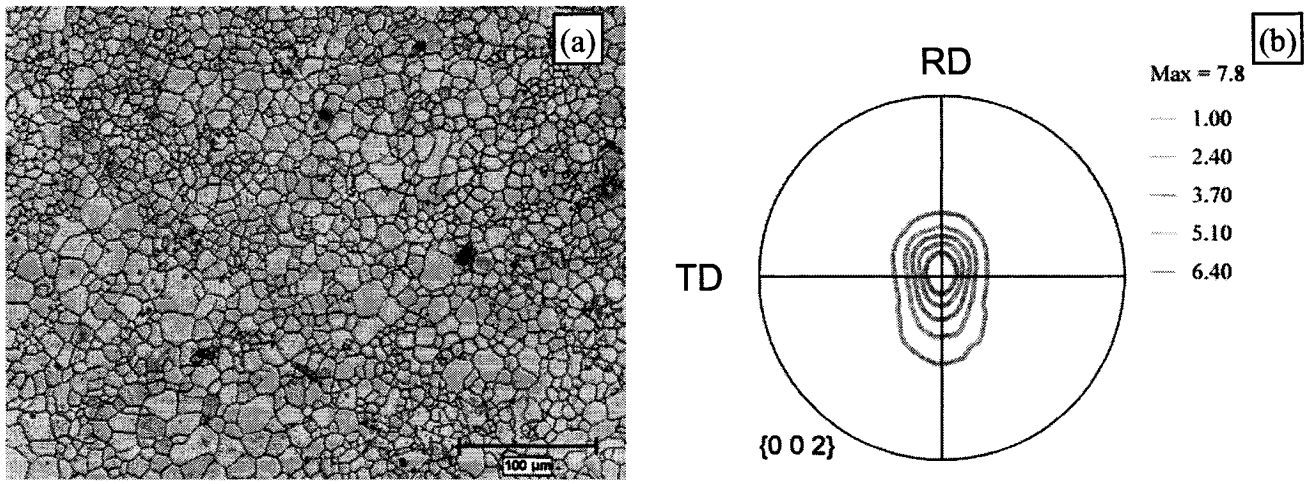

Figure 5 - 2. Micrographs of the AZ31 sheet after heat-treatment of 450°C for 6min: (a) microstructure and (b) texture.

Table 5 - 1. Chemical Composition of AZ31 sheet material in wt%. Commercial AZ31 sheet supplied by Spectrulite.

Element	*wt%*
Al	3.2
Zn	0.92
Mn	0.48
Si	< 0.1
Fe	< 0.005
Cu	< 0.003
Ni	< 0.003
Ca	< 0.01
Be	< 0.005
Mg	balance

The dog-bone shape test specimens were cut from the commercial AZ31 sheet with the tensile axis parallel to the sheet rolling direction. The initial dimensions of the specimen gage section are 6 mm wide x 25 mm long, which follows ASTM E2448-06 specification (Figure 5-3). Tensile tests were performed in an Instron 5568 equipped with an

air-circulating furnace. Samples were heated to the test temperature in about 15 minutes. The tensile tests were conducted at the temperatures from 300°C to 450°C, and the initial strain rates ranging from $0.001s^{-1}$ to $0.1s^{-1}$. The list of the various test conditions is shown in Table 5-2.

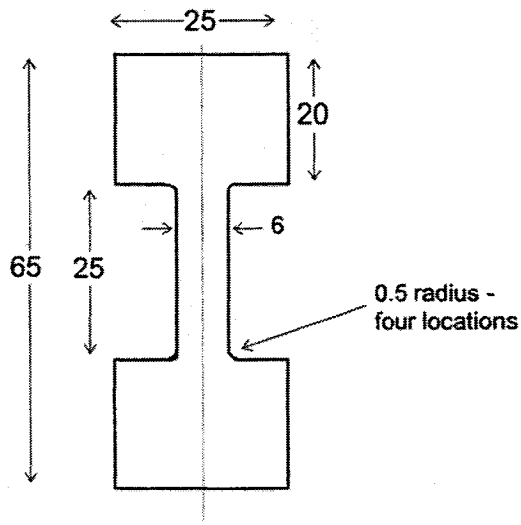

Figure 5 - 3. Tensile test specimens per ASTM E2448-06 [1]

Table 5 - 2. List of tensile specimens and test conditions investigated.

Specimen	***Temperature (°C)***	***Strain Rate (s^{-1})***
MgA	300	10^{-3}
MgB	300	10^{-2}
MgC	300	10^{-1}
MgD	400	10^{-3}
MgE	400	10^{-2}
MgF	400	10^{-1}
MgG	450	10^{-3}
MgH	450	10^{-2}
MgI	450	10^{-1}

5.3 Macroscopic Examination of Fracture Behavior

An untested tensile specimen and specimens tested to failure and its relative elongation under various conditions are shown in Figure 5-4. As expected, the maximum elongation of 362% was obtained at 450°C and $0.001s^{-1}$, which is at the highest temperature and slowest strain rate. Specimens deformed close to this high temperature and slow strain rate regime (MgA, MgD, MgE, MgG, MgH and MgI) exhibit large elongation exceeding 200%, meaning that they shows superplatic deformation behavior. While at low temperature and fast strain rate, elongation of 84% was obtained for specimen MgC.

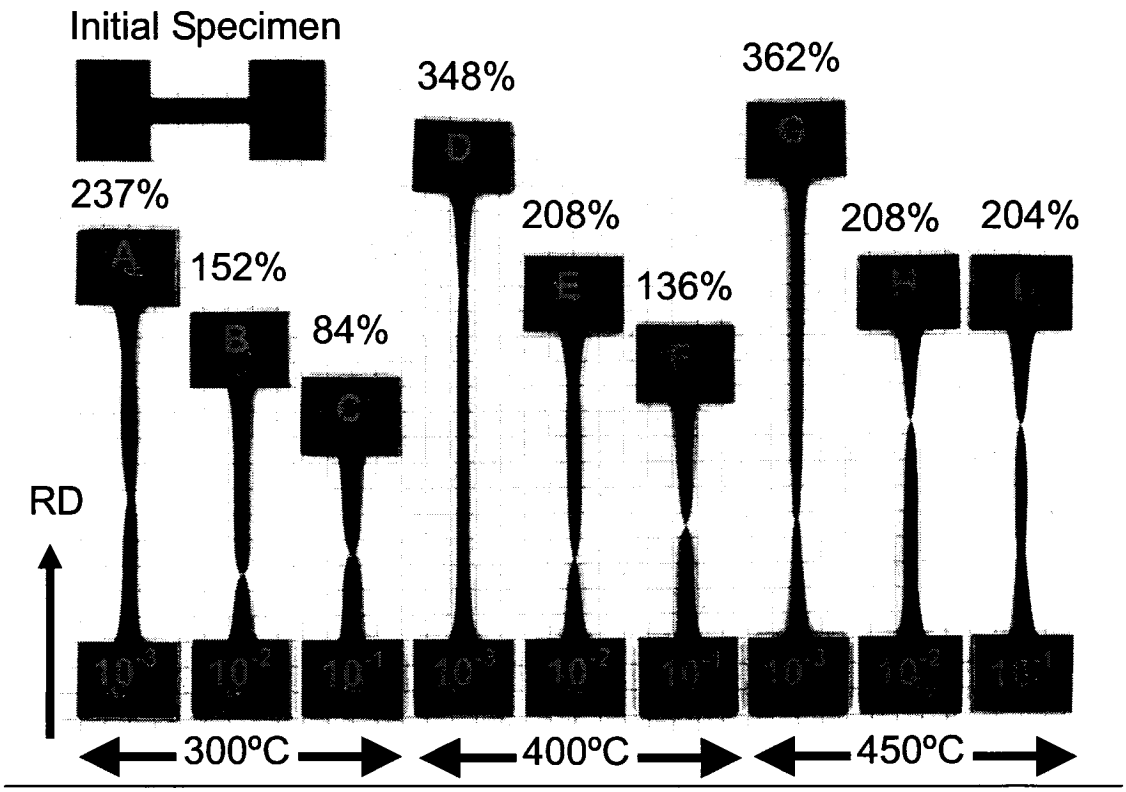

Figure 5 - 4. Fracture specimens by tensile test at various conditions.

5.4 Microscopic examination of fracture behavior

The microstructure examination was conducted on all specimens pulled to failure at/near tip gage region as shown in Figure 5-5.

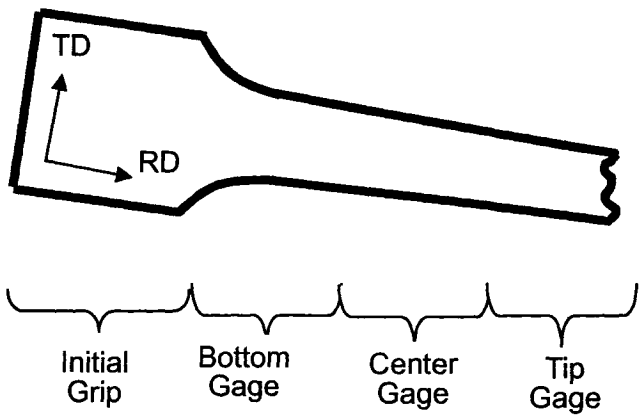

Figure 5 - 5. A schematic image of half portion of a specimen pulled to failure by tensile test. RD: Rolling/Tensile Direction; TD: Transverse Direction.

Based on the macrostructure and microstructure examination of all specimens pulled to failure, the specimens failed in one of three manners under elevated temperature deformation: (1) by 'moderate' necking with some degree of deformation/necking at the tip (Figures 5-6a and 5-6b); (2) by cavity formation and subsequent interlinkage of these cavities, exhibiting a very abrupt fracture surface with minimal necking, (Figures 5-6c and 5-6d); or (3) by 'strong' necking down almost to a point (Figures 5-6e and 5-6f).

The fractured tensile specimens were examined under light optical microscope and the results are summarized in Figure 5-7 in the form of a fracture map. Failure was characterized by strong necking at high strain rates ($0.01s^{-1}$ and $0.1s^{-1}$) and at high temperatures (400°C and 450°C); cavity interlinkage was observed at high temperatures (400°C and 450°C) with lower strain rate ($0.001s^{-1}$), and moderate necking took place at lower temperatures (300°C) irrespective of the strain rate. There were two specimens that exhibited a mixture of failure modes, the conditions were: (1) 400°C and $0.01s^{-1}$, where some sign of cavity interlinkage was seen along with necking; and (2) 300°C and $0.1s^{-1}$,

where necking was observed to be stronger than moderate necking, but less pronounced than in the specimens with strong necking.

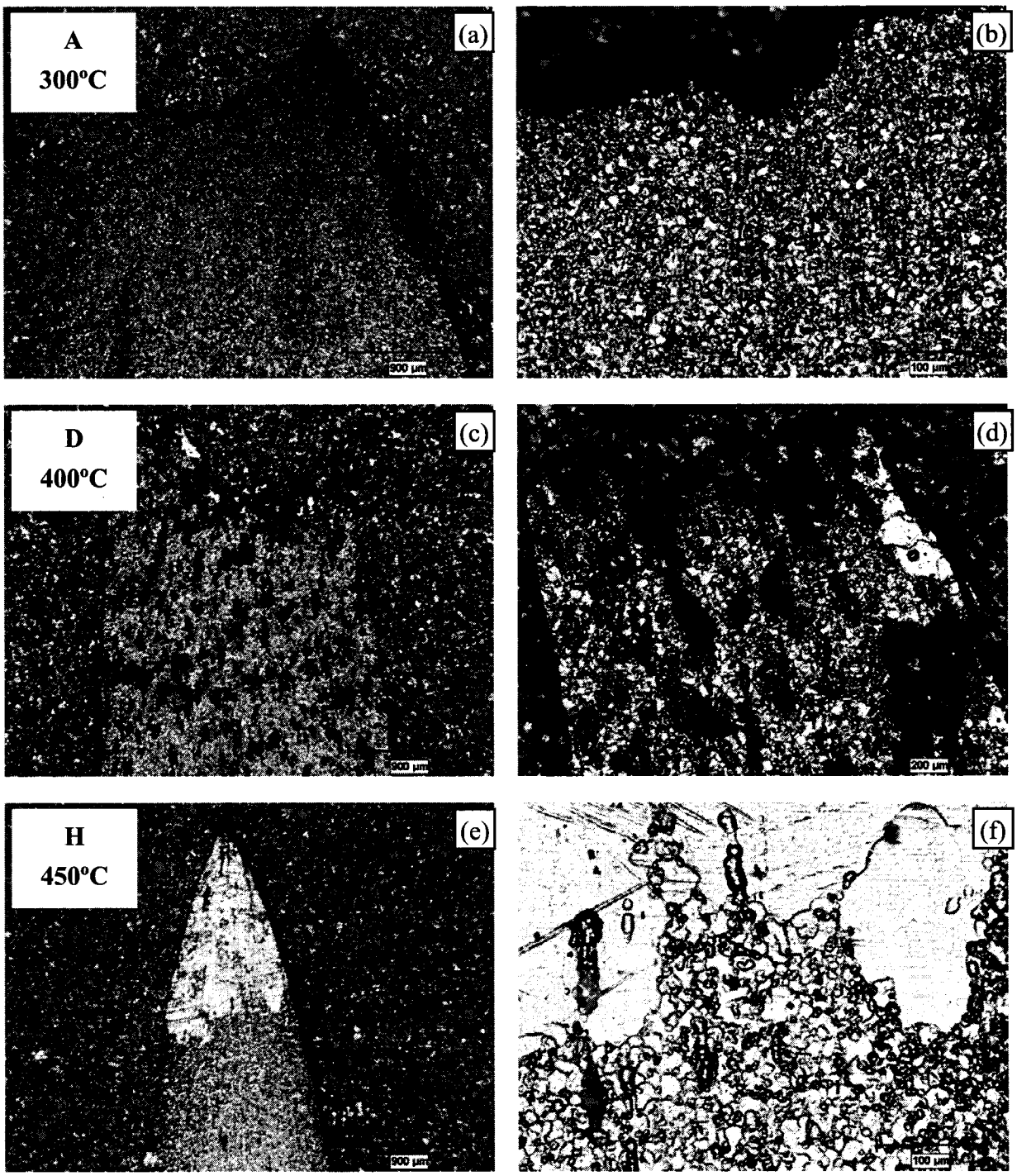

Figure 5 - 6. Low and high magnification micrographs of the cross-section of fractured tip failed by: moderate necking (a) and (b); cavity interlinkage (c) and (d); strong necking (e) and (f).

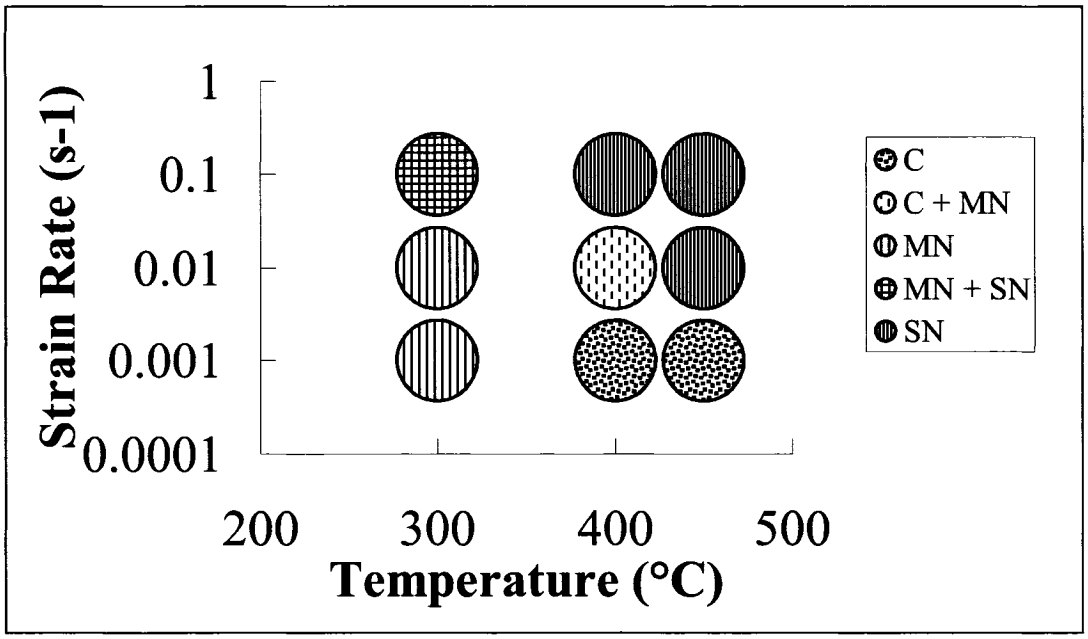

Figure 5 - 7. Mode of failures map as a function of strain rate and temperature for the commercial AZ31 sheet. Notation: MN as moderate necking failure, C as cavity interlinkage failure, SN as strong necking failure, C+MN as moderate necking failure with some trace of cavity, and MN+SN as necking degree in between of MN and SN.

In the specimens where cavitation controlled failure was recorded, very little necking was observed at the fracture tip. Large cavities, about 20-50 μm, were present across the entire fracture surface, especially near the fracture tip (Figure 5-6d). In the specimens that failed by strong necking, significant grain growth was seen near the fracture tip. Figure 5-6f illustrates the grain growth in the necked region for specimen deformed at 450°C and $0.01s^{-1}$. In the region near the fracture tip, the grain size was approximately 50-100 μm, while away from the fracture tip, the grain size was only 20μm. A similar change in grain size was not observed in the samples that failed by cavity interlinkage.

5.5 Microtexture Examination of Fracture Behavior

Microtexture Examination of the specimens was performed with the aid of Orientation Imaging Microscope (OIM). It enables us to perform the boundary and crystallographic orientation examination by analyzing the Electron BackScattered Pattern (EBSP) of the specimens. It is then possible to characterize the fracture tip in depth and try to understand the deformation mechanisms of AZ31 sheet at elevated temperature. All examination focus on the tip gage of selected specimens pulled to failure (Figure 5-5). The examined specimens are shown in Table 5-3.

Table 5 - 3. Deformation conditions and modes of failure of the examined specimens under OIM.

Specimen	***Temperature (°C)***	***Strain Rate (s^{-1})***	***Failure Mode***
MgB	300	10^{-2}	Moderate Necking
MgD	400	10^{-3}	Cavity Interlinkage
MgH	450	10^{-2}	Strong Necking

5.5.1 High Temperature Deformation Characteristic of AZ31 Sheet

Figure 5-8 shows typical Electron Backscattered Diffraction (EBSD) maps of the one area from the sample deformed at 300°C with strain rate of $0.01s^{-1}$. In Figure 5-8a, it can be seen that grains possess a large fraction of high angle grain boundaries (>15°). For this particular specimen, dual grain size was observed: some fine grains of less than 10μm and some coarse grains of more than 10μm.

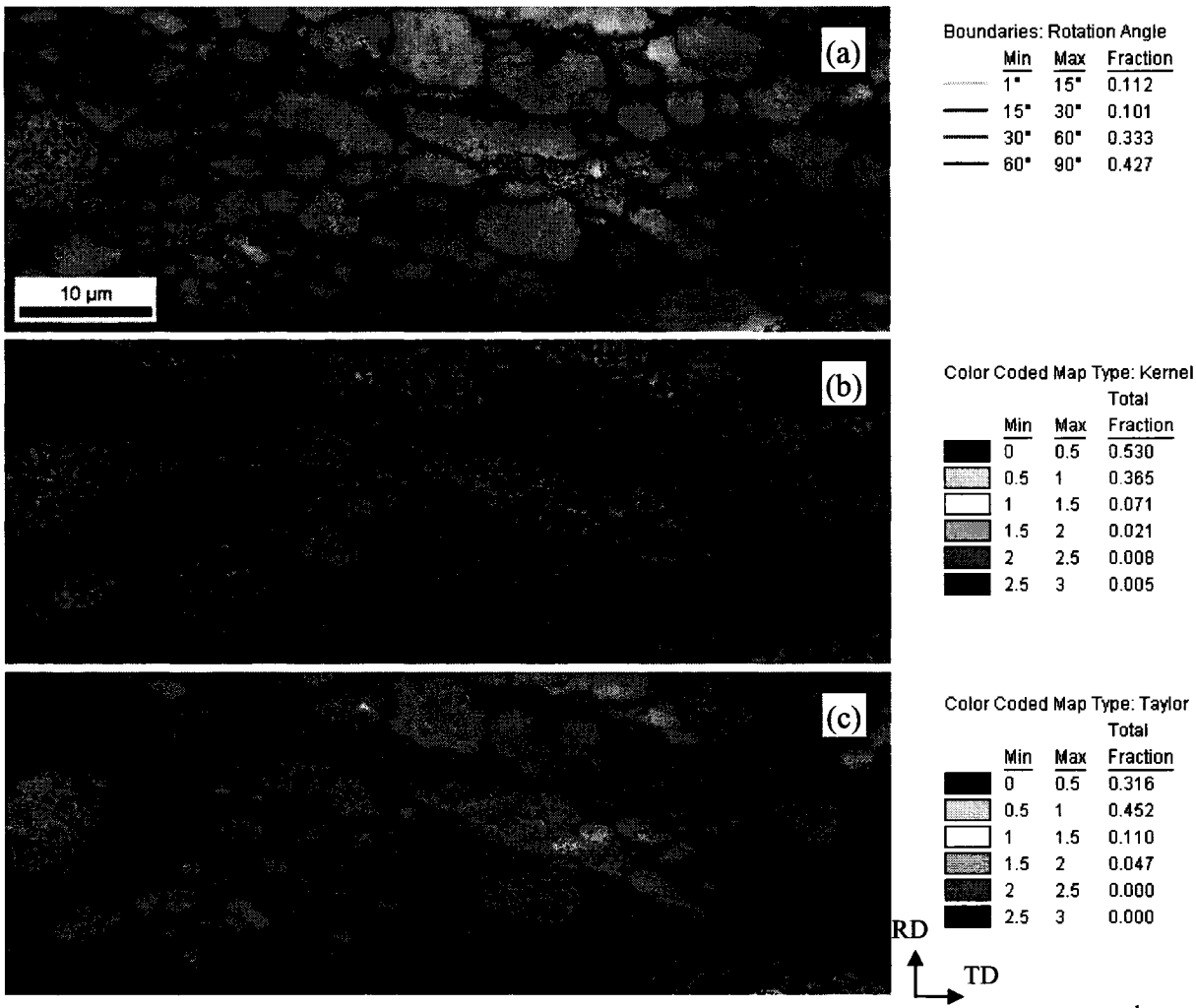

Figure 5 - 8. EBSD mapping of sample deformed at 300°C with strain rate of $0.01s^{-1}$ (MgB): (a) grain boundary characteristic distribution map; (b) kernel average misorientation map; (c) Taylor factor map. RD: Rolling/Tensile Direction; TD: Transverse Direction.

Figure 5-8b shows the Kernel mapping, which is a representation of local misorientation. It is a tool in OIM analysis that can be used as a representation of dislocation density. Figure 5-9 is a schematic illustration of Kernel average misorientation calculated of a selected scan area. The misorientation of the neighbors points relatively to the yellow point are measured. Only misorientation less than 5 degree is considred as local misorientation, as indicated in the equation below the figure, in this exemplary case, the

kernel value is 1.9. As a general rule, if the kernel average misorientation value is high and distributed all over the scan image, it means that the dislocation density is high as well. In the present sample, the degree of local misorientation was found to be almost the same within the scan area. Although there was a slight difference of 0.5 in the degree of local misorientation, this difference was considered negligible. This might suggest that the deformation was relatively homogeneous.

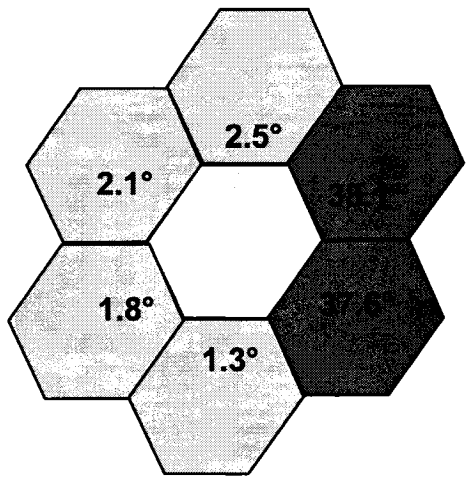

$$Kernel\ Average\ Misorientation = 1.9° = \frac{(1.3° + 1.8° + 2.1° + 2.5°)}{4}$$

Figure 5 - 9. A schematic illustration of Kernel average misorientation calculation of a selected scan area [2].

The Taylor factor in OIM can be used as an indication of strain incompatibility. In the case of specimen deformed at high temperature, homogeneous deformation is encouraged. As a result, the Taylor factor mapping seen in Figure 5-8c shows no sharp differences in Taylor factor across grain boundaries. This observation means that there is no significant local stress concentration. It can be explained by the increase in the number of operating slip systems, which gives rise to homogeneous deformation that is more typical for 'Taylor type' plasticity.

The OIM mappings in Figure 5-10 show the microstructure represented by Image Quality (IQ) and crystallographic map by Inverse Pole Figure (IPF) of the deformed specimens at various conditions. It is believed that as temperature increases texture might change during deformation due to activation of additional slip systems, such as prismatic (non-basal <a>) slip and pyramidal (<c+a>). For all deformation conditions, basal texture in AZ31 alloy was retained as indicated in Figures 5-10b, 5-10d and 5-10f, where (0001) basal crystallographic plane is represented by red. The initial texture of the rolled sheet was basal as reported in Figure 5-2b. This can be explained by referring to the CRSS's of the Mg crystal shown in Figure 2-8. Despite the dramatic drop of CRSS for prismatic and pyramidal slips at temperature above 250°C, these CRSS are still much higher compare to basal one.

Figure 5-11 represents the grain size distribution of the specimens obtained from OIM. At elevated deformation temperatures such as 400°C and 450°C, coarser grains resulted during dynamic recrystallization (DRX). Figures 5-10c and 5-10d show the coarser DRX grains as a result of the higher deformation temperatures (400°C and 450°C). Since the d_{rex} grain size is directly proportional to Zener-Holloman parameter (Z), for a given strain rate, higher temperature deformation results in larger d_{rex} grain size.

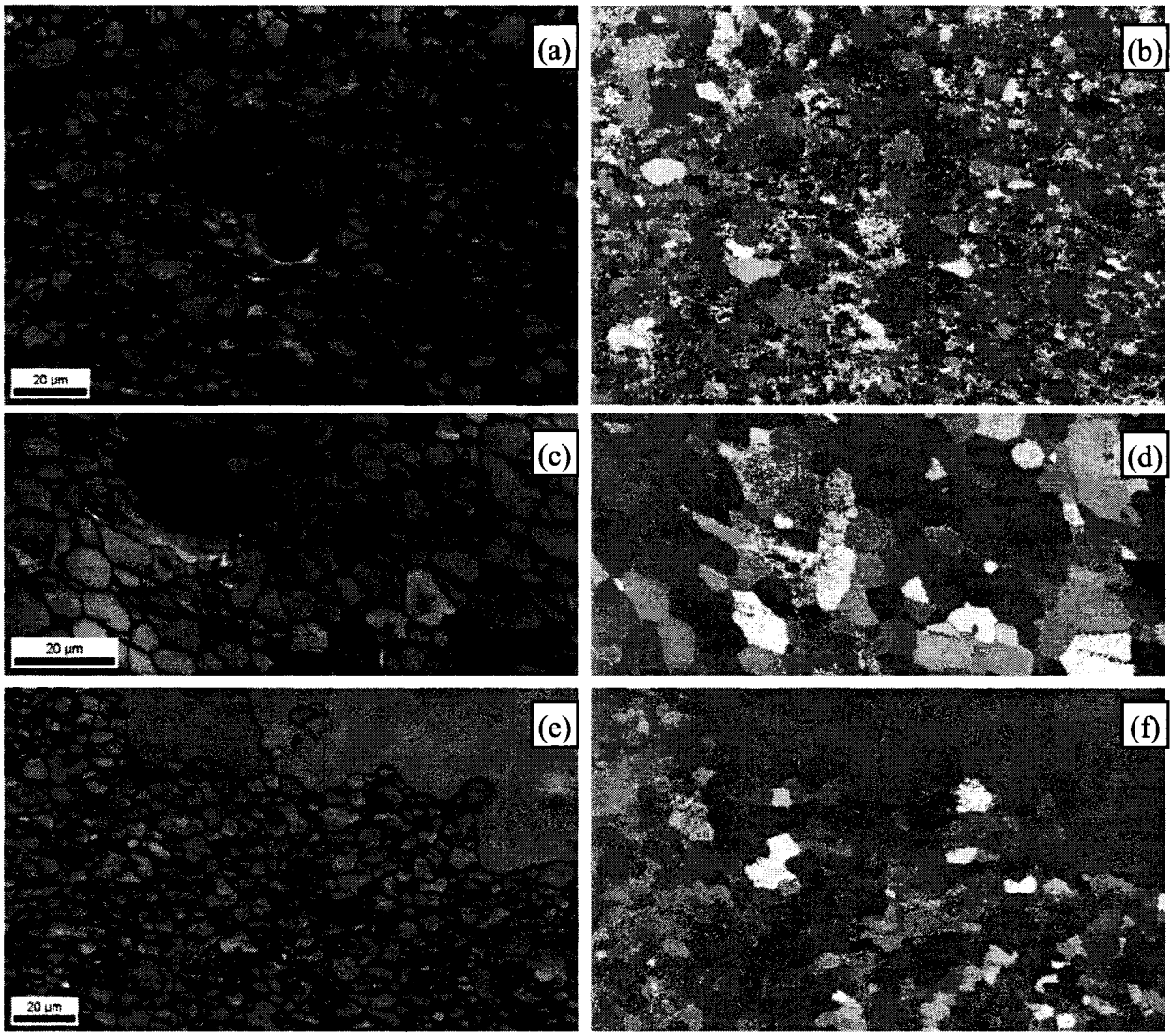

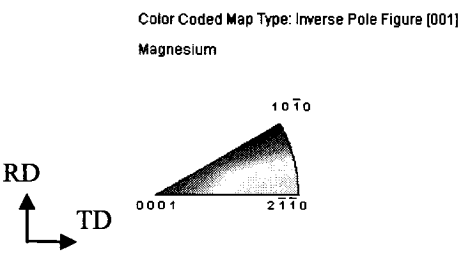

Figure 5 - 10. OIM mapping corresponding to sample deformed at: (a) and (b) 300°C at $1x10^{-2}$ s^{-1} (MgB); (c) and (d) 400°C at $1x10^{-3}$ s^{-1} (MgD); (e) and (f) 450°C at $1x10^{-2}$ s^{-1} (MgH). RD: Rolling/Tensile Direction; TD: Transverse Direction.

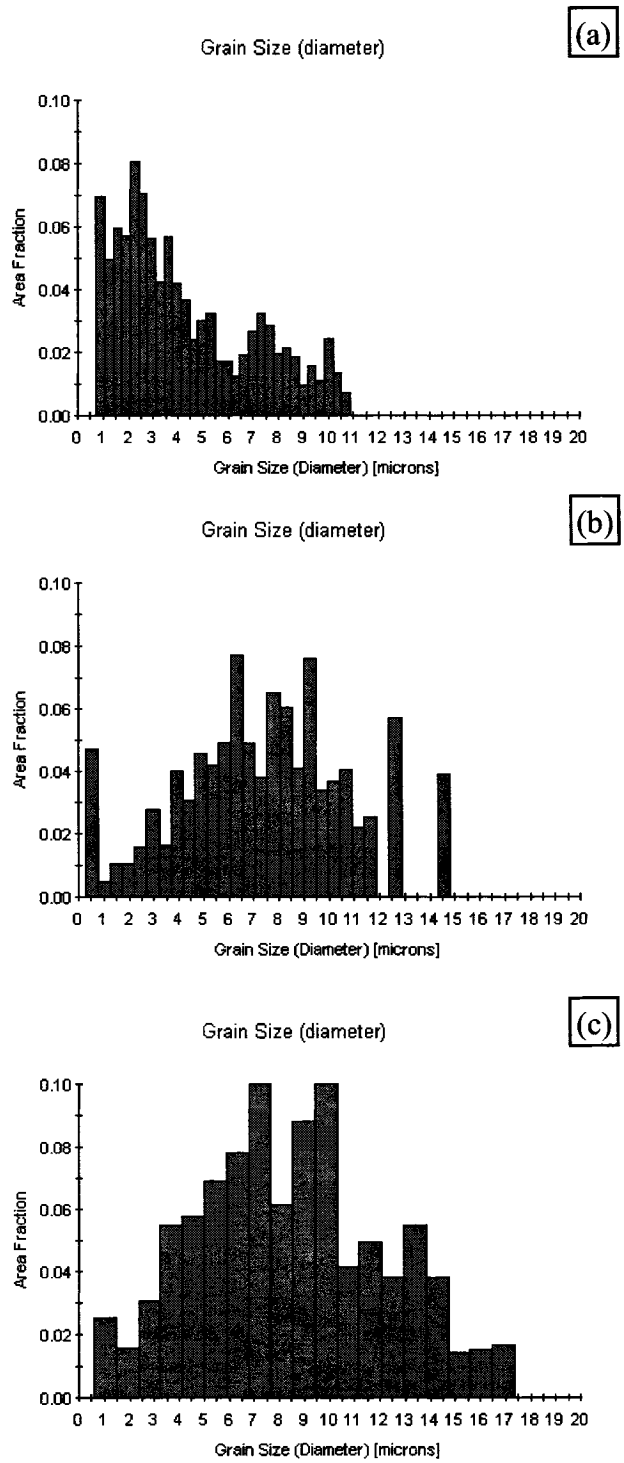

Figure 5 - 11. Grain size distribution of specimens deformed at: (a) 300°C at $1x10^{-2}$ s^{-1} (MgB); (b) 400°C at $1x10^{-3}$ s^{-1} (MgD); (c) 450°C at $1x10^{-2}$ s^{-1} (MgH).[5]

[5] The area measured for grain size calculation is similar for all specimens. Due to grain size difference, it affects the number of grains measured and the bar weight.

5.5.2 Failure Mechanism of AZ31 Sheet at Elevated Temperatures

At high temperatures, one of the important mechanisms of plastic deformation in polycrystals that attributes to superplasticity can be grain boundary sliding (GBS). It consists of the random rotation of grains along their grain boundaries and often leads to decrease in texture intensity. This is observed in the case of superplastic deformation of Al alloys.

In the present study, the strong basal texture in AZ31 alloy was still maintained as shown in Figure 5-10. Pole figures calculated based from EBSD results of the same deformed specimens discussed in Figure 5-10 show, however, slight differences in the basal texture shape under different deformation conditions (Figure 5-12). As the temperature increased, the texture become more concentrated and distributed in a like six-fold symmetric patterns of the $\{1\bar{1}00\}$ and $\{11\bar{2}0\}$ pole figures shown in Figures 5-12b and 5-12c. Since there are six equivalent $\{1\bar{1}00\}$ and $\{11\bar{2}0\}$ planes in HCP crystal, this might indicate that slip activities occurred during deformation. In particular, the non-basal <a> slip modes can give rise to this sort of texture evolution. In addition, the split of basal plane might be a sign of <c+a> slip activation at higher temperatures to accommodate the deformation mechanism [3].

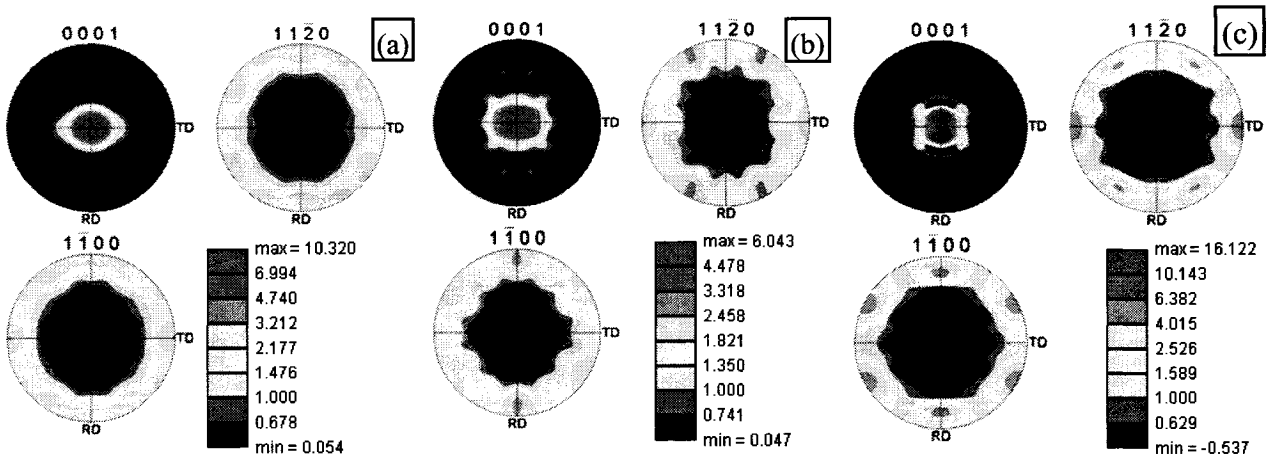

Figure 5 - 12. Pole figures corresponding to sample deformed at: (a) 300°C at $1x10^{-2}$ s^{-1} (MgB); (b) 400°C at $1x10^{-3}$ s^{-1} (MgD); (c) 450°C at $1x10^{-2}$ s^{-1} (MgH). RD and TD represent the rolling direction (tensile direction) and transverse direction of the samples.

If one would associate the failure modes discussed preciously with deformation mechanisms, it could be distinguished by two simplified models illustrated in Figures 5-13 and 5-14.

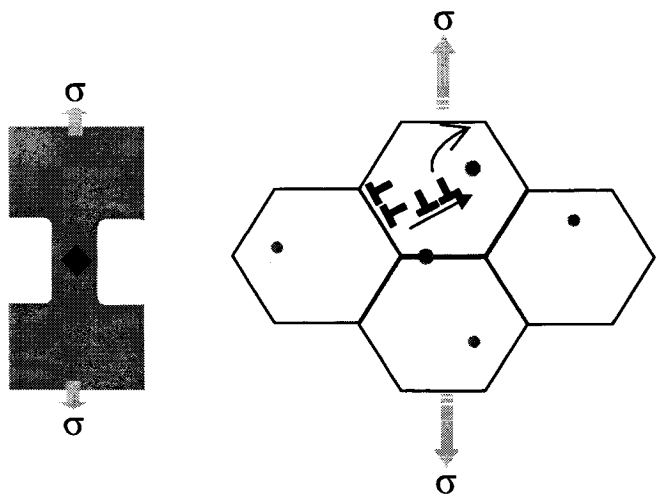

Figure 5 - 13. Model for the strong necking failure mode: (a) un-deformed tensile specimen; (b) generation of dislocations that could slide and/ or climb with increasing strain.

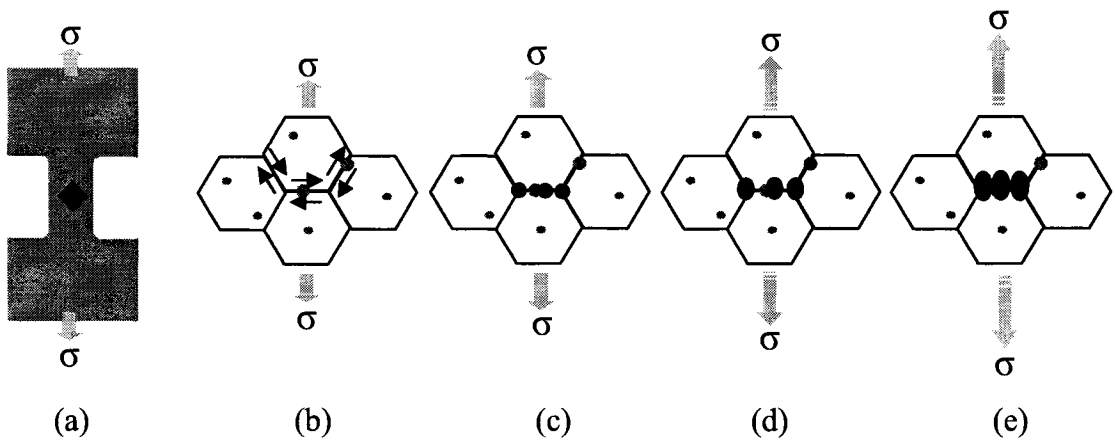

Figure 5 - 14. Model for the cavity interlinkage failure mode: (a) un-deformed tensile specimen; (b) sliding and rotation of fine recrystallized grains; (c) micro- cavities formed near grain boundaries, triple points and precipitates; (d) growth of cavities with strain and (e) the coalescence and interconnection of cavities after a 'substantial' amount of strain is accumulated, lastly material fails without significant macroscopic necking or excessive thinning.[6]

Failure by strong necking, as in the case of of MgH (Figures 5-6e and 5-6f), is a result of slip mechanism or dislocation creep mechanism [5]. Coarser recrystallized grains formed during deformation at elevated temperatures and faster strain rate results dislocations that are prone to slip and/or climb. As a result the material exhibits significant localized thinning and reduction in area prior to failure, and no sign of grain boundaries sliding mechanism (e.g cavities) seems to be apparent. The strong necking failure mode model controlled by dislocation creep is shown in Figure 5-13.

On the other hand, due to the presence of cavities distributed uniformly on the cross-section of fractured tip, as shown in Figure 5-6c and 5-6d, one could assume that GBS also made some contribution to deformation. Consequently, the whole deformation

[6] An adaptation of the model from D.L. Lin [4]

process and failure mechanism behind the cavity interlinkage failure mode is believed to start with sliding and rotation of fine recrystallized grains that nucleate microcavities near the grain boundaries, triple points and precipitates; and these microcavities then experience growth and coalescence during the deformation which in turn result materials discontinuity and final failure. Figure 5-14 illustrates the model for the cavity interlinkage fracture mechanism. However this cavity interlinkage failure model is considered to be controlled mainly by grain boundaries sliding deformation mechanism. Since basal texture is still maintained, it is assumed that other possible deformation mechanisms, such dislocation creep, might associated with GBS.

At this point of the study, it is understood that combination of deformation mechanisms such DRX, slips, GBS and dislocation creep contributed to overall ductility of the specimens during deformation at high temperature. Figure 5-15 shows the deformation mechanism of AZ31 at elevated temperature. The model illustrates that both GBS and dislocation creep are the deformation mechanisms seen in most of the specimens pulled to failure, especially for specimens that yielded 'superplastic' elongation (>200%). In order to clarify this issue, if one can examine the flow curves and perform the flow mechanism in interrupted tensile tests at different strains then the contribution of individual deformation mechanism at elevated temperature can be ascertained.

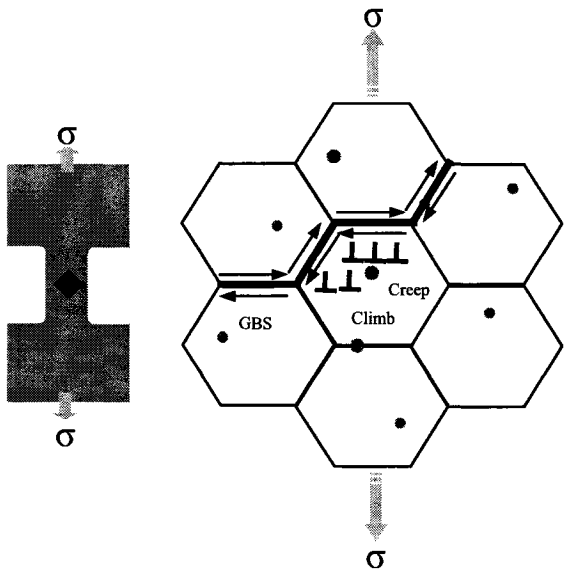

Figure 5 - 15. Model for deformation mechanism of AZ31 at elevated temperature: both GBS and dislocation creep are the deformation mechanism [6].

5.5.3 Abnormal Grain Growth

One interesting deformation characteristic of AZ31 sheet at high temperature is the occurrence of abnormal grain growth at certain conditions. The most important characteristic of abnormal grain growth is that, along with the inhibition of the growth of most of the grains, there are certain grains which grow fast. The abnormal grain growth phenomenon was found only when the sample failed by strong necking. It seemed to occur when the sample reached certain level of critical strain in a very short period of time. In this case, it is at the tip (Figure 5-6e), where the stored energy is the highest. Figure 5-16 shows the grain boundary characteristic distribution map of abnormal grain growth in sample deformed at 450°C at faster strain rate of $1x10^{-2}$ s^{-1}.

Figure 5 - 16. Grain boundary characteristic distribution map of abnormal grain growth. Specimen MgH.

The driving force for abnormal grain growth is usually the reduction in energy of the grain boundaries of certain grains (i.e. surface energy driving force). The energy of the free surface depends on the number of atoms per unit area of the surface and is the lowest for the most densely packed lattice plane, which is (0001) for Mg. Thus, abnormal grains revealed the (0001) basal plane as shown in Figure 5-10f. Moreover, it has been well established that grain boundary mobility strongly depends on the grain boundary character and the misorientation angle. High angle boundaries (>15°) are more mobile than low angle boundaries (<15°). As a result, abnormal grain growth must be related to the contribution of boundaries with high mobility (Figure 5-16).

5.6 Summary

Different failure modes (moderate necking, cavity, strong necking) were observed in the investigated specimens pulled to failure.

Unlike to Al alloy, AZ31 alloy still maintained its basal texture during deformation. However, slight differences in the basal texture shape were observed with different deformation conditions. The gradual concentration of the six-fold symmetric patterns in the $\{1\bar{1}00\}$ and $\{11\bar{2}0\}$ pole figures and the splitting of basal plane distribution found in deformation at higher temperatures (400 and 450°C) indicate that slip mechanism or dislocation creep deformation mechanism contribute to the deformation. Additional of grain boundary sliding (GBS) deformation mechanism is believed to contribute the 'superplastic' elongation (>200%) of some specimens deformed in tension. In brief, in slow strain rate ($\leq 1x10^{-3}$ s^{-1}) and high temperature ($\geq$ 400°C) deformation condition, the deformation mechanism is controlled by GBS and dislocation creep, while at fast strain rate ($\geq 1x10^{-2}$ s^{-1}) and high temperature ($\geq$400°C), it is rather controlled by dislocation creep.

Abnormal grain growth occurred in the sample deformed at elevated temperature and at fast strain rate.

5.7 References

1. ASTM E2448-06
2. EDAX TSL OIM Analysis manual, 2004
3. Li, H-L, Formability of Magnesium Alloys, *McGill/GM Internal Report*, 4th quarterly, 2005.
4. Yin, D.L., et al., "Superplasticity and cavitation in AZ31 Mg alloy at elevated temperatures", *Materials Letters*, v59, 2005, pp.1714–1718
5. Krajewski, P., "Elevated Temperature Forming of Sheet Magnesium Alloys," SAE Paper No. 2001-01-3104, Warrendale, PA, SAE, 2001.
6. Wei, Y. H. et al., "Superplasticity and cavitation in AZ31 Mg alloy at elevated temperatures", *Materials Science and Engineering*, A360, 2003, pp. 107-115

Chapter 6

Microstructure Control for Optimizing the Formability of AZ31 Sheet

6.1 Introduction

Several methods have been developed for refining grain in Mg alloys and they can be divided into the following groups: (i) cold or warm rolling plus heat treatment involving recrystallization, (ii) hot extrusion at high extruded ratio, (iii) hot working on Mg alloy powder, (iv) severe plastic deformation process such as torsion straining and equal channel angular extrusion (ECAE). Among these methods, the rolling is the only method that can be manipulated to fabricate large sheet or plates for application in transportation sector industry

In order to obtain a good formability of a sheet or plate the microstructure and texture

derived from the rolling process is important. This chapter will describe forward series of thermomechnical processes that were used for controlling microstructure, more specifically the grain size in commercial AZ31 sheet. These thermomechanical treatments will be used to optimize the microstructure and to improve the deformation behavior at elevated temperature. Sheets of AZ31 alloy with different grain sizes will be produced using different cold rolling reductions and annealing conditions. Deformation behavior of these different materials will be studied using tensile testing over a range of temperatures and strain rates. In addition, these studies will allow us to understand the correlation between the deformation mechanisms and failure modes.

6.2 Grain Size Control by Thermomechanical Processing

A commercial AZ31 sheet, 2.01 mm thick, supplied by Magnesium Electron (MEL), was used in the present study. Table 6-1 shows the chemical composition of the material. Figure 6-1 is a micrograph of the material in the as-received condition, which shows a heavily deformed microstructure consisting of twins and deformation bands.

Table 6 - 1. Chemical composition of the commercial AZ31 sheet supplied by MEL.

Element	wt%
Al	3.1
Zn	1.0
Mn	0.42
Fe	0.006
Cu	0.003
Ni	< 0.003
Si	< 0.1
Ca	< 0.01
Be	< 0.005
Sr	< 0.005
Ce	< 0.01
Mg	Balance

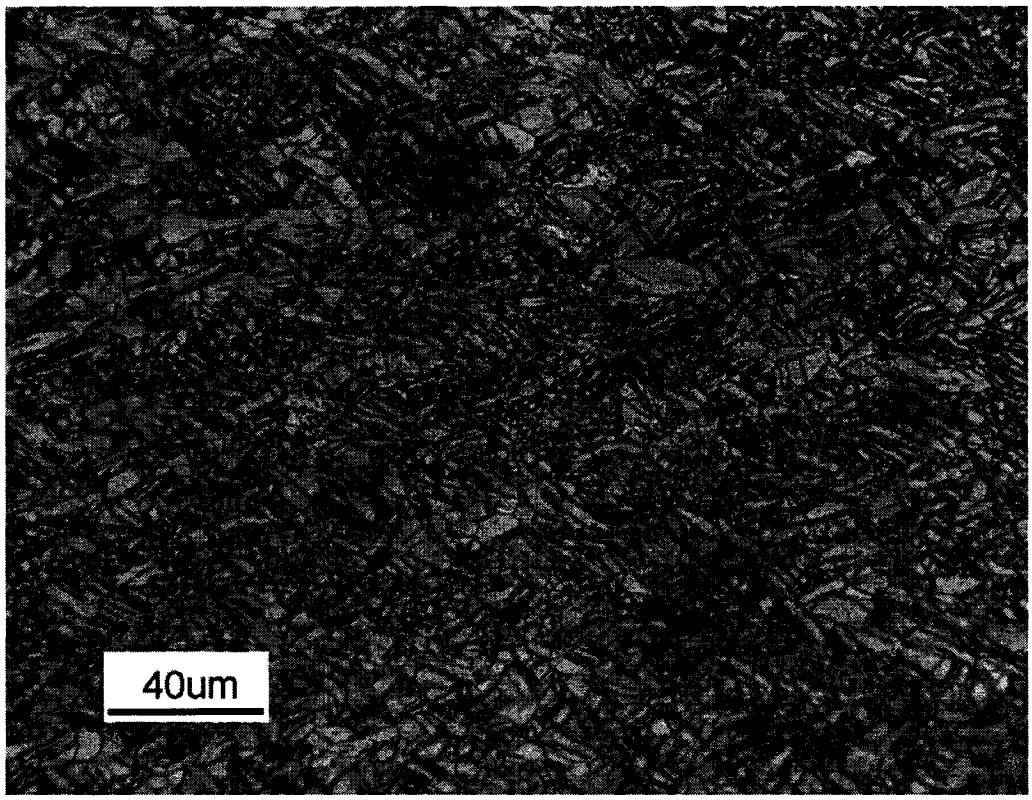

Figure 6 - 1. Microstructure of AZ31 Mg sheet as-received condition (as hot-rolled sheet).

Samples cut from the sheet were heat treated at different temperatures (350, 400 and 450°C) for different time periods (1, 10 and 30 min) to establish an optimum recrystallization treatment. Rockwell hardness measurements (HRF)[7] were made on the heat treated samples to evaluate if the recrystallization is completed. Based on the results, a heat treatment of 350°C for 15 min was selected as the optimum recrystallization treatment for this material. This treatment fully recrystallizes the deformed structure of the sheet, and gives an equiaxed 8 μm grain size.

[7] The Rockwell HRF hardness measurements were made using F scale with Tungsten (W) indenter. HRF values are averages of 5 separate indents.

Thermomechanical processing was used to generate different grain size materials from the as-received AZ31 sheet. The procedure used is schematically shown in Figure 6-2. Several 90 mm x 230 mm pieces cut from the commercial AZ31 sheet were given the already established recrystallization treatment of 350°C for 15 min, to produce fully annealed samples. The annealed samples were then cold rolled in a laboratory rolling mill (220 mm roll diameter) with reductions ranging from 0.5 to 14.5%[8] in a single pass. This was followed once again by the recrystallization treatment to produce sheet materials with different grain sizes. Three materials with distinctly different grain sizes, 8 μm (G8), 20 μm (G20) and 50 μm (G50), were selected to investigate the effect of grain-size on the tensile behavior at different temperatures.

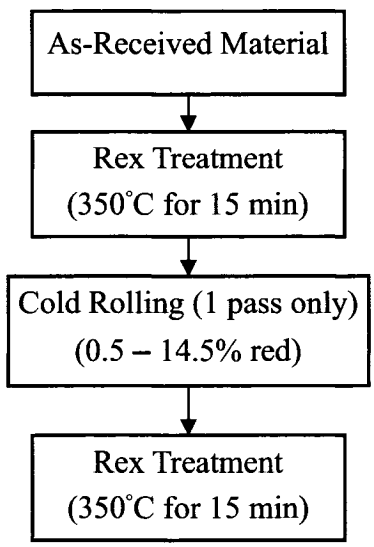

Figure 6 - 2. Procedure for generating AZ31 materials with different grain sizes.

Tensile test specimens, as shown in Figure 5-3, were machined according to ASTM E2448-06 standard from the selected sheet materials G8, G20 and G50. The machining

[8] 14.5% was the maximum cold rolling reduction that could be imparted before cracking occurred.

was done with the tensile axis aligned parallel to the sheet rolling direction. Elevated temperature tests were conducted in a screw-driven Instron 5568 machine equipped with an air circulating furnace and Bluehill data acquisition software. The specimens were heated to the test temperature in about 10 min before pulling to failure, and then water quenched. The tests were conducted at 350, 400 and 450°C and strain rates of $1x10^{-3}$, $1x10^{-2}$ and $1x10^{-1}$ s^{-1} under constant strain rate condition, i.e. under exponentially increasing cross-head velocity. Tensile elongation was obtained by dividing gage extension at failure by the original gage length of the specimen.

Strain-rate-change (SRC) tests were performed under the condition of 350, 400, 450 and 500°C in order to determine the effect of strain rate and temperature on deformation of the specimens. Figure 6-3 illustrates the strain rate path of the strain-rate-change test used in this present study (routine 1). The initial strain rate used in this test was $3x10^{-3}$ s^{-1} to a strain of 0.06. This initial strain rate allows us to work in the steady-state region. The first strain rate starts with $3x10^{-2}$ s^{-1} to 0.14 strain and subsequently, the strain rate and the amount of strain are decreased in successive steps until a strain of about 0.30 in this cycle is reached. This routine is repeated again in the second and third cycle. In addition, a separated strain-rate-change test (routine 2) at very slow strain rates ($3x10^{-5}$ and $1x10^{-5}$ s^{-1}) was conducted to understand further magnesium behavior at this range of strain rates (Figure 6-4). The calculation of strain rate sensitivity is taken from the values obtained in the first two cycles to avoid onset of instability (i.e. necking).

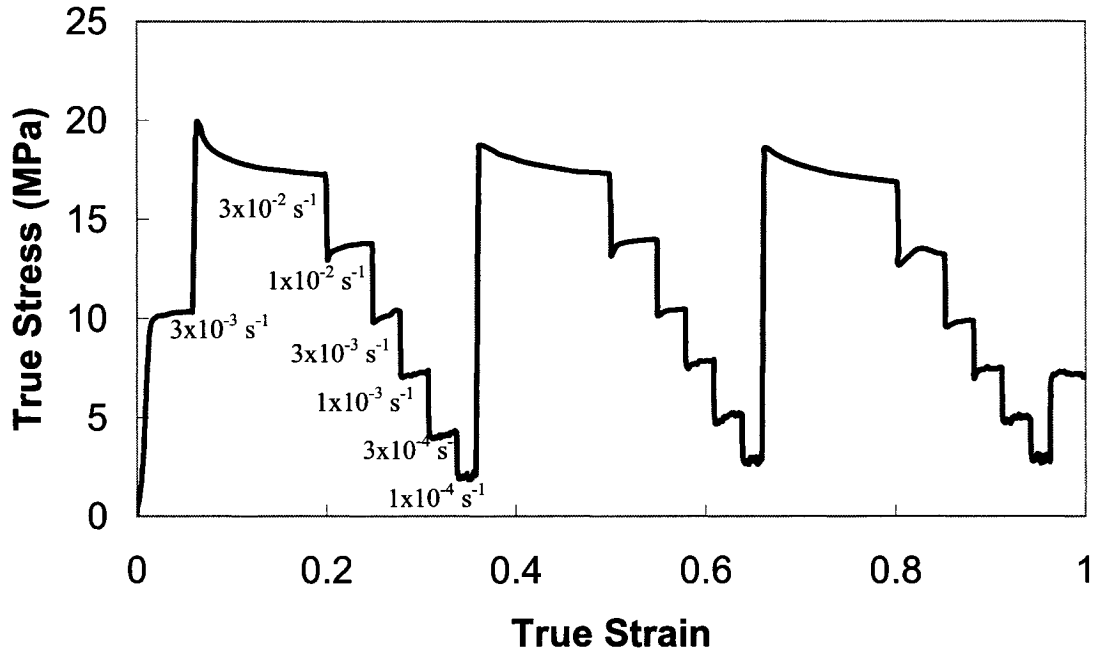

Figure 6 - 3.The strain rate path of the strain-rate-change test for routine 1. Specimen G8 tested under 500°C.

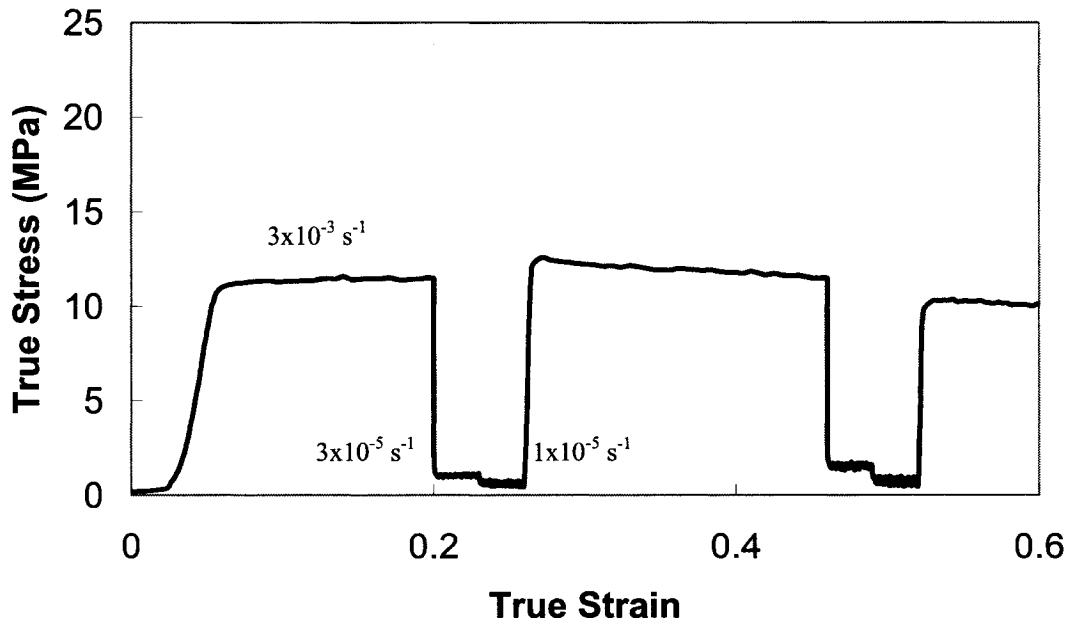

Figure 6 - 4. The strain rate path of the strain-rate-change test for routine 2. Specimen G8 tested under 500°C.

6.3 Effect of Grain Size on Deformation Behavior of AZ31 Sheet at Elevated Temperatures

6.3.1 Optimzing the Heat Treatment

Change in sheet hardness with annealing time at the three temperatures (350, 400 and 450°C) is shown in Figure 6-5a. Annealing at any of the three temperatures results in sharp drop in sheet hardness from 76 HRF in the as-received (hot rolled) condition, to below 65 HRF after 1 minute at given temperature. The hardness drop beyond 1 minute is practically negligible. The sharp hardness drop with little change after further annealing is an indication of full recrystallization of the material to a defect free state. It is concluded that the AZ31 sheet can be fully recrystallized within 1 minute at 350-450°C. The small differences in the sheet hardness values for different annealing temperatures in Figure 6-5a are a consequence of the slightly different grain sizes after annealing at different temperatures, as shown in Figures 6-5b - d. The recrystallized grain size changes little with increasing annealing time at 350°C, but shows a grain growth at 450°C, increasing from 10 μm after 10 minutes to 12.5 μm after 30 minutes annealing. Thus grain growth is a concern at 450°C. Based on the conducted tests, a heat treatment of 350°C/15 minute was chosen for recrystallization of the AZ31 material in this study. Annealing at 350°C provided the finest and stable grain size, and 15 minute was a sufficiently long time to attain full recrystallization at that temperature.

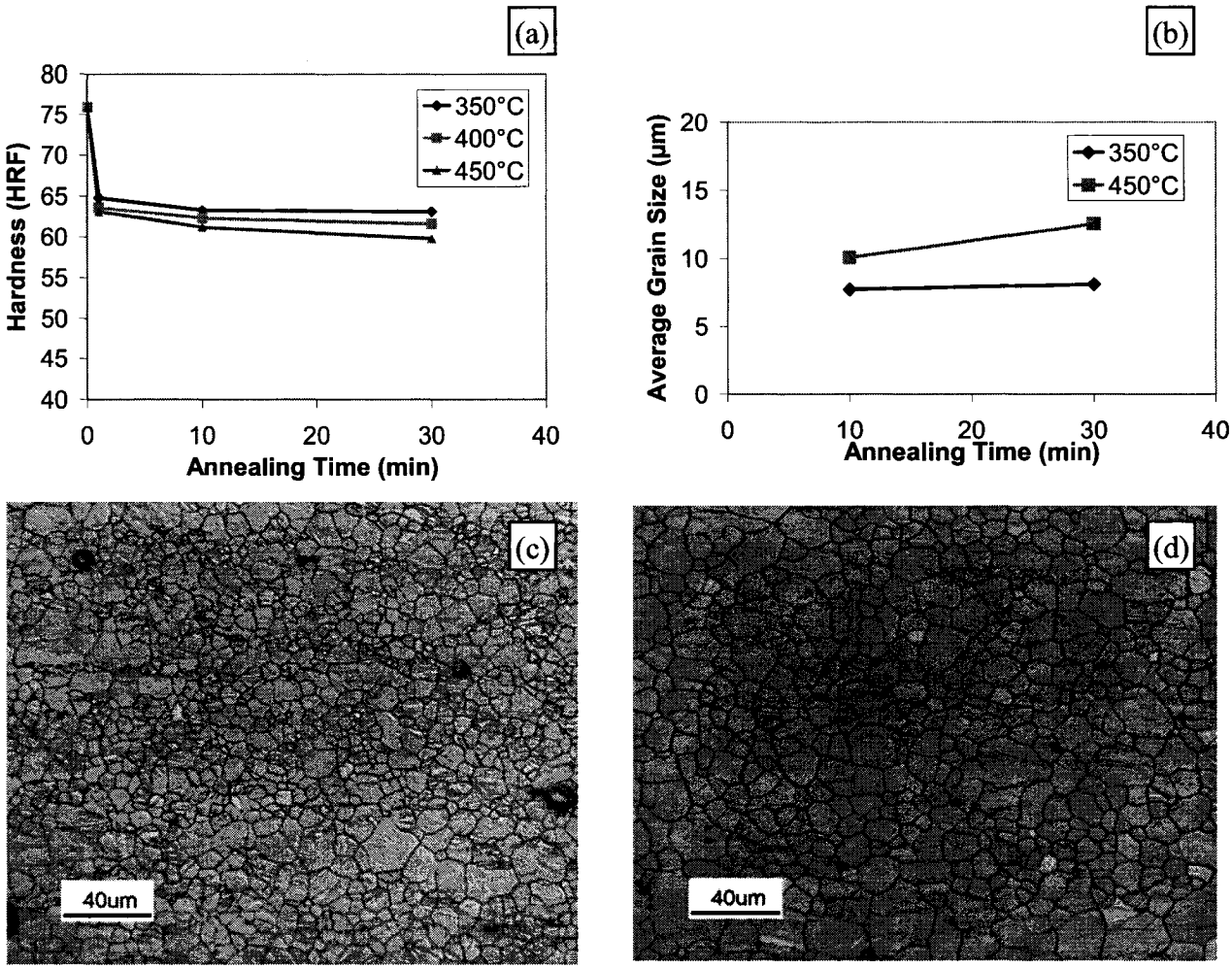

Figure 6 - 5. AZ31 specimens annealed at different temperatures and times in a furnace: (a) Hardness (HRF) plot; (b) average grain sizes plot; (c) microstructure of the specimen heat treated at 350°C for 10 min (d_{ave} = 8 µm); and (d) microstructure of the specimen heat treated at 450°C for 10 min (d_{ave} = 10 µm).

6.3.2 Generating Different Grain size

A schematic of the thermomechanical process used to generate different grain size materials from the as-received AZ31 sheet is shown in Figure 6-2. Pieces cut from the AZ31 sheet were heat treated at 350°C for 15 minutes, cold rolled with different reductions ranging from 0.5 – 14.5% in a single pass, and again heat treated at 350°C for 15 minutes. Figure 6-6 shows change in sheet hardness with rolling reduction both after cold rolling (CR) and after the final heat treatment (CR+HT). The CR plot shows typical

strain hardening with increasing cold reduction. The post-heat treatment plot, CR+HT, follows the CR plot up to 0.5% cold reduction, and then shows a sharp drop at 2% cold reduction. Beyond 2% reduction, the hardness increases monotonically with increasing cold reduction. Optical metallographic examination was used to measure grain sizes in the post-heat treatment samples, and the average grain sizes are plotted (GS(CR+HT)) as a function of cold reduction, in Figure 6-6. The plot shows a sharp increase in grain size at 2% reduction, coinciding with the softening in the CR+HT plot. The large grain size (80μm) and the accompanying material softening are consequences of recrystallization of the material. Thus 2% cold work is the threshold strain for strain-induced recrystallization in this alloy. Increasing cold reduction beyond 2% decreases recrystallized grain size, first rapidly to 25μm at 4% reduction, and then more slowly to 8μm at 14.5% reduction. In the CR+HT plot, increase of hardness with increasing cold reduction, beyond 2% reduction, is a consequence of Hall-Patch effect associated with decreasing grain size shown in the GS(CR+HT) plot. Coincidentally, the sheet hardness and grain size at 14.5% reduction closely match with those of the initial, 0% cold rolled sheet.

From the range of grain sizes produced in the preceding, three distinctly different grain sizes, 8 μm (G8), 20 μm (G20) and 50 μm (G50), were selected for further investigation. The G8 was produced by simply heat treating the as-received sheet material at 350°C for 15 minute. The G20 and G50 were produced by first heat treating the as-received sheet at 350°C for 15 min, followed by cold rolling 6% and 3%, respectively, and then heat treating again at 350°C for 15 min. Figure 6-7 shows optical micrographs of the G8, G20 and G50 sheet samples. While G8 and G20 show narrow grain size distributions, G50 shows a bimodal microstructure. Sheet samples produced with 2-3% cold rolling

reduction, in fact show in addition to a bimodal microstructure a gradient in bimodality through the thickness of the sample. Figure 6-8 illustrates the microstructure gradient from surface to center of the G50 specimen. Microstructure near the sheet surface (Figure 6-8a) almost entirely comprises coarse grains, whereas near the center (Figure 6-8b) it comprises approximately 70% by area coarse grains, with average grain size 70 μm, and 30% small grains with average grain size 8 μm, giving an overall average grain size of about 50 μm.

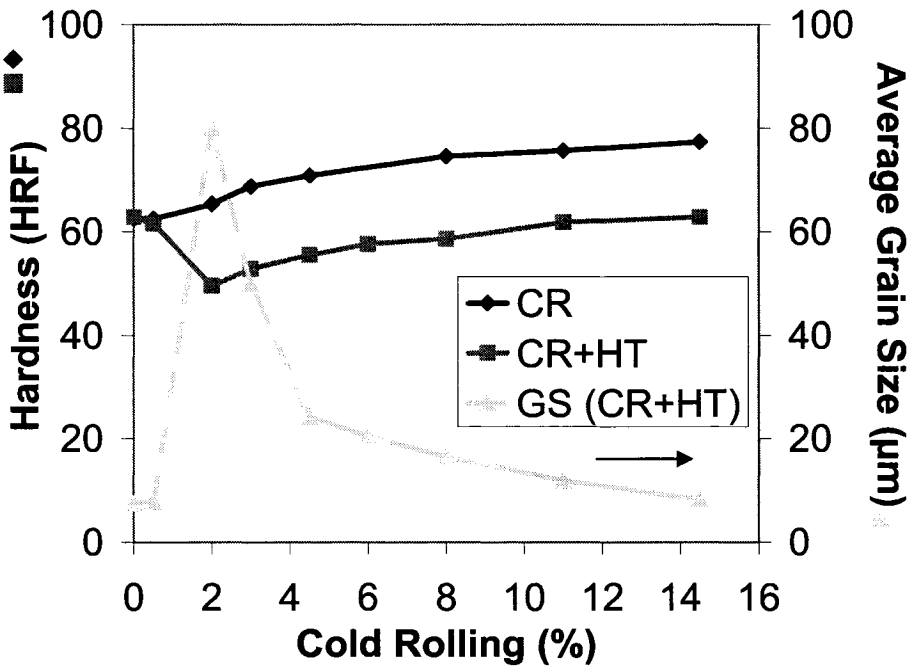

Figure 6 - 6. Correlation between hardness and average grain size as a function of amount of cold rolling reduction. Blue line represents hardness of the cold rolled specimens. Red line represents hardness of the cold rolled followed by annealing specimens. Green line represents average grain size of the cold rolled followed by annealing specimens. The dotted section in the green line indicates a bimodal microstructure was observed.

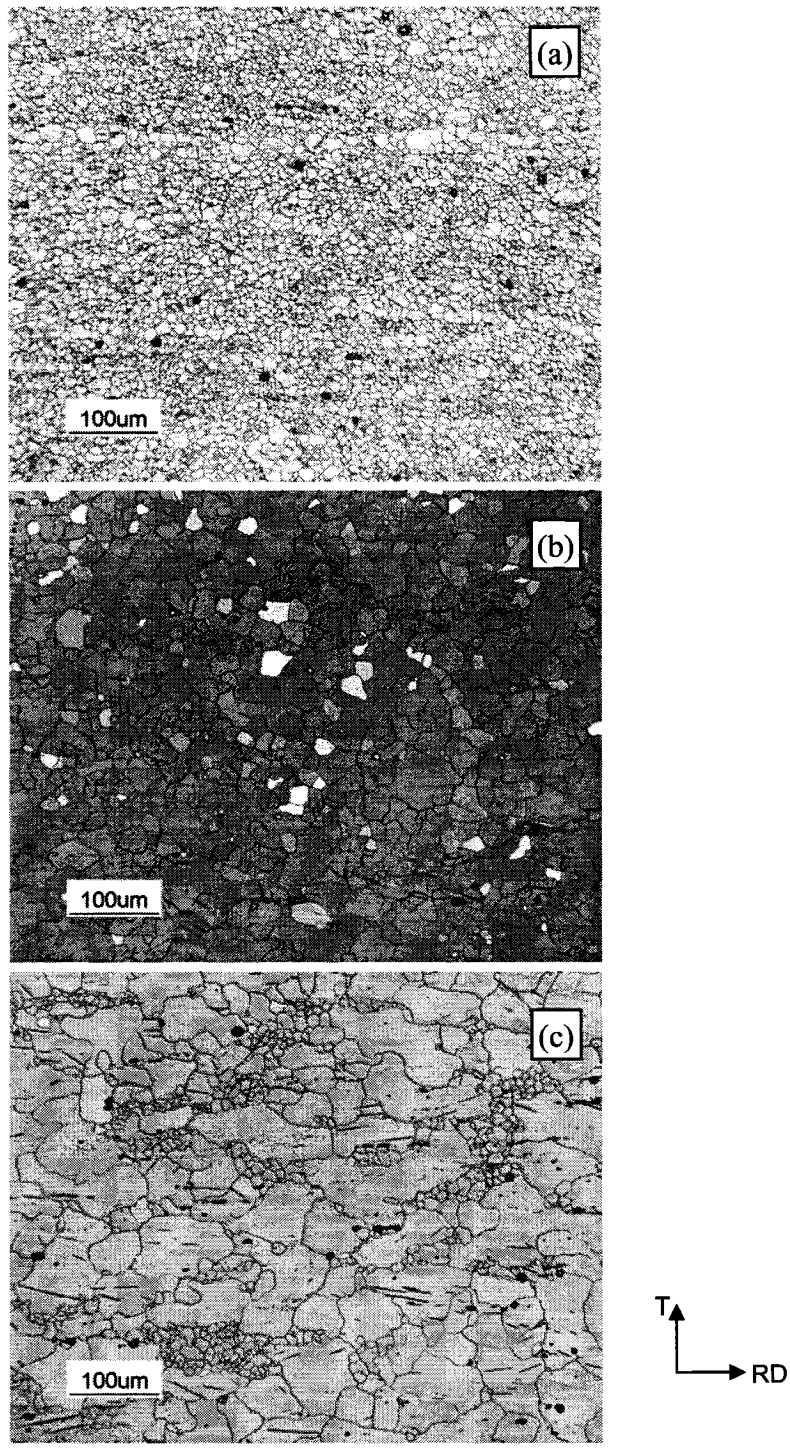

Figure 6 - 7. Different materials produced from as-received AZ31 sheet by different cold rolling and annealing (350°C for 15min) treatment combinations : (a) G8 - average grain size 8 μm, produced by annealing only), (b) G20 – average grain size 20 μm, produced by annealing + 6% cold rolling reduction + annealing (c) G50 - average grain size 50 μm, produced by annealing + 3% cold rolling reduction + annealing. RD: Rolling Direction and T: Thickness Direction.

The microstructure gradient in sample G50 is a consequence of the small cold reduction (3%) used, which barely affects the center of the 2 mm thick sheet. The relatively higher strain near the sheet surface produces nearly complete recrystallization to coarse grains. The sheet centre is barely touched by the small cold reduction, leaving significant areas unrecrystallized and retaining the original 8μm grain size, and the remaining areas comprising the coarse recrystallized grains. As the cold reduction level increases to 4% or greater, the microstructure gradient and bimodality are eliminated and the sheet grain size decreases with increasing density of recrystallization nuclei resulting from increased cold reduction [1].

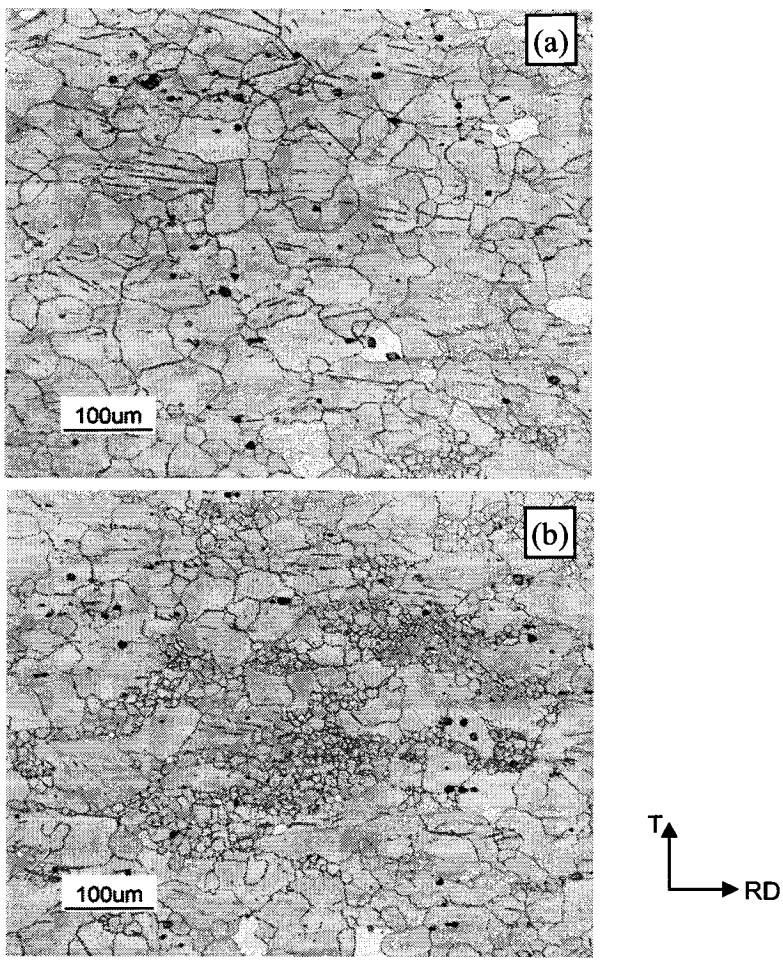

Figure 6 - 8. Microstructures of the sheet specimen subjected to 3% cold rolling reduction followed by annealing at 350°C for 10 min near (a) surface and (b) center. RD: Rolling Direction and T: Thickness Direction.

The commercial AZ31 sheet, produced by hot rolling, has a basal texture in which the (0002) crystallographic planes are predominantly aligned parallel to the sheet rolling plane. It was surmised that processing by cold rolling and annealing may produce a different texture in AZ31. Texture measurements were made on the various cold rolled and annealed sheet samples by an X-ray diffraction method described elsewhere [2]. The method measures texture in terms of a Texture Intensity Factor (TIF), which expresses predominance of a crystallographic plane's alignment with the sheet plane relative to a random sample. All sheet samples showed standard basal texture, though the texture intensity showed a slight, but systematic, increase with increasing cold reduction. (Figure 6-9). However, the texture variations developed in here were not significant enough to affect sheet anisotropy.

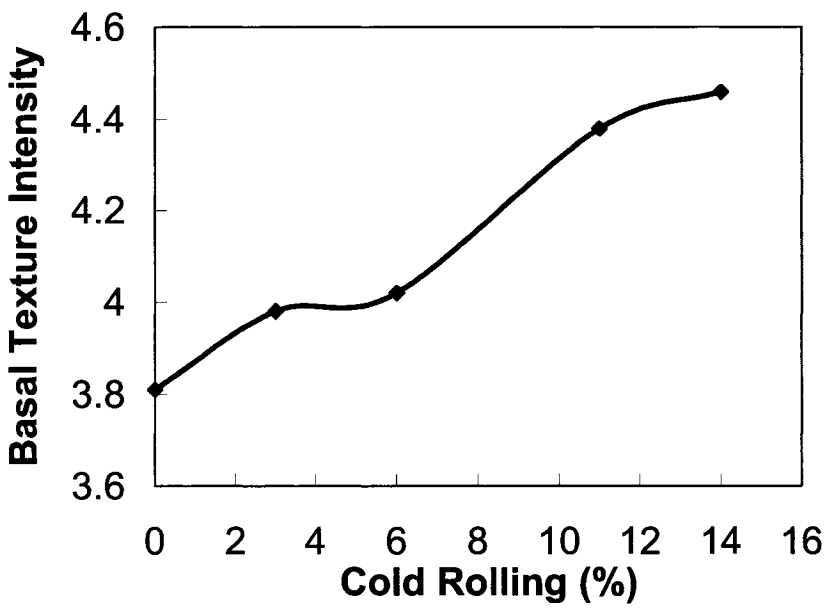

Figure 6 - 9. Intensity of basal plane texture as a function of the cold rolling reduction. All specimens were annealing at 350°C for 10 min after cold rolling prior the texture measurement.

6.3.3 Tensile Behavior at Elevated Temperatures

The true stress-strain curves of the three materials, G8, G20 and G50, for two extreme temperatures 350 and 450°C and two extreme strain rates $1x10^{-3}$ and $1x10^{-1}$ s^{-1} are shown in Figure 6-10. At 350°C and $1x10^{-3}$ s^{-1} (Figure 6-10a), the G8 shows a steady flow behavior and a high failure strain. The G20 and G50 show flow softening, indicative of diffuse necking, and the G50 shows one of the lowest failure strains observed in this study. Some of the highest failure strains are observed at 450°C and $1x10^{-3}$ s^{-1} (Figure 6-10b). The G8 shows gradual hardening followed by a steady flow behavior, suggestive of deformation by grain boundary sliding mechanism in this fine grain alloy. Both G20 and G50 show a sharp spike in stress (indicated by an arrow in Figure 6-10b) in the beginning, which is then followed by a steady flow behavior. All the flow curves for 350°C and $1x10^{-1}$ s^{-1}, in Figure 6-10c, show significant hardening up to a strain of about 0.2, and thereafter rapid softening suggesting strain localization and necking. All three alloys, irrespective of grain size, show some of the lowest failure strains under this low temperature and high strain rate regime. The curves in Figure 6-10d (450°C and $1x10^{-1}$ s^{-1}) show a relatively steady flow behavior and higher failure strains than those in Figure 6-10c. The reason is the high test temperature in Figure 6-10d helps reduce rapid hardening followed by rapid softening observed in Figure 6-10c.

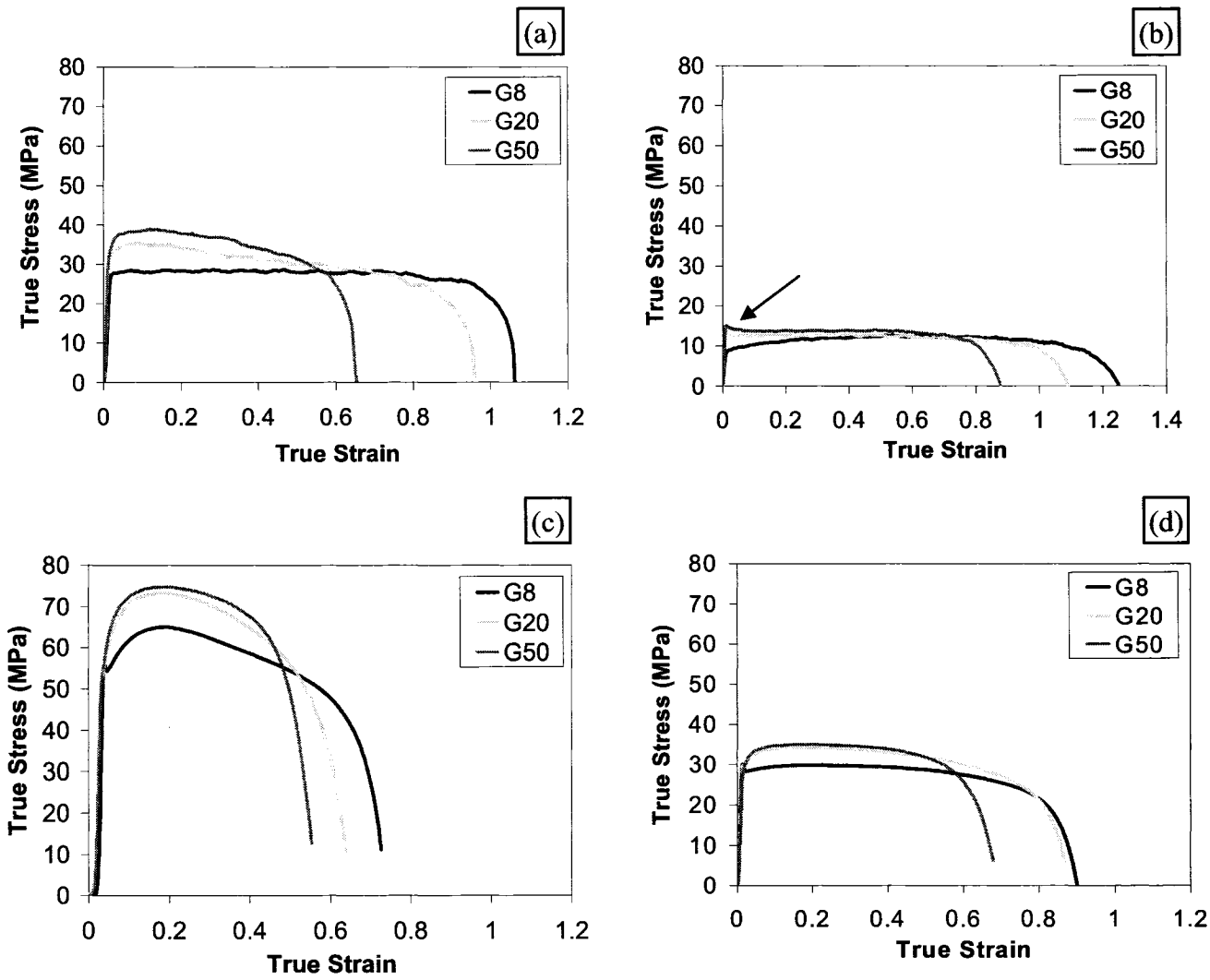

Figure 6 - 10. Stress-Strain curves of specimens at different temperatures and strain rates (a) 350°C and $1x10^{-3}$ s^{-1}, (b) 450°C and $1x10^{-3}$ s^{-1}, (c) 350°C with $1x10^{-1}$ s^{-1} and (d) 450°C and $1x10^{-1}$ s^{-1}.

The dependence of tensile elongation on sheet grain size and test conditions is shown in Figure 6-11. The results show a typical behavior i.e. tensile elongation increasing with decreasing grain size, increasing test temperature and decreasing strain rate. The highest elongation of 265% was observed with the fine-grain G8 material and test condition of 450°C and $1x10^{-3}$ s^{-1}. The specimen with 50 μm grain size, under the same test condition, exhibited an elongation of 152%. The advantage of high elongation with small grain size,

however, was significantly reduced at the highest strain rate of $1x10^{-1}$ s^{-1} (Figure 6-11b).

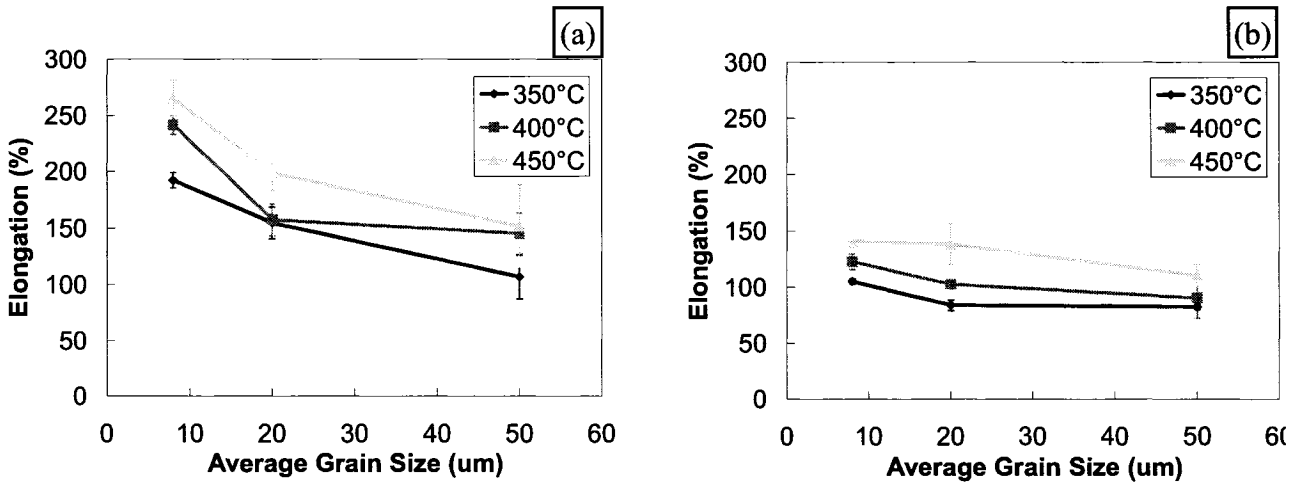

Figure 6 - 11. Variation of tensile elongation as a function of average grain size of material, at different test temperatures and strain rates of (a) $1x10^{-3}$ s^{-1} and (b) $1x10^{-1}$ s^{-1}.

In all three sheet materials, highest tensile elongation was observed under the high temperature (450°C) and low strain rate ($1x10^{-3}$ s^{-1}) condition (Figure 6-11a). The corresponding stress-strain curves, in Figure 6-10b, are characterized by steady flow behavior, though the three curves start out very differently. The curve for the fine grain G8 material shows significant hardening, right up to a strain of about 0.5, before the steady flow begins. This hardening is a consequence of dynamic grain growth typically observed under superplastic deformation conditions [3-4]. Unlike the G8 curve, the G20 and G50 curves in Figure 6-10b start with a peak stress (indicated by an arrow in Figure 6-10b) followed by rapid softening, implying onset of dynamic recrystallization. Similar observation of dynamic recrystallization (DRX) during tensile testing of AZ31 has been reported by Tan et al [5]. The softening lasts till a strain of <0.1, and is followed by a steady flow behavior.

6.3.4 Strain Rate Sensitivity Measurement

The most important mechanical characteristic of a material that can exhibits superplastic behavior is its high strain rate sensitivity of flow stress, referred to as m value. Figure 6-12 shows the stress vs. strain rate curves in double logarithmic scale at different temperatures obtained from the strain rate step tests for specimen G8. The strain-rate sensitivity (m value) was then obtained from the slope of the curves at different temperatures and strain rates. Similar results and calculation were performed on specimens G20 and G50. Figure 6-13 plots the m value as a function of grain size for different temperatures at strain rate of: (a) $1x10^{-4}$ s^{-1}, (b) $1x10^{-3}$ s^{-1} and (c) $1x10^{-2}$ s^{-1}.

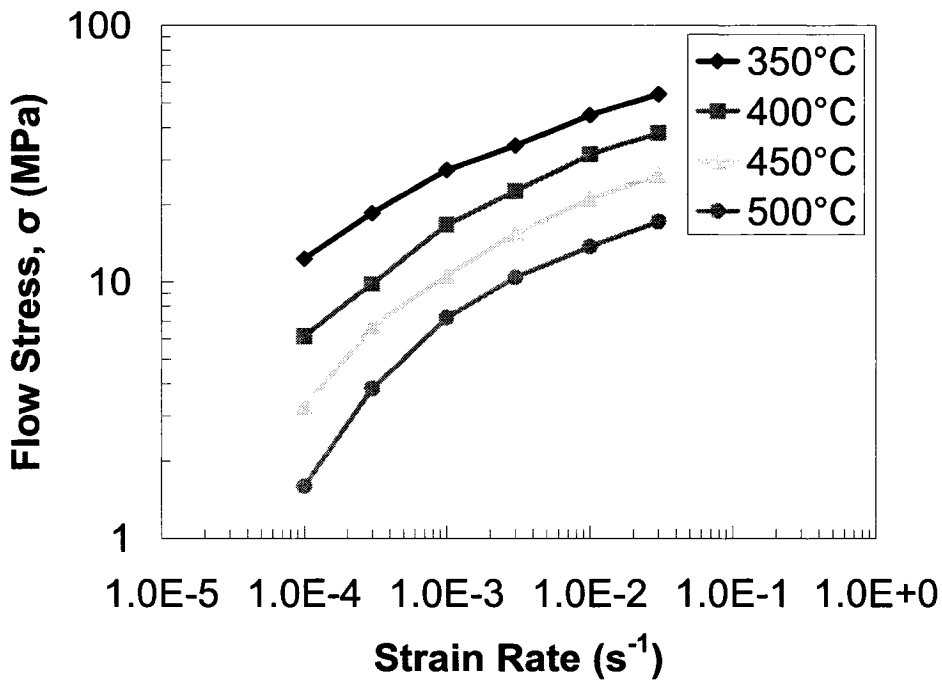

Figure 6 - 12. Stress vs. strain rate curves in double logarithmic scale at different temperatures for specimen G8.

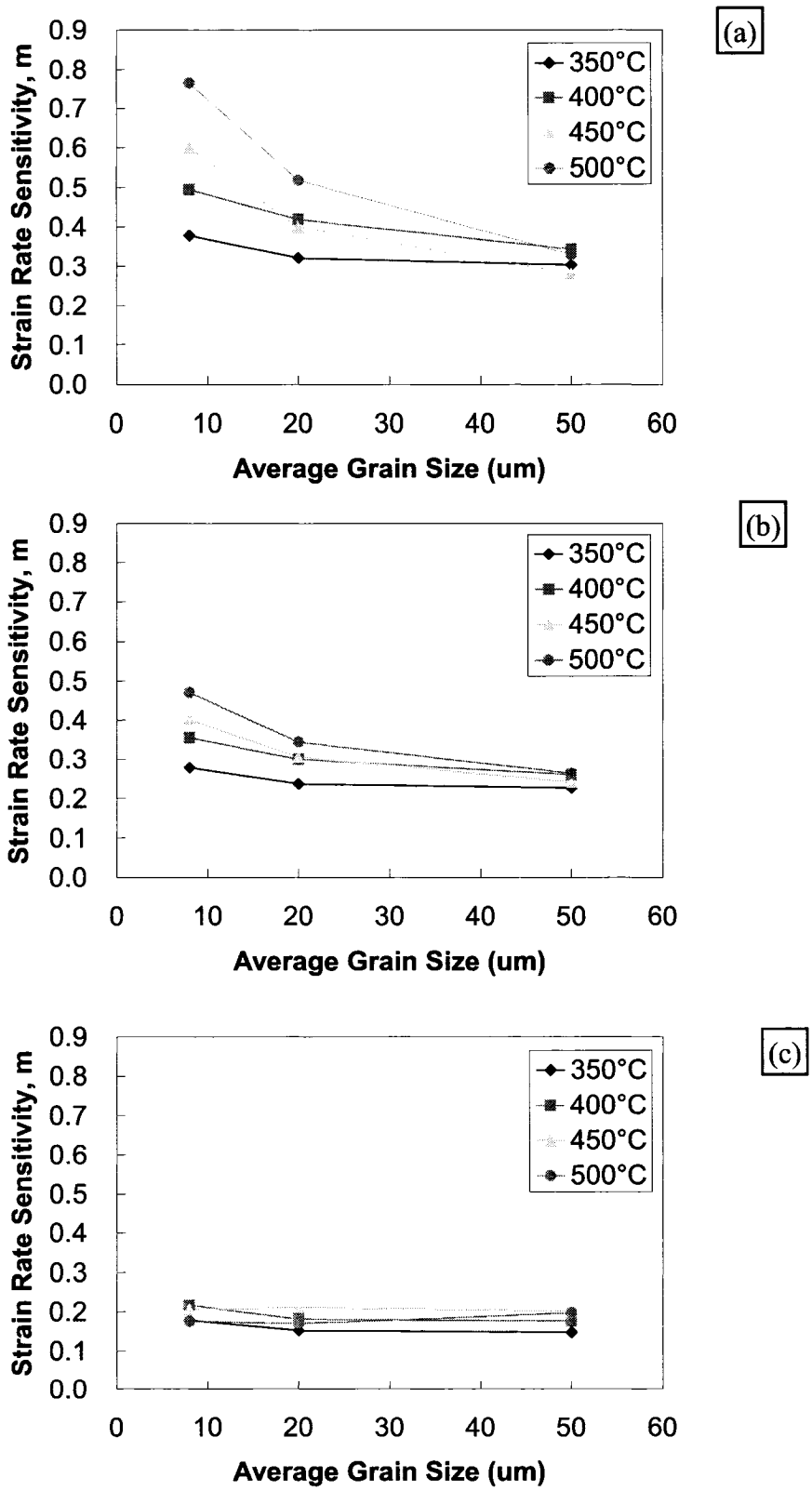

Figure 6 - 13. Variation of strain rate sensitivity as a function of average grain size of material, at different test temperatures and strain rates of a) $1x10^{-4}$ s^{-1}; (b) $1x10^{-3}$ s^{-1} and (c) $1x10^{-2}$ s^{-1}.

In general, the strain-rate sensitivity (m value) of the alloy is very sensitive to both grain size, temperature as well as strain rate (Figure 6-13). For magnesium, the material is denoted superplastic as m value exceeds 0.3. As shown in Figure 6-13a, the three materials exhibit high m values ($m > 3$) for all temperatures with the slowest strain rate ($1x10^{-4}$ s^{-1}). This implies that superplastic behavior could be seen even for specimen with coarse grains at this strain rate. While at fastest strain rate ($1x10^{-2}$ s^{-1}), the m values of all specimens are below the superplastic regime limit (Figure 6-13c). As a common trend, the strain-rate sensitivity increases with decreasing strain rate, increasing temperature and decreasing grain size. The specimen G8 shows the highest m values than specimens G20 and G50 in all conditions, except at fastest strain rate of $1x10^{-2}$, where the m values become "invariant" with grain size and temperature. In addition, the strain-rate sensitivity of the specimen with small size grain is more dependent on deformation conditions (temperature and strain rate) compare to the specimen with large grains. Figure 6-14 illustrates the elongation plot as a function of strain rate sensitivity, which the correlation of increasing elongation with m value is well demonstrated. For instance, the material with a fine grain size of 8 μm is able to exhibit high elongation (>200%), as shown in Figure 6-14, due to its high m value resulted in the low strain rate ($1x10^{-3}$ s^{-1}) and high temperatures (400 and 450°C) regime.

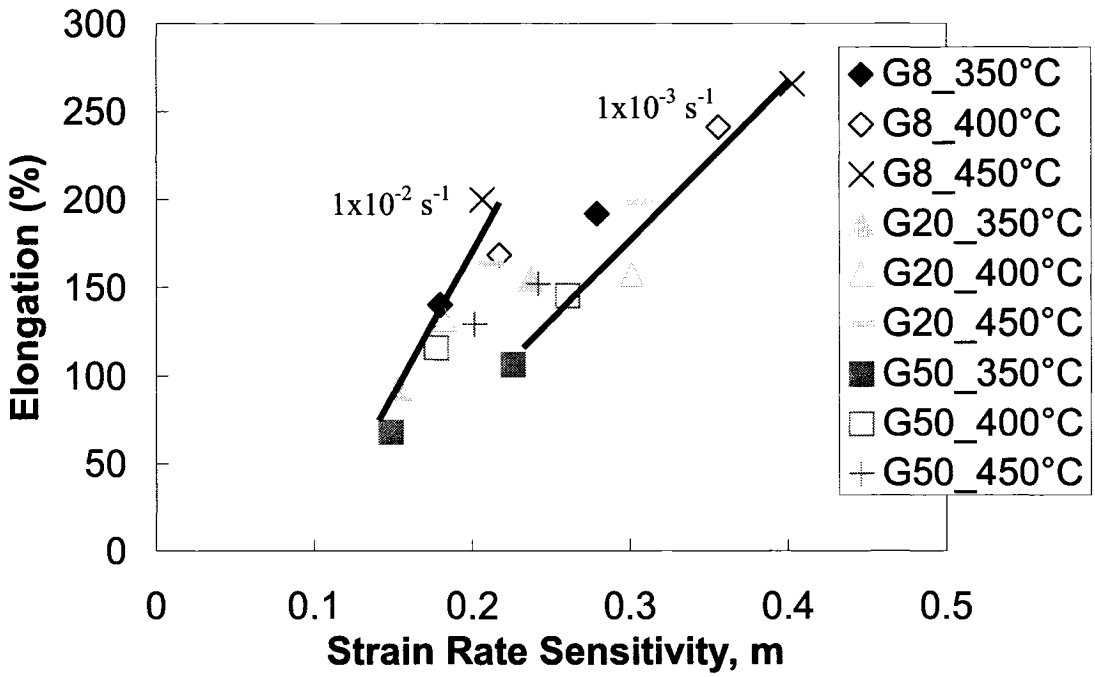

Figure 6 - 14. Elongation plot as a function of strain rate sensitivity of the materials.

In practice most of superplastic materials show a sigmoidal variation of the flow stress with strain rate and that the strain rate sensitivity passes through a maximum [6]. However, this was not seen in the present study because the strain rate range used in the first routine did not cover yet the maximum. Hence, a second SRC routine (routine 2) was conducted for specimens G8 in order to obtain the remaining part of the curve with a very slow strain rates of $3x10^{-5}$ and $1x10^{-5}$ s^{-1} at 500°C. The variation of strain rate sensitivity with strain rate for specimen G8 tested at 500°C of routine 1 and routine 2 is presented in Figure 6-15. As a result, the curve from routine 2 shows a sigmoidal curve, where additional data from $3x10^{-5}$ and $1x10^{-5}$ s^{-1} are included with the previous data obtained from routine 1. These data are fitted using a third degree polynomial. On the other hand, second degree polynomial curve fitting is used to fit the data from routine 1, instead of third. This is for the sake of simplicity because both fittings gave similar results. By

comparing the fitting of the first and second routines, it demonstrates that within the strain rate range of $3x10^{-4}$ and $1x10^{-2}$ s^{-1} the results are comparables either fit data with a second or third degree polynomial. Since strain rates of $3x10^{-5}$ and $1x10^{-5}$ s^{-1} are too slow for industrial practice, only strain rates used in the routine 1 were carried further for investigation.

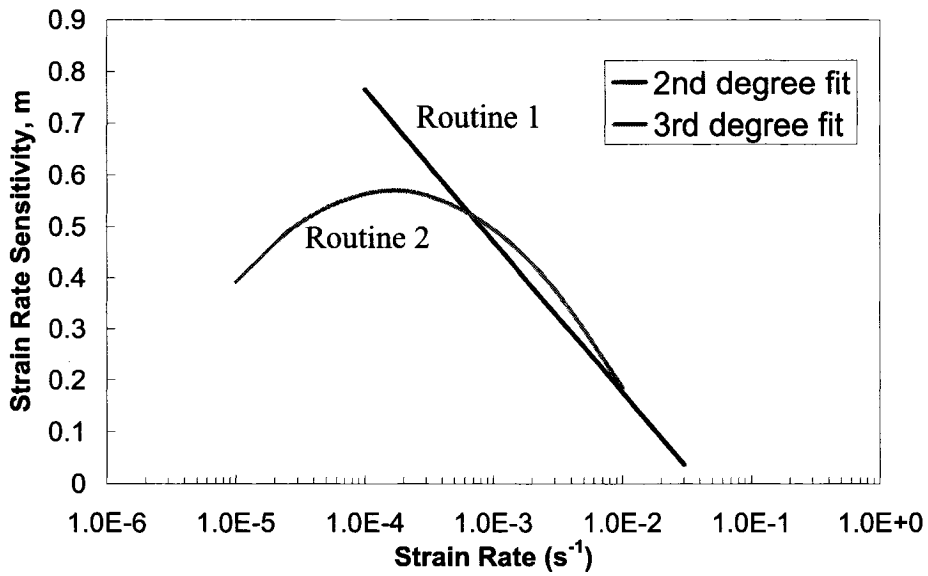

Figure 6 - 15. Variation of strain rate sensitivity with strain rate of routines 1 and 2.

6.3.5 Deformation Behavior at Elevated Temperatures

Stress Exponent

Data from strain-rate-change test on specimens G8, G20 and G50 at temperatures from 350 to 500°C were calculated to determine the deformation behavior of the material at elevated temperature. These data were first plotted as logarithm of true strain rate, $\dot{\varepsilon}$, vs true stress, σ, compensated by the Young's elastic modulus, E. Temperature-dependent elastic modulus values are obtained from the relationship for pure magnesium [7]:

$$E(MPa) = 4.3x10^{4}[1 - 5.3x10^{-4}(T - 300)]$$

Equation 6-1

where T is the absolute temperature in Kelvin. As explained previously, the data from the strain-rate-change tests were measured at early stage of deformation (up to 2nd cycle) to avoid onset of instability. Figure 6-16 illustrates the strain rate vs compensated stress behavior of the G8 at different temperatures. The slope of these curves is equivalent to the stress exponent, n.

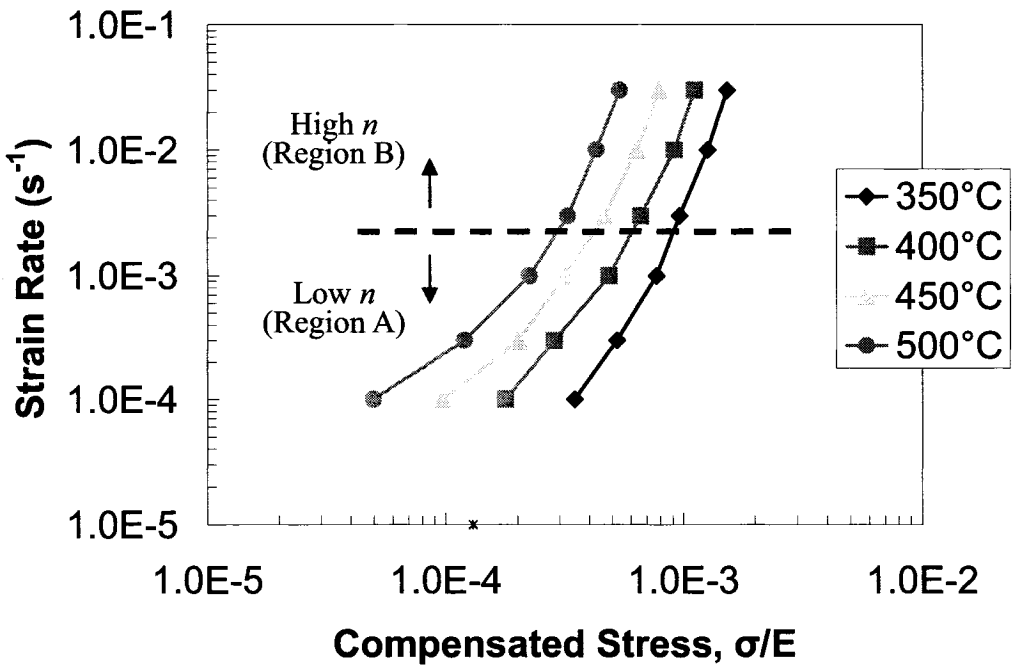

Figure 6 - 16. Strain rate vs compensated stress behavior of the G8 at different temperatures. Region A with low stress exponent (n = 2-3) and region B with high stress exponent (n = 4-6).

The individual corresponding n's relatively to grain size and temperature are summarized in Figure 6-17a for n in low strain rate regime and Figure 6-17b for n in high strain rate regime. As general trend, the stress exponent decreases with increasing temperature and decreasing grain size. At slow strain rate, the n values vary from 2-3, 2-4 and 3-4 for G8,

G20 and G50 respectively (Figure 6-17a). This variation of *n* values suggests that at slow strain rate regime the stress exponent is dependent on grain size and temperature. At high strain rate regime, all specimens tends to have stress exponent values about 4-5 when deformed at temperatures above 400°C, except at temperature of 350°C where G20 and G50 exhibit high n value of 6 (Figure 6-17b).

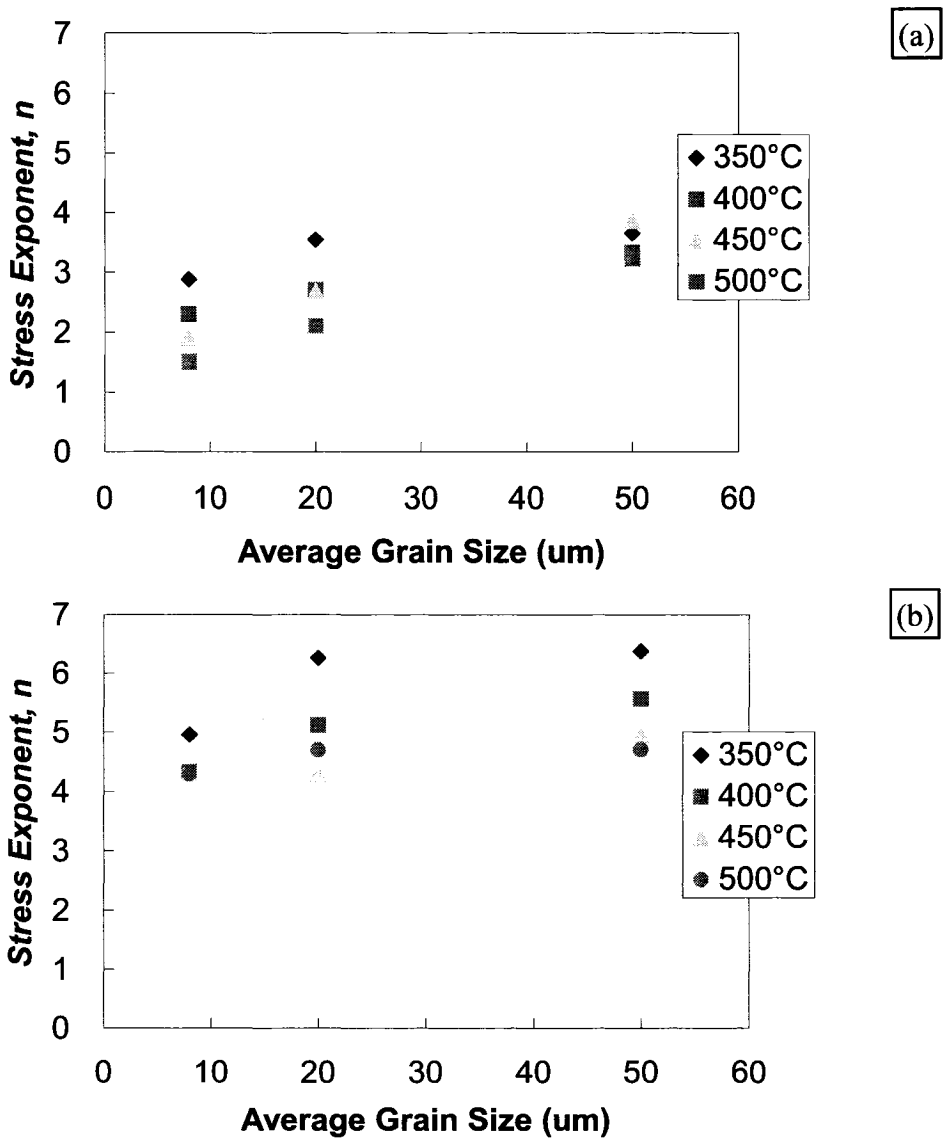

Figure 6 - 17. Stress Exponent, *n*, as a function of grain size and temperature at: (a) *n* in low strain rate regime; and (b) *n* in high strain rate regime.

Activation Energy

The vertical separation between data at different temperatures, but at same grain size and constant σ/E, in Figure 6-16, is proportional to the activation energy. The activation energy can be calculated from SRC data using the following equation:

$$Q = -R\frac{\partial \ln \dot{\varepsilon}}{\partial 1/T}\bigg|_{\sigma/E}$$

Equation 6-2

where R is the gas constant, 8.314 J/mol·K, $\dot{\varepsilon}$ is true strain rate and T is the absolute temperature. For calculation of Q, the data for each material is divided into two regions from the viewpoint of stress exponent: region A and region B, associated with low stress exponent (n = 2-3) and high stress exponent (n = 4-6), respectively (Figure 6-16)[9]. Figure 6-18 shows the activation energies for G8 for both A and B regions.

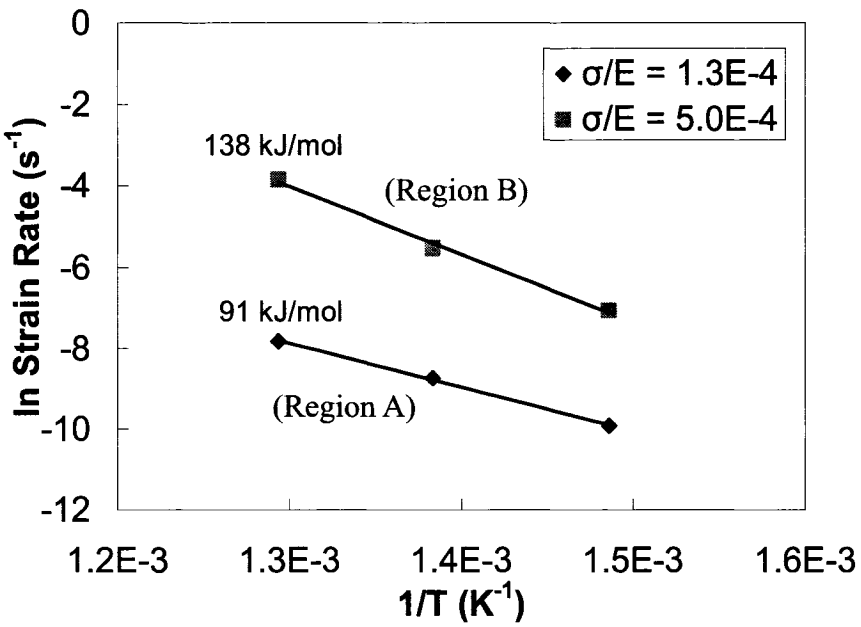

Figure 6 - 18. Activation energies for G8 for both A and B regions. Q=91 kJ/mol at σ/E = 1.3 x10^{-4} (region A) and Q=138 kJ/mol at σ/E = 5.0 x10^{-4} (region B).

[9] The activation energies were calculated from temperatures ≥ 400°C and they were measured from two separated regions (A and B) in order to avoid the mixed mode deformation mechanism zone.

The activation energies for the three specimens measured from SRC test data are shown in Figure 6-19. For specimen with a grain size of 8 μm in the low strain rate regime (region A), Q is equal to 91 kJ/mol (at $\sigma/E = 1.3 \times 10^{-4}$). In the high strain rate regime (region B), the activation energy increases to 138 kJ/mol (at $\sigma/E = 5 \times 10^{-4}$). The activation energy corresponding to specimen G20 is 102 kJ/mol (at $\sigma/E = 2 \times 10^{-4}$) in region A and 160 kJ/mol (at $\sigma/E = 8 \times 10^{-4}$) in region B. The Q values for specimen G50 are 119 (at $\sigma/E = 3 \times 10^{-4}$) and 167 kJ/mol (at $\sigma/E = 8 \times 10^{-4}$) in region A and B, respectively. It is noticed that the Q values for G20 and G50 in region B are considered quite high compared to Q value for G8. The reason behind this abnormal high Q values is assumed to be DRX effect that causes softening in these specimens with coarse grains and reduces the flow stress during early stage of deformation (Figure 6-10b).

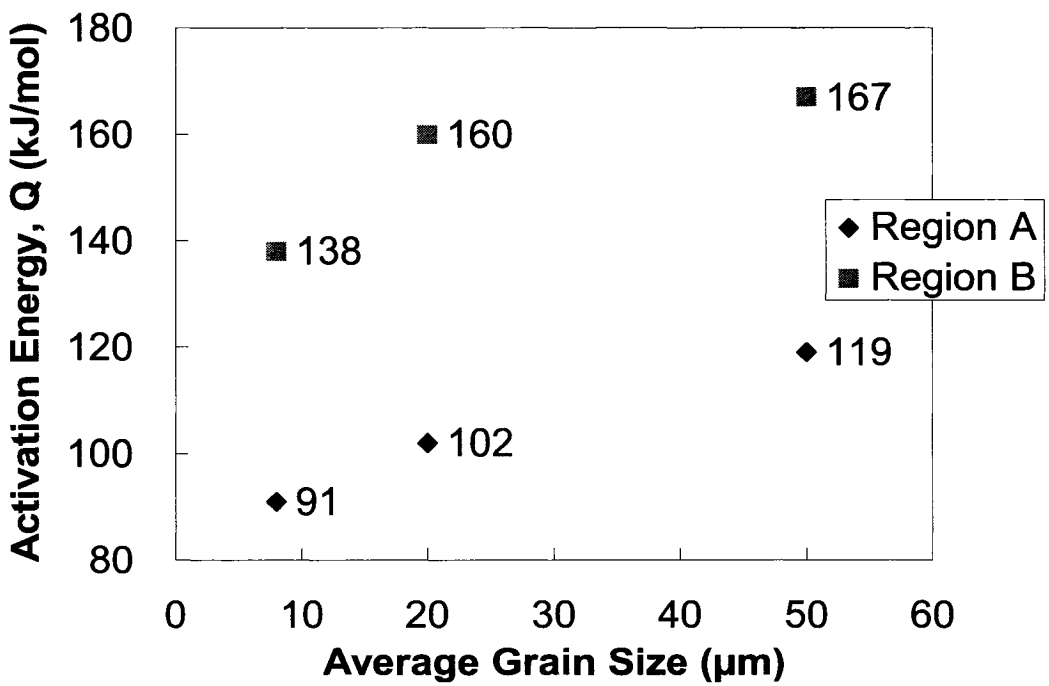

Figure 6 - 19. Activation energies as function of grain size for both A and B regions.

Summary of Deformation Behavior

Summarizing our experimental findings, first, it was found (Figure 6-17) that, in the low-strain-rate regime, the stress exponent increases with grain size, from a value of 2 (d = 8 μm) to 3 (d = 50 μm) at temperatures ≥ 400°C. These values of n are characteristic of GBS [8]. Simultaneously, the activation energy varies from a value of 91 kJ/mol to a value of 119 kJ/mol (Figure 6-19). These values are close to the activation energy for grain-boundary diffusion of Mg (Q = 92 kJ/mol) and significantly smaller than the activation energy for diffusion of Al atoms in a Mg matrix (143 kJ/mol) [8]. Thus, GBS, accommodated by grain-boundary diffusion, seems to play an important role during deformation in the low strain rate regime.

At high strain rate, the stress exponent increases to a value close to 5 for (d = 8 μm). This value is indicative of dislocation creep deformation mechanism, where the main deformation mechanism is crystallographic slip. This is consistent with the activation energy measured: 138 kJ/mol, which is close to both the activation energy for Mg self-diffusion (135 kJ/mole) and for diffusion of Al in Mg (143 kJ/mol) [8]. For the specimens with coarser grains G20 and G50, the stress exponent is about 6 at lower temperature (350°C), while it decreases to a value similar to the one for (d = 8 μm) at high temperatures (450 and 500°C). The trend of exhibiting similar flow stress, elongation and strain rate sensitivity regardless the grain size implies the effect of grain size becomes negligible at high strain rate, especially at high temperatures.

6.3.6 Microstructural Examination of Deformation Behavior

Selected fractured tensile specimens were chosen based on the resulted strain rate

sensitivity (m) value of the specimen for microstructual examination. Referring to Figure 6-14, three specimens G8, G20 and G50 deformed at 450°C with $1x10^{-3}$ s^{-1} resulted distinct m values of $m > 0.3$, $m = 3$ and $m < 0.3$ respectively were examined.

Figure 6-20 shows the fracture tip of the three selected specimens. It is observed that the failure mode of the three specimens was comparable and sign of cavities was seen near the fracture tip (Figures 6-20b, d and f). This is because they all fall into the GBS deformation mechanism category. At 450°C with $1x10^{-3}$ s^{-1}, these specimens have similar stress exponent (n = 2-3) and their activation energies were close to the one for grain-boundary diffusion of Mg (*Qgb* = 92 kJ/mol). However, the degree of necking seemed to be higher for G20 and G50 than G8. This is due their different strain rate sensitivities where the low m values from G20 and G50 suggest necking, whereas the high m value from G8 suggests resistance to necking. Therefore high elongation of 265% was obtained for this specimen.

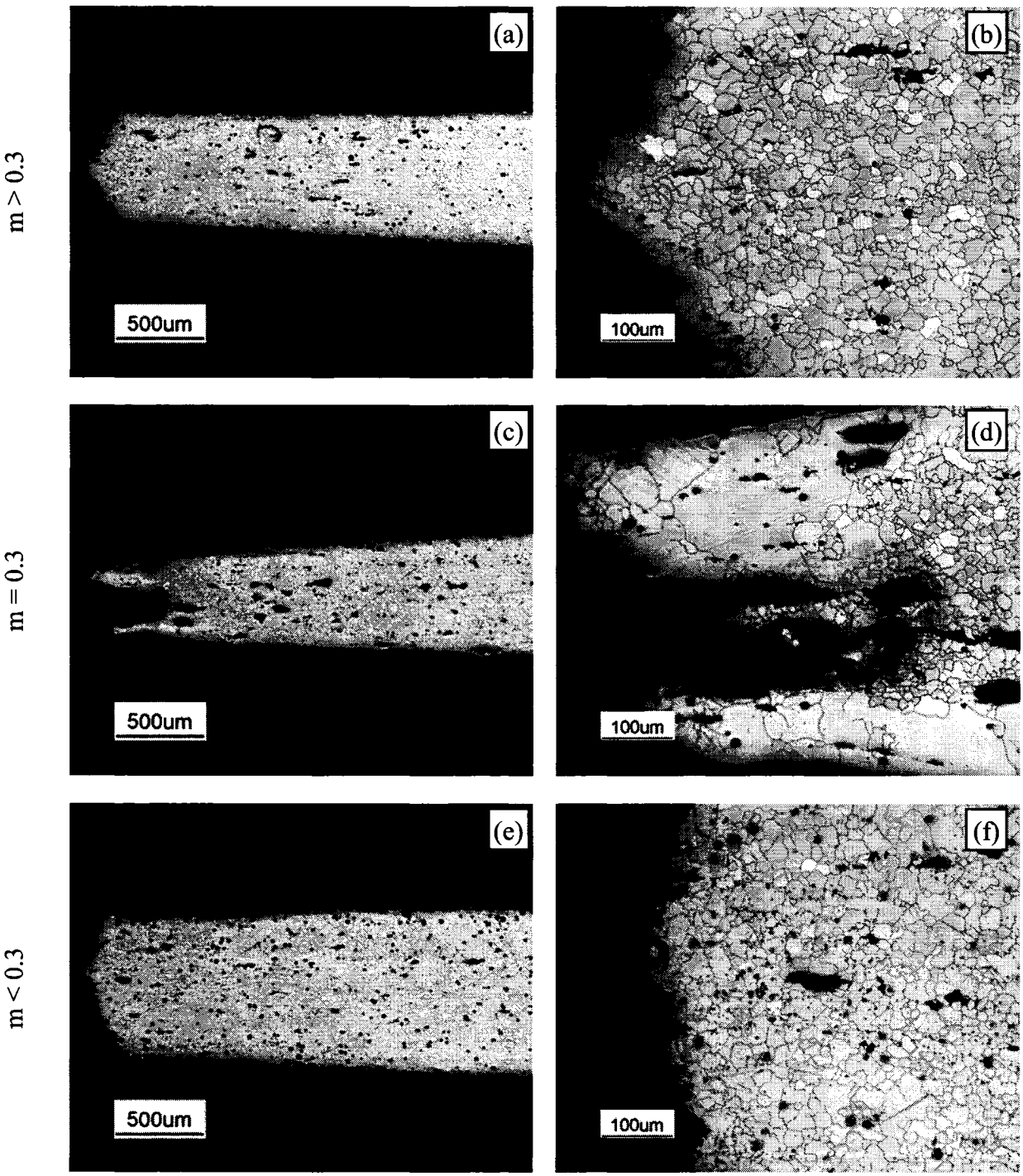

Figure 6 - 20. Fracture tip of specimen: (a-b) G8; (c-d) G20; and (e-f) G50. The tip of specimen G50 has been polished away. It was found initially abnormal grain growth and some necking at the tip of this specimen (G50).

Microstructure evolution along the gauge length of the specimens tested at 450°C and $1x10^{-3}$ s^{-1} was examined by optical metallography. Figure 6-21 shows change in grain size as a function of thickness strain variations along the gauge length of the G8, G20 and G50 specimens pulled to failure. The zero strain represents measurement in the un-deformed grip region of the tensile specimen, whereas the highest strain represents measurement near the fracture tip of the specimen. Microstructures in the grip and near the fracture tip of the G8 and G50 specimens are shown in Figure 6-22. It is observed that the fine grain G8 specimen undergoes significant dynamic grain growth during deformation with the grain size increasing from 10 μm at zero strain (Figure 6-22a) to 19 μm at fracture strain (Figure 6-22b). The initial coarse grain structure of the G20 and G50 specimens, on the other hand, undergoes grain refinement with increasing deformation. In case of the G20, the grain size changes from 26 μm at zero strain to 20 μm at fracture strain (Figure 6-21). The G50 specimen undergoes very large grain refinement, from 59μm at zero strain (Figure 6-22c) to 21 μm at fracture strain (Figure 6-22d). This grain refinement is a big factor in the large tensile elongation obtained with this initially coarse grain material. Similar observation of high ductility in a coarse grain AZ31 alloy was reported by Watanabe *et al.* [9].

The G50 plot in Figure 6-21 in fact shows two grain refinement dips one at a thickness strain of about 0.15 and another close to the fracture strain of 0.55. The dips are probably a case of double necking that occurred in the width direction of the tensile specimen. Further analysis would be needed to confirm the occurrence of double necking and multiple grain refinement cycles in the G50 material. Coincidently, for deformation at

450°C and $1x10^{-3}$ s^{-1}, the grain size in all three materials tends to approach 20μm (Figure 6-21). It will be interesting to confirm if 20μm is the most stable grain size for deformation of AZ31 at 450°C and $1x10^{-3}$ s^{-1}.

It may be pointed out that the grain sizes in the grip sections of the three specimens (Figures 6-21 and 6-22) are larger than the original grain sizes of the G8, G20 and G50 specimens, which is a consequence of static grain growth occurring at the high test temperature of 450°C.

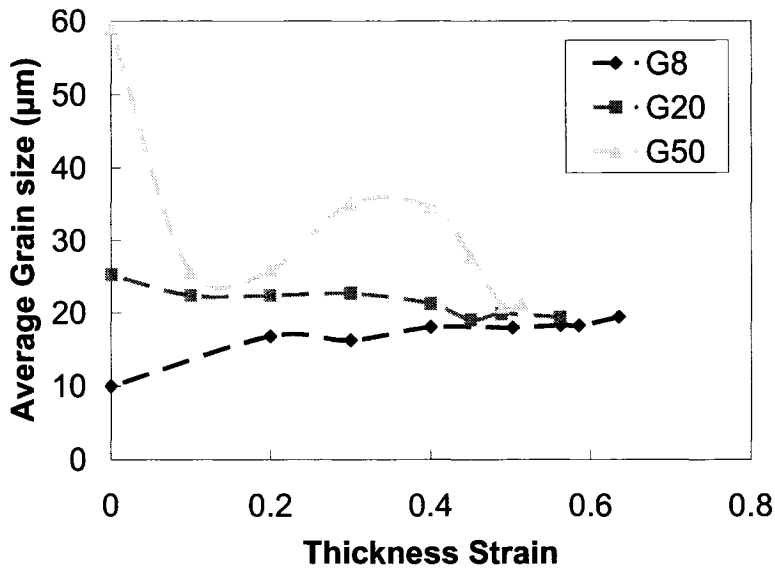

Figure 6 - 21. Microstructure evolution in tensile specimens deformed at 450°C and $1x10^{-3}$ s^{-1} strain rate, as a function of thickness strain variations along the gauge length of specimen pulled to failure. The thickness strain was measured as the change in the thickness of the specimen divided by the initial thickness. The highest thickness strain represented measurement near the fracture tip of the specimen, and the zero strain represented the un-deformed grip region.

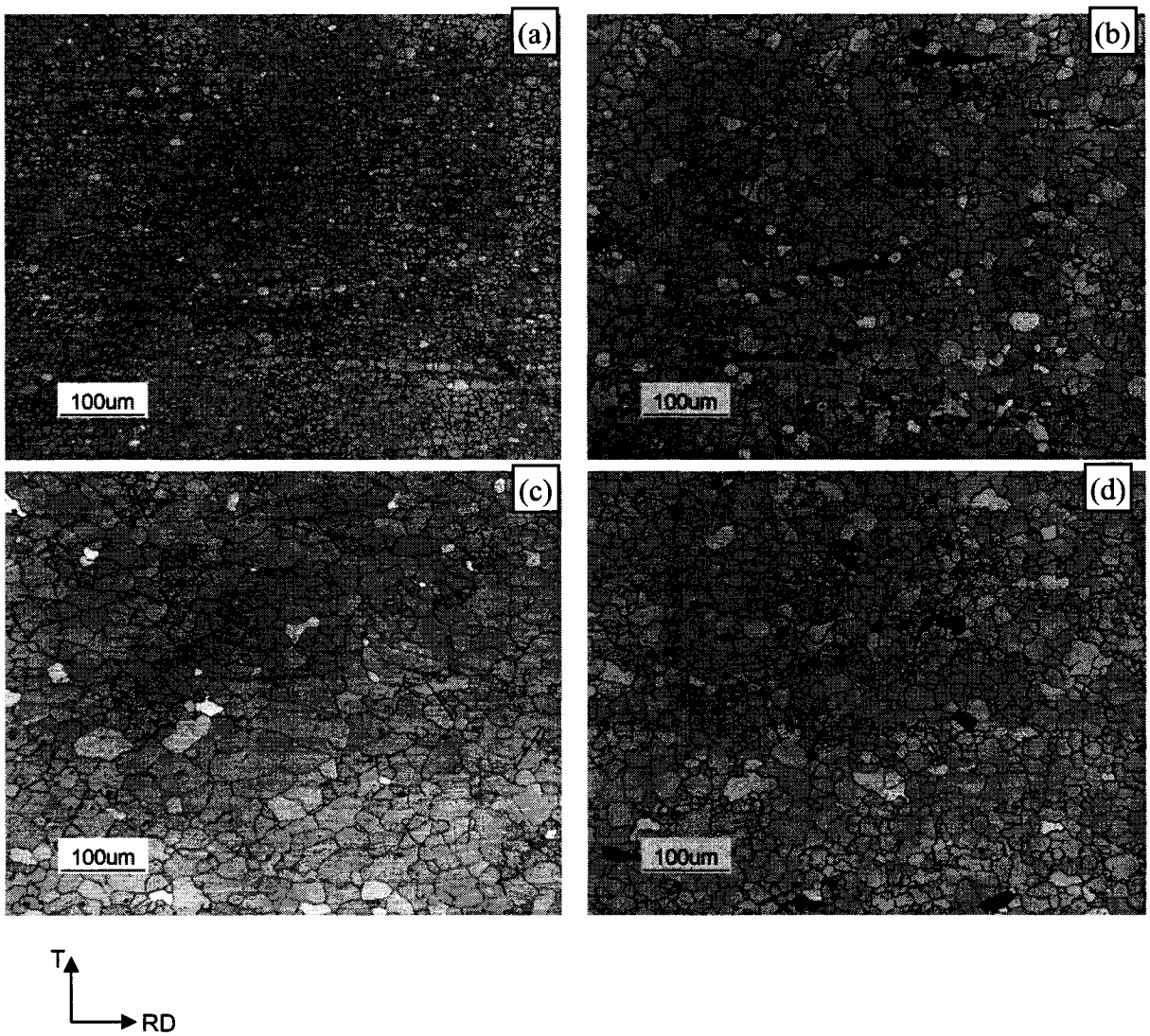

Figure 6 - 22. Microstructures of tensile specimens pulled to failure at 450°C and $1x10^{-3}$ s^{-1} strain rate: (a) G8 in grip region (d_{ave} = 10 μm), (b) G8 near fracture tip (d_{ave} = 19 μm), (c) G50 in grip region (d_{ave} = 59 μm), and (d) G50 near fracture tip (d_{ave} = 21 μm). RD: Rolling/Tensile Direction and T: Thickness Direction.

6.4 Summary

A heat treatment of 350°C/15 minute was established as the optimum recrystallization treatment for the AZ31 alloy, as it provided full recrystallization with the finest recrystallized grain size.

AZ31 sheet materials with different grain sizes from 8 to 80 μm can be produced from a fully annealed AZ31 alloy by imparting different cold reductions followed by recrystallizing.

High tensile elongations were obtained at high temperature and low strain rate condition (450°C and $1x10^{-3}$ s^{-1}) in all three different-grain-size (8, 20 and 50 μm) materials investigated. The highest elongation of 265% was obtained with the material having initial grain size of 8 μm. The deformation in this fine grain material was characterized by a significant hardening due to dynamic grain growth, followed by a steady flow behavior akin to grain boundary sliding. The material with initial grain size of 50 μm, under the same test conditions, showed large grain refinement due to dynamic recrystallization, resulting in significant tensile elongation in this coarse grain material. Deformation at 350°C and $1x10^{-1}$ s^{-1} was characterized by rapid strain hardening and localization, resulting in lowest tensile elongations

Strain-rate sensitivity, which is a good indication of material's ductility, suggested the highest with material with 8 μm grain size. As a common trend, the strain-rate sensitivity increases with decreasing strain rate, increasing temperature and decreasing grain size. At fastest strain rate of $1x10^{-2}$, the m values become "invariant" with grain size and

temperature.

The deformation conditions tested in the present study for G8, G20 and G50 are separated into two regions: (1) region A represents low strain rate regime with (n = 2-3) and (2) region B indicates fast strain rate regime with (n = 4-6). The *n* values in region A are characteristic of GBS and the *Q* values are close to the activation energy for grain-boundary diffusion of Mg (*Q* = 92 kJ/mol). Thus, GBS plays an important role during deformation in the low strain rate regime. On the other hand, the *n* values in region B are is indicative of dislocation creep deformation mechanism and the Q values are close to both the activation energy for Mg self-diffusion (135 kJ/mole) and for diffusion of Al in Mg (143 kJ/mol). Hence, dislocation creep is the main deformation mechanism at fast strain rate regime.

At 450°C with $1x10^{-3}\ s^{-1}$, all three specimens (G8, G20 and G50) were examined under optical microscope near the fracture tip. They exhibits similar failure mode and sign of cavities is seen near the fracture tip. At this deformation condition, they all have comparable stress exponents (n = 2-3) and activation energies are close to the one for grain-boundary diffusion of Mg (*Qgb* = 92 kJ/mol). However, the degree of necking seemed to be higher for G20 and G50 than G8. This is due their different strain rate sensitivities where the low m values from G20 and G50 suggest necking, whereas the high m value of G8 suggests resistance to necking.

6.5 References

1. Reed-Hill, R.E., Physical Metallurgy Principles, 2nd ed., 1973.

2. Ravi Verma and Jon T. Carter, *SAE*, 2006.

3. Caceres, C.H. & Wilkinson, D.S., "On the Mechanism of Strain-Enhanced Grain Growth During Superplastic deformation", *Acta Metall.*, v. 32, 1984, pp. 1335-1345.

4. Del Valle, J.A. et al., "Deformation Mechanisms Responsible for the High Ductility in a Mg AZ31 Alloy Analyzed by Electron Backscattered Diffraction", *Metallurgical and Materials Transactions A*, v. 36A, June 2005, pp. 1427-1438.

5. Tan, J.C. & Tan, M.J., "Dynamic Continuous Recrystallization Characteristics in Two Stage Deformation of Mg-3Al-1Zn Alloy Sheet", *Materials Science and Engineering*, A339, 2003, pp. 124-132.

6. Mukherjee A. K., "Deformation Mechanisms in Superplasticity", A*nnu. Rev. Mater. Sci.*, 1997, pp. 191-217

7. Frost, H. J. and Ashby, M. F., in *Deformation Mechanism Maps*. Pergamon Press, Oxford, 1983, p. 44.

8. H. Somekawa et al., "Dislocation creep behavior in Mg–Al–Zn alloys", *Materials Science and Engineering*, A 407, 2005, pp. 53–61.

9. Watanabe H. et al., "Deformation Mechanism in a Coarse-Grained Mg-Al-Zn Alloy at Elevated Temperatures", *International Journal of Plasticity,* v. 17, 2001, pp. 387-397.

Chapter 7

Formability of AZ31

7.1 Introduction

The results of experiments on formability are presented in two sections: in one the r-value of AZ31 sheet at elevated temperatures was examined and in the other the Forming Limit Diagram, which is used to design most stamping operation was measured.

7.2 High temperature r-value of Commercial AZ31 Sheet

7.2.1 Methodology for r-value Measurement

The suitability of sheet metal for deep drawing operation or its resistance to thinning is characterized by the plastic strain-ratio, r-value. R-value is measured in a tensile test by interrupting the test at an axial strain of about 10%[10] (for Mg), measuring the changes in width, thickness in the gage section of the specimen and taking a ratio of the true width strain (x-axis) to true thickness strain (z-axis), as shown in equation 7-1. In this present study, however, the measurements were made on a tensile specimen that was stretched to failure. These specimens were of the same materials used in Chapter 5 and r-value was measured for all deformation conditions (details in Chapter 5). As shown in Figure 7-1, the r-values were obtained based on the measurement of the strain ratios (equation 7-1) at different locations along the gage length (y-axis) of the failed specimen, according to Lankford formulae[11]:

$$r = \frac{\log\left(\frac{x_0}{x}\right)}{\log\left(\frac{z_0}{z}\right)}$$

Equation 7-1

[10] At room temperature the uniform elongation for wrought Mg alloys was found to be ~10% [1]

[11] Adapted from Equation 2-2

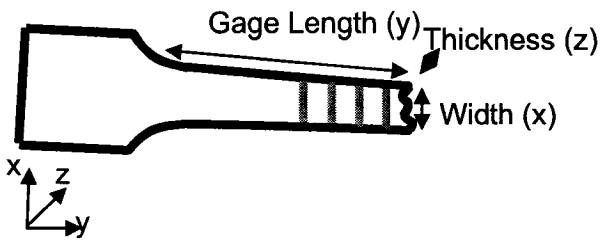

Figure 7 - 1. Schematic image of r-value measurements made on a tensile specimen stretched to failure.

An r-value measured for a constant axial strain (10%) does not necessarily correspond to the initial state (prior to start of deformation) of the material, since the structure has been changed due to texture transformation accompanying deformation during the straining. As proposed by Truszkowski and Szpunar [2], the set r values measured from a single failed specimen can be expressed by relation $r_\eta = f(\eta)$, where η is the true cross-section (area) strain in x-z plane of the specimen[12]. Hence r_0 can be obtained by extrapolation of $r = f(\eta)$ to $\eta = 0$ (initial state of the material before testing), the r_{10} ($\eta = 10\%$) can be extrapolated as well. Figure 7-2 presents the r-value (r_η) as function of axial strain along the gage length for specimen deformed at 300°C with strain rate of $1x10^{-1}$ s^{-1}.

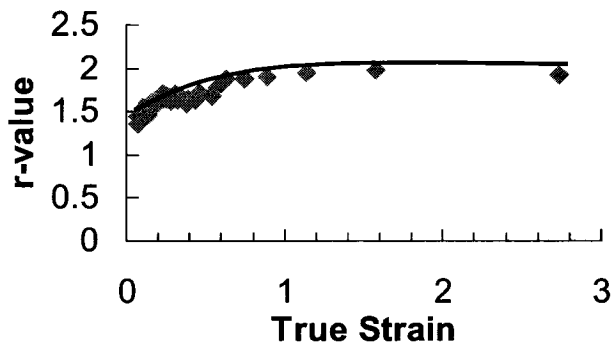

Figure 7 - 2. r-value (r_η) as function of axial strain along the gage length. r_0 and r_{10} extrapolation methodology adapted from Truszkowski and Szpunar [2]. Specimen deformed at 300°C with strain rate of $1x10^{-1}$ s^{-1}.

[12] The physical meaning of the r_0 obtained in this way has been provided in ref [3]

7.2.2 Effect of Temperature and Strain Rate on r-value on AZ31 Sheet

The r-value is used to evaluate formability. The r-value represents the sheet's resistance to thinning, with a higher r-value being preferred. In Agnew's work, r-value of AZ31 sheet was investigated up to 250°C. It shows that AZ31 sheet indeed has strong anisotropy of r-value at room temperature due to the basal texture, but this anisotropy decreases as temperature increases. In the present study, the r-values (r_0 and r_{10}) of the RD at various deformation conditions (temperatures and strain rates) were measured at temperatures 300°C and higher. Figure 7-3 shows the extrapolated r_0 (at strain of zero) and r_{10} (at strain of 10%) values for different temperatures and strain rates from the fractured tensile specimens stressed along the RD.

The r-values (both r_0 and r_{10}) increase with increasing temperature and strain rate. In order to explain the different r-value observed at different deformation condition, one can refer to Figure 7-4 which shows the correlation of r-value (r_{10}) and failure modes. This is a combination of results from Figures 5-7 and 7-3. As a recap of Chapters 5 and 6, in slow strain rate ($\leq 1x10^{-3}$ s^{-1}) and at high temperature ($\geq 400°C$) the main deformation mechanism is controlled by GBS and results in cavity interlinkage failure, while at fast strain rate ($\geq$ $1x10^{-2}$ s^{-1}) and high temperature ($\geq$ 400°C), the deformation is controlled mainly by dislocation creep and strong necking is observed. From Figure 7-4, it is seen that the deformation conditions associated mainly with GBS result in fair drawability/formability of AZ31 sheet with r-value about 1. A good drawability of the sheet having r-value above 1.5 is obtained when the main deformation mechanism is controlled by dislocation creep and the specimen failed by strong necking. The activation of additional slip systems (non-basal <a> and <c+a>), helps to prevent thinning during

deep drawing. The high r-value observed at 450°C with $0.1s^{-1}$ implies stronger resistance to thinning. This deformation condition might suggest optimum forming process parameters, especially for deep drawing, for the AZ31 sheet under investigation.

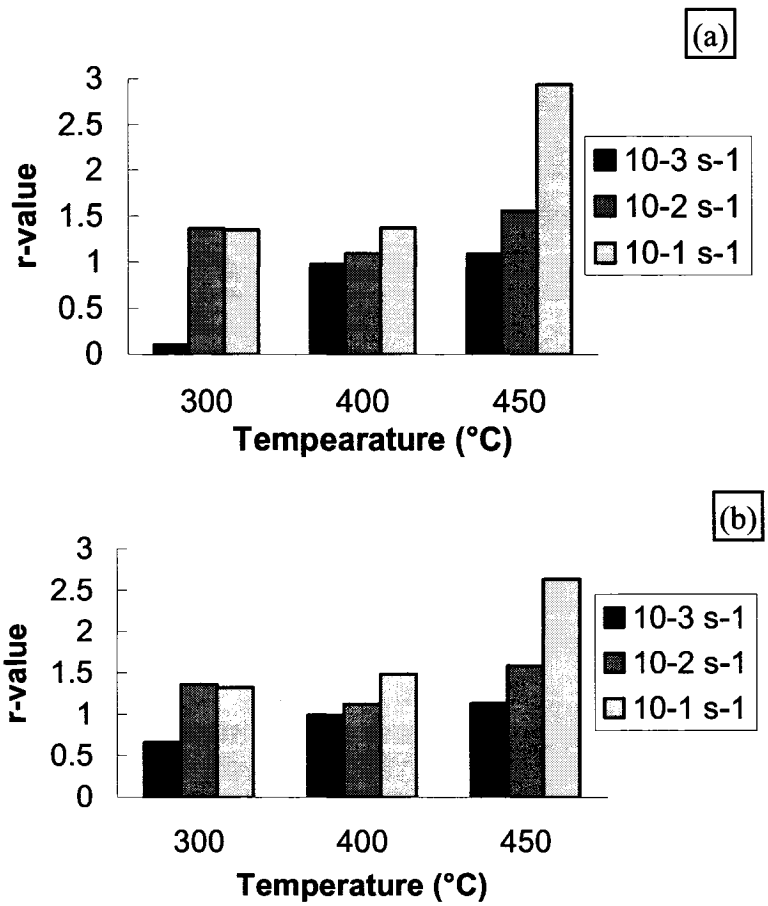

Figure 7 - 3. Extrapolated (a) r_0 and (b) r_{10} at various deformation conditions. The r-values were measured along the RD direction.

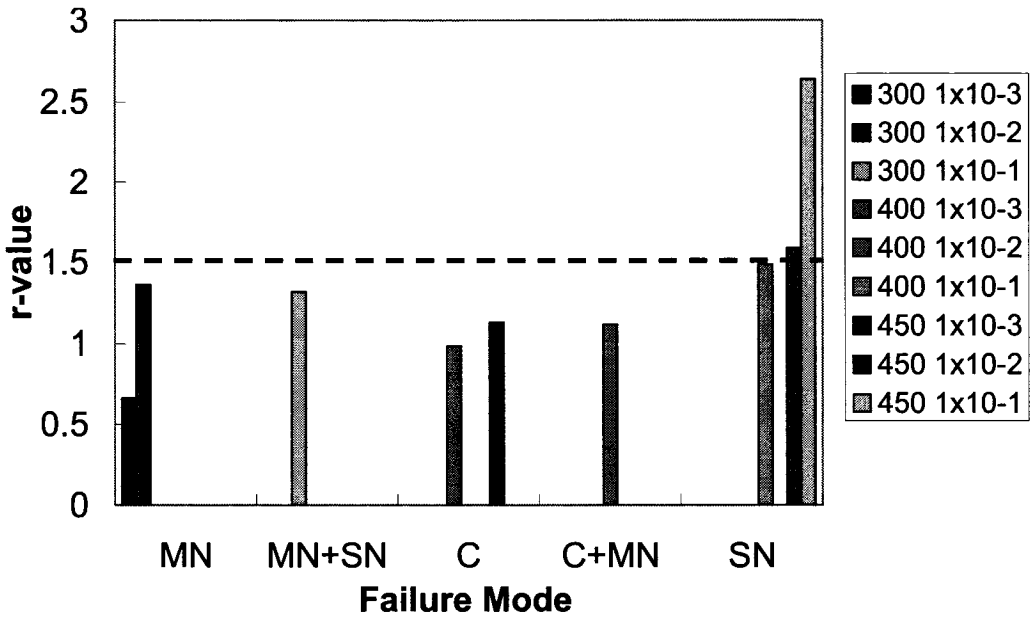

Figure 7 - 4. Correlation of r-value and failure mode (deformation mechanism) of commercial AZ31 sheet at various deformation conditions. Notation: MN as moderate necking failure, C as cavity interlinkage failure, SN as strong necking failure, C+MN as moderate necking failure with some trace of cavity, and MN+SN as necking degree in between of MN and SN.

7.3 Forming Limit Diagram of Commercial AZ31 Sheet

7.3.1 Methodology for Forming Limit Diagram Measurement

Samples Preparation for Forming Limit Diagram

Commercial AZ31 alloy sheet selected in this part of work was 1.3 mm thick. This material was supplied by Magnesium Electron (MEL). It had same chemical composition and processing history as the material used in Chapter 6, except that the present material was rolled to thinner thickness. Figure 7-5 shows a micrograph of the material in the as-received condition, which represents heavily deformed microstructure consisting of twins and deformation bands. The chemical composition of the material is shown in Table 6-1.

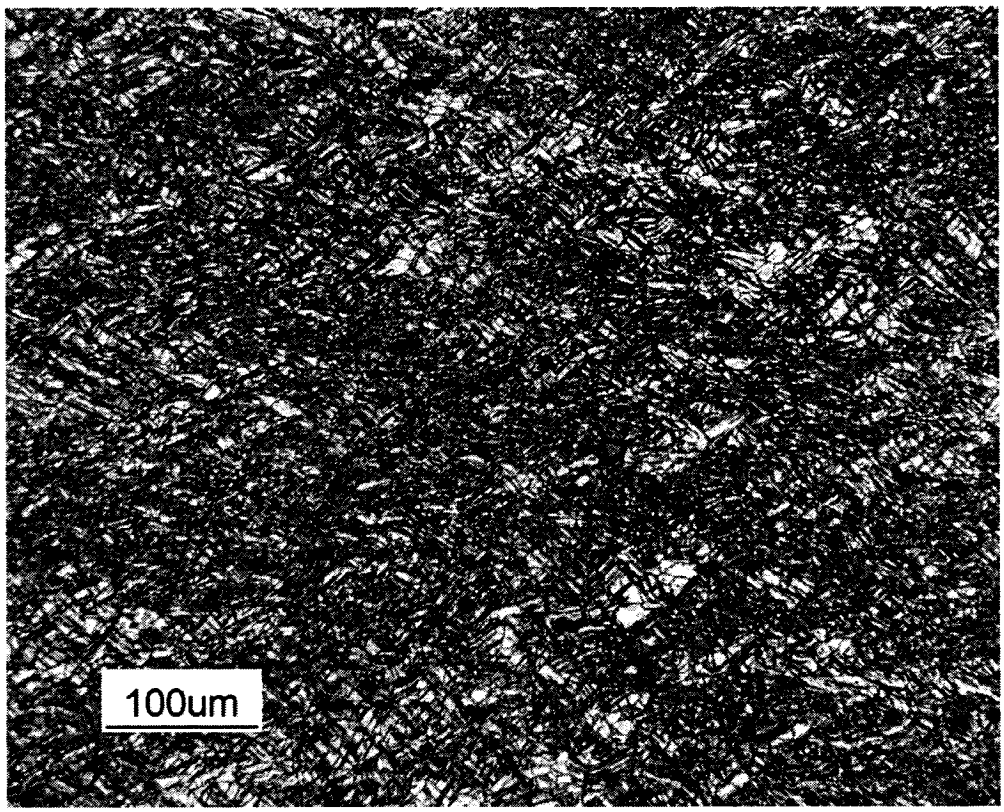

Figure 7 - 5. Microstructure of AZ31 Mg sheet as-received condition (as hot-rolled sheet).

In order to determine the different strain states, the following dimensions were designed for forming test of AZ31 sheet (Figure 7-6): (1) circular specimen with a 7" diameter for biaxial stretching (Figure 7-6a), (2) 3" width specimen for quasi plain strain test (Figure 7-6b) and (3) 1.5" width specimen for uniaxial tensile test (Figure 7-6c). The specimens with 1.5 and 3" width, were cut along planes coinciding with the rolling direction. The reason for cutting the specimens with side cuts of different radii instead of cutting straight was to prevent the premature failure at die entry radius[13].

[13] Since the cut edges were locations where defects were mostly present and the stress distribution at these straight cut edges were not evenly distributed while forming, die entry radius failure occurred.

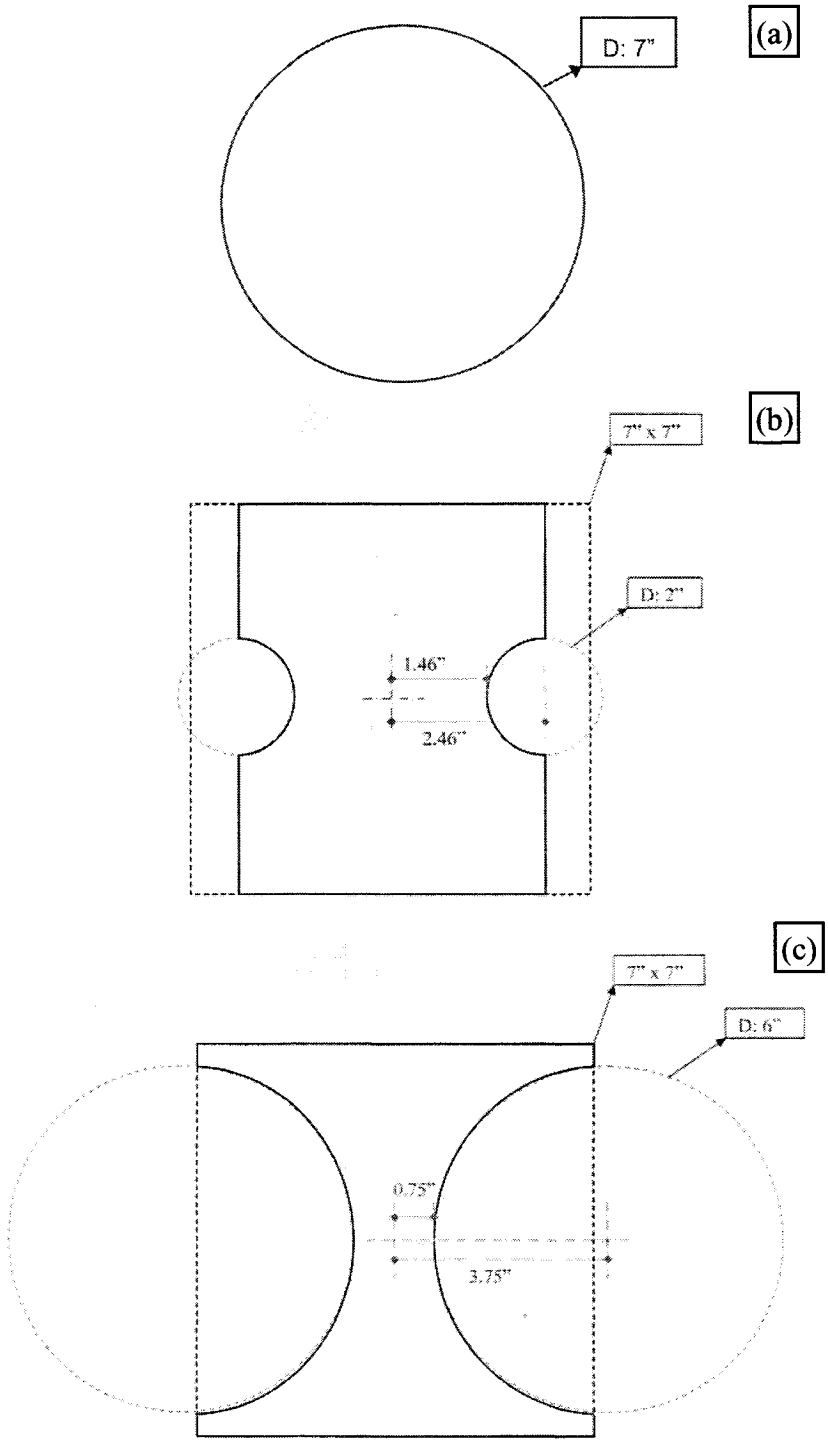

Figure 7 - 6. The specimen dimension for forming test: (a) circular specimen with a 7" diameter for biaxial stretching, (b) 3" width specimen for quasi plain strain test, (c) 1.5" width specimen for uniaxial tensile tests.

Prior to the test, the specimens were electrochemically etched using a LNC-4[1] solution for Mg material to make a circle grid pattern with 2.54mm-diameter circles. The set-up for the electrochemical etching process is shown in Figure 7-7.

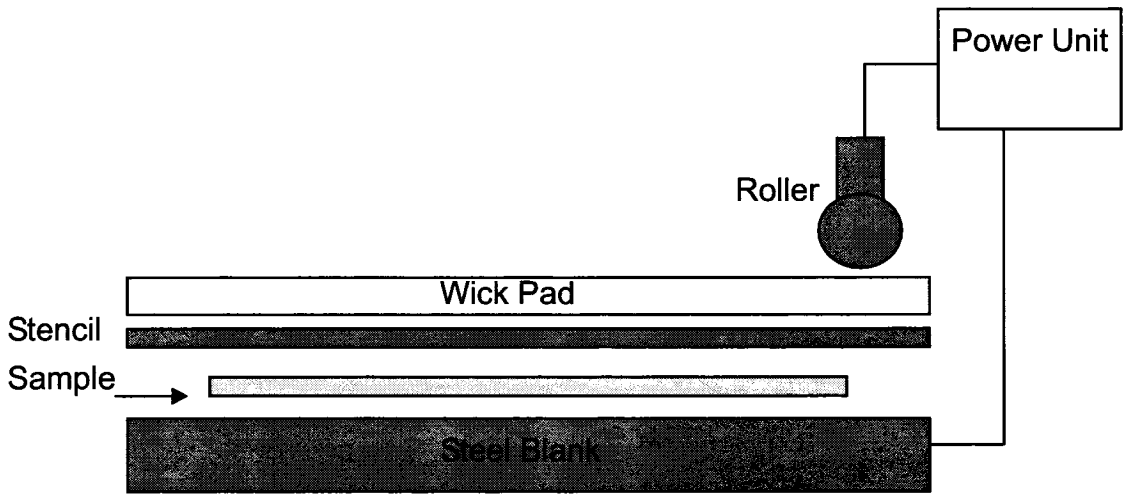

Figure 7 - 7. The set-up for the electrochemical etching process.

Forming Procedures

Limiting Dome Height (LDH) test was conducted on AZ31 sheet material at the temperature 300°C under a suitable punch speed of 0.005in/sec. This test method is by stretching a specimen over a 4" diameter hemisphere punch and friction is present during the test. Figure 7-8 depicts the tool (Interlaken Model 3360-400-LDH) and the specimen set-up for the LDH test. Boron nitride (BN) was used as lubricant and was sprayed on the bottom surface (i.e. surface facing the punch) of the specimen. The test at high temperature was performed under isothermal condition where the tooling (spherical punch, upper and lower clamp rings) were heated and covered using an insulation. The specimens were preheated to the desired temperature for 5 min before forming and the temperature of specimen was kept constant until the specimen was stretched to failure.

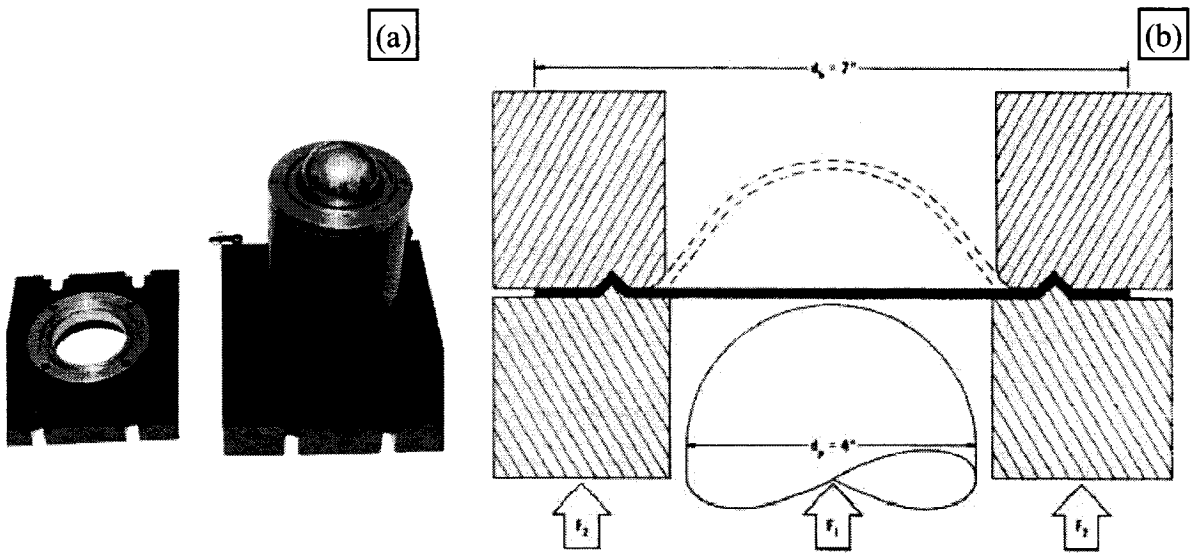

Figure 7 - 8. (a) Limit Dome Height (4" diameter punch) test tool and (b) specimen set-up for the LDH test.

During the test, specimens clamped at the periphery were stretched to failure. After forming, the engineering major and minor strains were measured from the deformed circles with an aid of GPA camera[14] at the locations close to the fracture for each specimen. Figure 7-9 shows the camera tool and the method of recording the measurement. Using a Grid Pattern Analyzer GPA 3.0, the major and minor strains were recorded from measurement of the deformed circle and were plotted against one another with the major strain axes as the coordinate. The curve fitted into the measured strain points was defined as the forming limit curve. The diagram showing this forming limit curve is called the Forming Limit Diagram.

[14] ASAME technology LLC

Figure 7 - 9. GPA camera tool and the method of recording the measurement.

7.3.2 Forming Limit Diagram of AZ31 by Limit Dome Height Test

Figure 7-10 demonstrates the resulting AZ31 test specimens from LDH test method at 300°C. The major and minor strains were measured from three different regions: failed, necked and good (i.e. undeformed) regions. Figure 7-11 illustrates how these terminologies are defined in the present work. Based on the outcome of repeated test results, there was no specific preferred orientation fractured for the biaxial stretched specimen, unlike for the gas forming where AZ31 sheet material tends to tear at the top of the dome and along the RD. Since friction was present during the LDH test, the failure zone of the test specimens was not located at the top of the dome. As a result, deformed circles near the fractured region from the biaxial stretch test showed rather an ellipsoid shape than circular. Although these results were not representing the balanced biaxial stretch zone, they were still considered as good data points on the FLD. In Figure 7-10b, die entry radius failure was observed; this implied that the 3" width dimension design is needed to be reviewed and possibly changed to avoid this type of failure. Nevertheless, the sign of tearing was seen on the second test of the 3" width specimen by lowering slightly the clamp load.

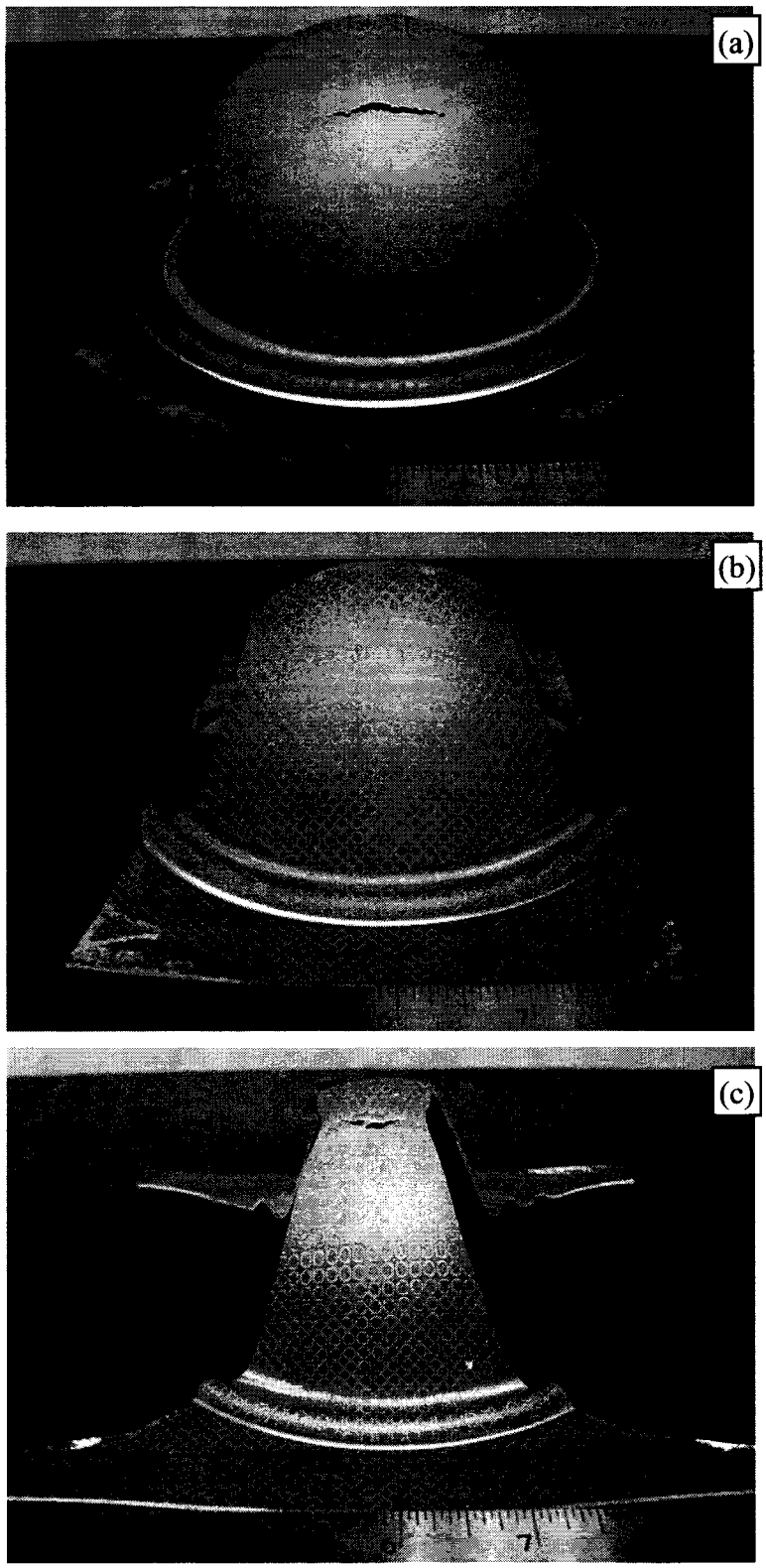

Figure 7 - 10. The resulting AZ31 specimens formed from Limit Dome Height test at 300°C (a) 7" circular specimen, (b) 3" strip specimen and (c) 1.5" strip specimen.

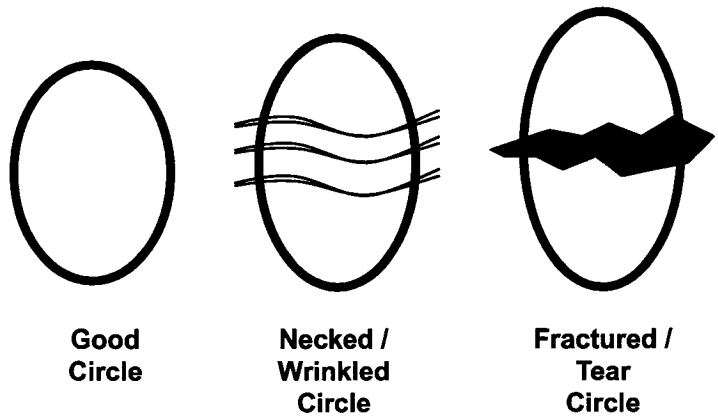

Figure 7 - 11. Terminology of good, necked and fractured circles.

Forming limit diagram of AZ31 at 300°C using limiting dome height test is shown in Figure 7-12. The FLD_0 of AZ31 at 300°C with punch speed of 0.005 in/min was found to be 67%. Similar results were reported in Chen's work (Figure 2-15) [4]. However, his FLD_0 results showed slightly lower value compared to the present study. This rather minor difference might be due to the use of different AZ31 sheet material and testing parameters (e.g. punch speed).

From the perspective of the functionality of a formed part, the punch displacement at peak load (part depth) is another important measure of the formability. Figure 7-13 shows the part depth of biaxial forming of AZ31 by LDH at 300°C. It shows a value of 1.86 in under an isothermal heating condition, where die and punch were heated to the same temperature. This value was found to be the same under three repeated tests, whereas the maximum LDH (height of the dome) were varied from 2.4 to 2.6 in. These experimental results obtained in the present study provide the fundamentals for the stamping die design of forming AZ31 sheets.

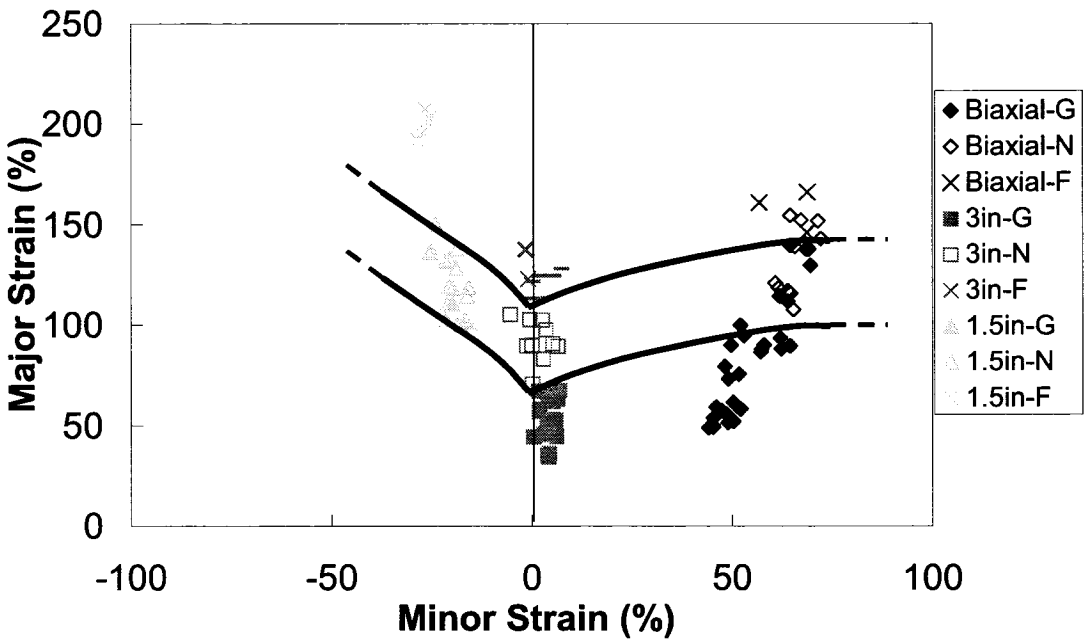

Figure 7 - 12. The Forming Limit Diagram of AZ31 by Limit Dome Height test at 300°C. G: Good circle; N: Necked circle; F: Failed circle. (The – symbol indicates the strongly necked region found in the first 3" width specimen been formed.)

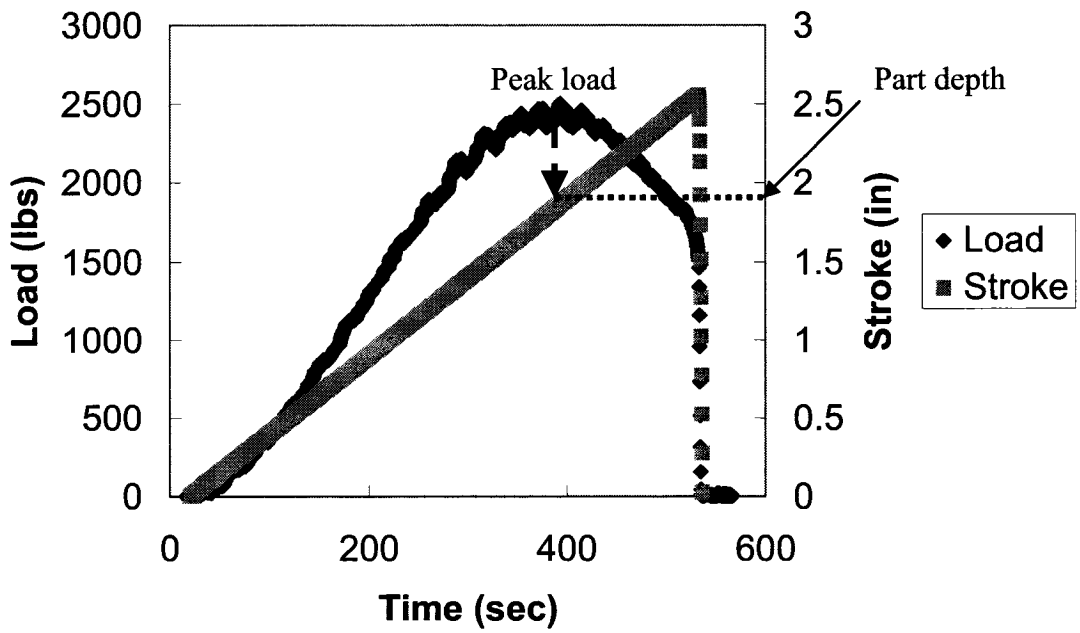

Figure 7 - 13. Load and stroke values of biaxial forming of AZ31 by Limit Dome Height test at 300°C. The part depth is 1.86 in and the maximum LDH is 2.6.

It would be an interest to examine the part depth or the maximum LDH by gas forming under the same condition and to compare the results of both different forming technique in order to understand the effect of the friction. Furthermore, it has been reported that the part depth of aluminium material can be increased significantly under a suitable thermal gradient where a higher die temperature is used to soften the periphery of the specimen to promote enhanced draw-in of the material. Hence, this could be additional experiment for investigating the forming behavior of AZ31.

7.4 Summary

The r-values (r_0 and r_{10}) representing the sheet material's resistance to thinning were obtained by extrapolating the width-to-thickness strain ratios of the tensile specimens pulled to failure under various deformation conditions (temperature and strain rate). The r-values increased with increasing test temperature and strain rate. The highest r-values (r_0 and r_{10}) were observed at 450° C and $0.1s^{-1}$. Hence this deformation condition might be considered the best for forming deep drawn parts from the commercial AZ31 sheet.

A preliminary study of Forming Limit Diagram for AZ31 sheet was performed at 300°C with punch speed of 0.005 in/min by Limit Dome Height test method. The FLD_0 of AZ31 was found to be 67%; the part depth of biaxial forming was 1.86 in; and the maximum LDH were varied from 2.4 to 2.6 in. Additional experiments for investigating the forming behavior of AZ31 sheet will be required in order to build the criterion for stamping processes.

7.5 References

1. Agnew, S. & Duygulu, O., "A Mechanistic Understanding of the Formability of Magnesium: Examining the Role of Temperature on the Deformation Mechanisms", *Materials Science Forum*, v.419-422, 2003, pp. 177-188.

2. Truszkowski W., Dutkiewicz J. & Szpunar J., "Évolution de la texture et de l'anisotropie lors du laminage du laiton", *Mémoire Sciencifiques de la Revue de Métallurgie*, LXVII, N° 5,1970, pp. 355-365.

3. Truszkowski W. & Jarominek J., "Plastic Anisotropy of cold rolled copper", *Archiwum Hutnictwa*, v.14, 1969, pp. 309-326.,

4. Chen, F.-K. and Huang, T.-B., "Formability of stamping magnesium-alloy AZ31 sheets", *Journal of Materials Processing Technology*, v.142, 2003, pp. 643–647.

Chapter 8

Conclusion

As an introductory understanding of deformation modes on AZ31 reported in Chapter 4, only basal slip and twinning contribute to room temperature deformation. The twins are believed to be $\{10\bar{1}2\}$ tensile twins characterized by the broad morphology because of its smaller value of twinning shear. They are formed at low strain level, but once grain boundary shearing is evident, the fracture occurred. In the high temperature and high strain deformation condition, polygonization and necklacing are observed. When deformation is constrained and / or amount of strain is increased, the slip lines are more complex which imply activation of additional slip systems (prismatic and pyramidal).

Based on the results obtained in Chapters 5 and 6, an increase of ductility in the Mg sheet was contributed to dynamic recrystallization occurring readily at elevated temperatures ($\geq 300^{\circ}C$). Even coarse grain material experienced significant tensile elongation due grain

refinement. Despite the presence of DRX, the strong (0001) texture was still observed for all deformation conditions. Depending on temperature and strain rate, different deformation mechanisms were activated and lead to different failure modes (moderate necking, cavity, strong necking). More specifically, deformation at elevated temperature in the low-strain-rate regime with stress exponent *n* being about 2-3 is characteristic of GBS. At this deformation regime, the activation energy is close to the one for grain-boundary diffusion of Mg (Q = 92 kJ/mol). Thus, GBS with some accommodation of dislocation creep seems to be the deformation mechanism. The presence of dislocation creep mechanism is dependent on the amount of activation of non-basal and <c+a> slips during deformation, however this requires further investigation to obtain more quantitative results. On the other hand, at high strain rate and high temperature in the deformation regime, the stress exponent increases to a value close to 5. This *n* value is an indicative of dislocation creep deformation mechanism and is consistent with the activation energy for Mg self-diffusion (135 kJ/mole) and for diffusion of Al in Mg (143 kJ/mol). Plus the six-fold symmetric patterns of the $\{1\bar{1}00\}$ and $\{11\bar{2}0\}$ pole figures and the splitting of basal plane distribution are another indication of slip mechanism or dislocation creep mechanism. Figure 8-1 illustrates the above findings for AZ31 deformation mechanism associated with failure mode at elevated temperature deformation.

In Chapter 6, the optimum deformation behavior for AZ31 sheet was found to be for the material with fine grain microstructure. The highest elongation of 265% was obtained with the material having initial grain size of 8 μm. In addition, strain-rate sensitivity, which is a good indication of material's ductility, also was the highest in material with 8

μm grain size. As a common trend, the strain-rate sensitivity increases with decreasing strain rate, increasing temperature and decreasing grain size. At fastest strain rate of $1x10^{-2}$, the m values become "invariant" with respect to the grain size and temperature.

In term of drawability of AZ31 sheet as discussed in Chapter 7, the deformation controlled by GBS resulted in a fair drawability/formability property with r-value about 1; while a good drawability of the sheet having r-value above 1.5 is obtained when the main deformation mechanism was controlled by dislocation creep. Due to activation of additional slip systems (non-basal <a> and <c+a>), the thinning of the sheet was prevented. Figure 8-1 explains the different deformation mechanisms associated with r-value. The high r-value observed at 450°C with $0.1s^{-1}$ implies stronger resistance to thinning. This deformation condition might suggest good forming process parameters, especially for deep drawing, for the commercial AZ31 sheet under investigation.

A preliminary study of Forming Limit Diagram for AZ31 sheet was performed by Limit Dome Height test method at 300°C. The FLD_0 of AZ31 was found to be 67%; the part depth of biaxial forming was 1.86 in; and the maximum LDH were varied from 2.4 to 2.6 in. Additional experiments for investigating the forming behavior of AZ31 sheet will be required in order to build the criterion for stamping processes.

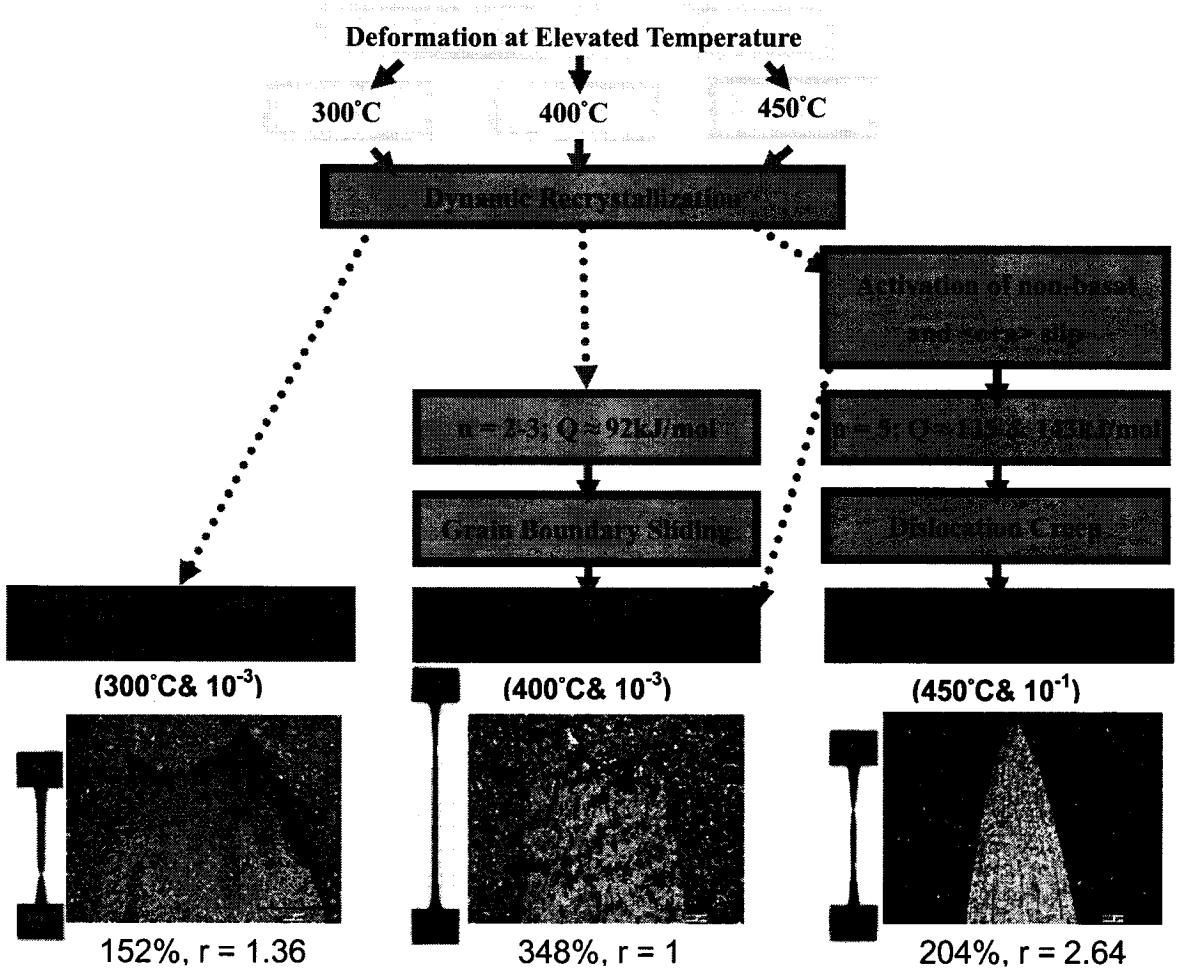

Figure 8 - 1. Illustration of AZ31 sheet deformation mechanism associated with failure mode and r-value at elevated temperature deformation.